2013

Dynamic Modeling of Channel Formation During Fluid Injection Into Unconsolidated Sands

Sayamik Ameen
Louisiana State University and Agricultural and Mechanical College, smoha11@lsu.edu

DYNAMIC MODELING OF CHANNEL FORMATION DURING FLUID INJECTION INTO UNCONSOLIDATED SANDS

A Thesis

Submitted to the Graduate Faculty of the
Louisiana State University and
Agricultural and Mechanical College
in partial fulfillment of the
requirements for the degree of
Master of Science

in

The Craft and Hawkins Department of Petroleum Engineering

by
Siyamak Ameen
B.S. Eng., University of Koya, 2008
December 2013

Acknowledgments

I would like to express my sincere gratitude to my advisor, Dr Arash Dahi for the opportunity to work on this project and for his guidance and support throughout this work at Louisiana State University.

Beside my advisor, I am also indebted to my committee members; Dr Mayank Tyagi for many valuable discussions I had with him, Dr Stephen Sears and Dr Krishnaswamy Nandakumar for their insightful comments and Dr Karsten Thompson for joining the committee toward the end of the project. An appreciation would also go to Dr Andrew Wojtanowics for his advice on my graduate study and also for giving me the opportunity to work at LSU Drilling Fluid Laboratory. I would also like to thanks Shell Exploration & Production for sponsoring the project and Mr. George Wang from Shell E&P for his generous help and support for this project.

I would like to thank all my friends at Louisiana State University and Geomechanics research group and special thanks to Houman Bedayat, Ali Takbiri and Denis Klimenko for their productive comments throughout the research, as well as their sincere friendship. I would also like to thank my girlfriend, Tiare Angelo, she have been a great help and support for me at LSU.

Last and most importantly, I would like to thank my family for their endless love and support: my parents Najaf and Fuzieh, my brother Saman and sisters, Delnya, Sonya and Laila.

Table of Contents

List of Tables

List of Figures

Abstract

Water injection is widely used for sweeping hydrocarbons in waterflooding operations, and also for maintaining reservoir pressure or disposing waste water. Injection at a high rate is required to maintain the economy of waterflooding projects; however, loss of injectivity is a quite common problem in unconsolidated sand formations like deep water Gulf of Mexico. Well intervention operations, hurricanes, and other issues require frequent shut-downs during the life of offshore wells; in order to minimize deteriorating effect of these shutdowns on wellbore injectivity more accurate modeling of the injection process is needed.

Injection of water into a saturated, granular, porous medium can lead to internal erosion and consequently formation of preferential flow paths within the medium due to channelization. Channelization in porous medium might occur when local fluid-induced stresses become locally larger than a critical threshold; then grains are dislodged and carried away, hence porosity and permeability of the medium will be altered along the induced flow paths. Vice versa, flow back during shut-down might carry particles back to the well and cause sand accumulation and consequently loss of injectivity. In most cases, to maintain injection rate operators increase injection pressure and pumping power. The increased injection pressure results in stress changes and further channelization in the formation.

Experimental lab studies have confirmed the presence of dependent and independent flow patterns (Huang, 2011, Golvin, 2011). Considering the above-mentioned scenarios, long-held assumptions like Darcy flow or homogeneity and symmetry of flow paths are no longer acceptable for fluid flow at most of the injectors. There is a need for models to describe flow patterns and predict probable issues for water injection at the reservoir scale. A finite volume model is developed based on multiphase volume fraction concept that decomposes porosity to mobile and immobile porosity where these phases change spatially and evolve over time and lead to development of erosional channels in radial injection patterns depending on injection rates, viscosity, and magnitude of in situ stresses and rock properties. This model will

account for both particle releasing and the suspension deposition. Sensitivity studies on the effect of failure criteria for unconsolidated sand, flow rates, cohesion and permeability shows qualitative agreement with experimental observations.

Chapter 1: Introduction

2.1 Description of the Problem

Injectivity depends on interstitial velocity of injected water which is related to injection rate, injection water temperature, erosional channels, volume concentration of solids, size of proppants, width and length of Frac-pack, and in-situ stresses. Any alternation of status of each of these parameters could change injectivity.

The injection water usually contains a combination of biological, hydrocarbons, and mineral materials which precipitation of those materials due to incompatibility of injection water chemical properties and formation water chemical properties leads to formation plugging. The occluding particles could also have migrated from the formation to the wellbore vicinity during injection shut down. In any case, any reduction in permeability near the wellbore region would require an increase of injection pressure to maintain a constant injection rate. Afterward, with the fracture face plugged with continued injection, the pressure at the fracture tip exceeds the fracture propagation pressure therefore the fracture starts to grow.

Injectivity decline could happen due to plugging of near wellbore region pore throats by moving small particles. These particles could be precipitated due to the inconsistency of injection water chemical properties or formation chemical properties, or they might be transported by injection water. Particle plugging could also happen due to flow back from formation to near wellbore region during injection shut-in. Figure 2.1 shows an example of injectivity decline due to plugging induced by high particle concentration in the injected water into unfractured, gravel packed injectors in unconsolidated sand in the Gulf of Mexico (Wennberg, 1998). In Figure 2.1 describes that initial injectivity was low and repeated simulations were performed. After each simulation, injectivity increased dramatically but then declined progressively and more rapidly. The half-life of some of these wells was approximately 50 days and this means within 50 days, the injectivity had decreased by 50% which is economically unsatisfactory.

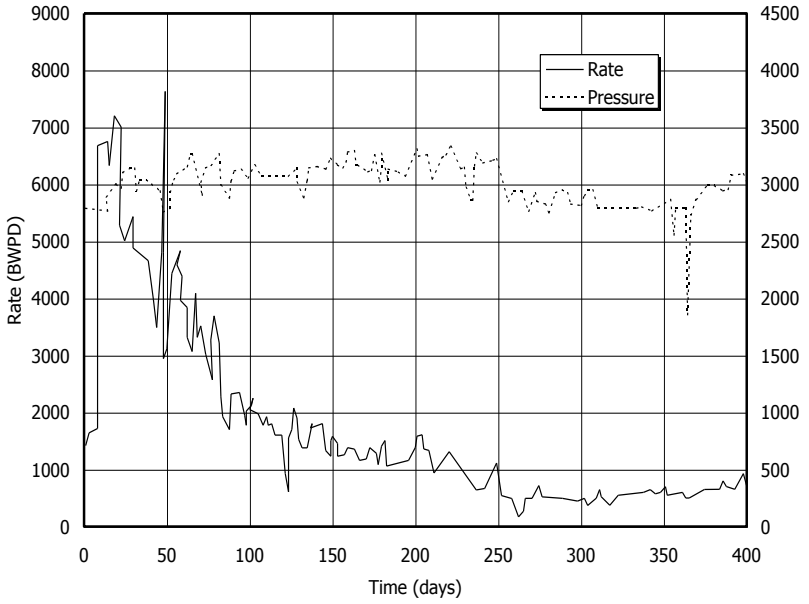

Figure 2.1. Injection decline for Well A09 (matrix injection, unconsolidated, Gulf of Mexico). (Wennberg, 1998)

Temperature difference between the injection fluid and the formation may also change injectivity. When cold water such as seawater is injected into a hot reservoir, a cold region of cooled rock develops in the vicinity of wellbore (Gadde, 2001) and contraction of the cooled region causes tensile stresses to develop in the cooled region. These thermal stresses will assist injection pressure to fracture the formation rock. Since fractured rock has higher permeability than formation rock, fluid flow will be directed mainly through induced fractures which improve injectivity temporarily but then declines progressively and more rapidly.

Formation of channels leads to injectivity decline and in some cases, loss of injectivity. Channelization in porous medium happens when the local fluid-induced stress is larger than a critical threshold; grains are dislodged and carried away this causes the porosity of the medium to be altered by erosion. This, in turn, affects the local hydraulic conductivity and pressure in the medium and results in the growth and development of channels that preferentially conduct to flow.

Depending on induced fracture conductivity, injection rate, damage in fracture wells, and formation permeability waterfront geometry could have different displacement geometry. A model is provided to simulate channelization in porous media that account for all above mentioned scenarios. This is followed by a model for flowback which simulates the movement of particles from the formation to the wellbore in case of injector shut-down.

2.2 Research Objective

The primary objective of this research is to model dynamic evolution of mobile particle motions spatially and in temporally due to change in fluid flow and to investigate their effects on consequent injectivity decline. In order to correctly investigate the fundamental failure mechanisms and flow patterns involved in fluid injection into porous medium, the objectives for this thesis are defined as

- Develop a numerical model to simulate flow-induced channelization in a domain subject to one-dimensional uniform flow.
    - Provide a dynamic porosity field model to show porosity field evolution during injection.
    - Define appropriate dimensionless variables so that the dimensionless variable will provide scalable results for thresholds of erosion and deposition.
    - Develop a two-dimensional numerical solution using finite volume methods.
- Develop a numerical model for near wellbore and two-dimensional geometries to study initiation and development of erosion channels in radial injection patterns under different injection rates, viscosities and rock properties.
    - Investigate the effect of rock heterogeneity on the formation of channels near the wellbore and its effect on fluid flow pattern.
- Provide a numerical solution for flow back in near- wellbore region and particles transportation which results in sand production in injector wells.

- Coupling the model developed for erosional channelization to the model that will provide flow back analysis. The created model will be used to apply real field data to obtain model parameters for predicting near wellbore behavior.
- It is crucial to have access to field data such as rock properties and injection history to achieve the defined goals of this project and validate the proposed models. Rock properties include elastic and plastic properties, which can be extracted from the logs and core analysis. To assess injection performance, normalized injectivity plots can be extracted from the field data. Change in the normalized injectivity slope is directly proportional to changes in injectivity and frac-pack situations in downhole.

Computational efficiency is an important factor in this effort because the goal of this work is to provide a practical and usable model that will account for real field data. Based on these objectives, the dependencies and resources for obtaining the goal of this project are provided in Figure 2.2.

Figure 2.2. Dependencies and Resources for the Project

Chapter 2: Literature Review

Injection wells are sensitive to the formation damage induced by water injection. Injectivity decline during water injection could occur due to suspended particles in the injected water, plugging near the wellbore, precipitation resulting from incompatible injected water, fines migration, and the swelling of clay minerals. Studies discussing factors affecting injectivity decline have been published, however, no clear model exists to consider the effect of fines migration toward the wellbore.

Kuo et al. (1984) has studied surface injection pressure behavior observed in the Somatito Field, a fault block in the Talara area of Northwest Peru, explained by a fracture extension mechanism. Kuo relates occasional pressure buildup to fracture plugging followed by "sharp pressure drop" due to fracture extension. Kuo et al. used the Geertsma and Klerk (GdK) model for plane strain hydraulic fracturing to predict fracture length at the water injector sites. In the GdK solution, it is assumed that fracture openings near the tips are proportional to the square root of the distance from the fracture tips. Leakoff volume should be limited or small to satisfy this assumption, which is not realistic situation in water injectors.

Sharma et al. (1997) assumed that the injectivity decline in water injection wells happens due to particle plugging and oil droplets existing in the injected water. The fracture growth rate and its relationship with injection rate and the concentration of injected water are studied in this model. Also, the concept of transition time, which results in permeability reduction in injection wells, gravel packed wells, and fractured wells (WID Model for injectivity decline) is proposed in this model.

Gadde et al. (2001) combined a single well simulator to a reservoir simulator and for the first time simulated oil displacement efficiency in systems where the fracture length is increasing with time. The physics of fracture growth is modeled by taking into account the effect of thermal stresses as well as particles plugging. If the temperature of the injected fluid is different from the formation, a thermal front with a temperature different from the original rock temperature propagates from the injection well. A

single well injection model was combined with three dimensional flooding models to capture the effect of fracture growth rate, fracture orientation, and reservoir properties on oil recovery such as pore pressure. The effect of rheological complex fluid such as polymers was not included; also the simulator was limited to water flooding applications.

Slevinsky (2002) proposed a model for thermally induced fractures that relies on actual injection pressure and rate data. Unlike the coupled geomechanical, fracture growth, fracture/reservoir plugging, thermal reservoir simulation models, the approach taken in this model is that the plugging and thermally induced fracturing is inevitable so that the problem can be addressed simply as if the injection was one hydraulic treatment. The proposed model does not rely on geomechanical coupling or detailed thermal modeling.

Zhai and Sharma (2005) developed an analytical model for coupling geomechanics with fluid flow for analyzing the stress state and flow around in injection wells to model fracture growth in unconsolidated sands. Material behavior was considered linear elastic but porosity was made a function of the bulk volumetric strain and permeability was a function of effective stress based on empirical models. The Mohr Coulomb failure criterion was used to predict shear or tensile failure at any point and in case shear failure was detected permeability tensor was modified according to an empirical correlation. Zones of shear failure result in high permeability zones and fracture propagation were thus represented by growth of the high permeability zones in a preferred direction with the orientation being primarily determined by the in-situ stress state.

Al-Kindi et al. (2008) reported difficulties at injection sites in Ursa and Princess Fields, Gulf of Mexico. The main reservoir in these fields is Yellow reservoir an upper Miocene turbidities reservoir charged with light oil.

Experiments conducted by Bohloli and de Pater 2006, have consistently reported higher net fracturing pressures in soft and plastic materials. Moreover, the net fracturing pressures increase with decreasing fluid efficiency because, unlike very high stress concentrations which develop at the crack tip in a brittle linearly elastic material, the stress concentrations at the crack tip in a plastic material are much lower due to ductile yielding at the tip, which relieves and redistributes the high stresses in the vicinity of the tip. Thus, plastic yielding at the crack tip effectively shields the crack from the influence of pressures acting at its faces (Papanastasiou 1999; Dong and de Pater 2008). Therefore, higher net fracturing pressures are required to obtain high enough stress concentrations at the tip to further crack the formation by tensile failure. The cavity expansion and shear bands which resulted from injection of low efficiency fluid is shown in Figure 3.1. In Figure 3.2, the fracture obtained with cross linked gel plus quartz powder is shown.

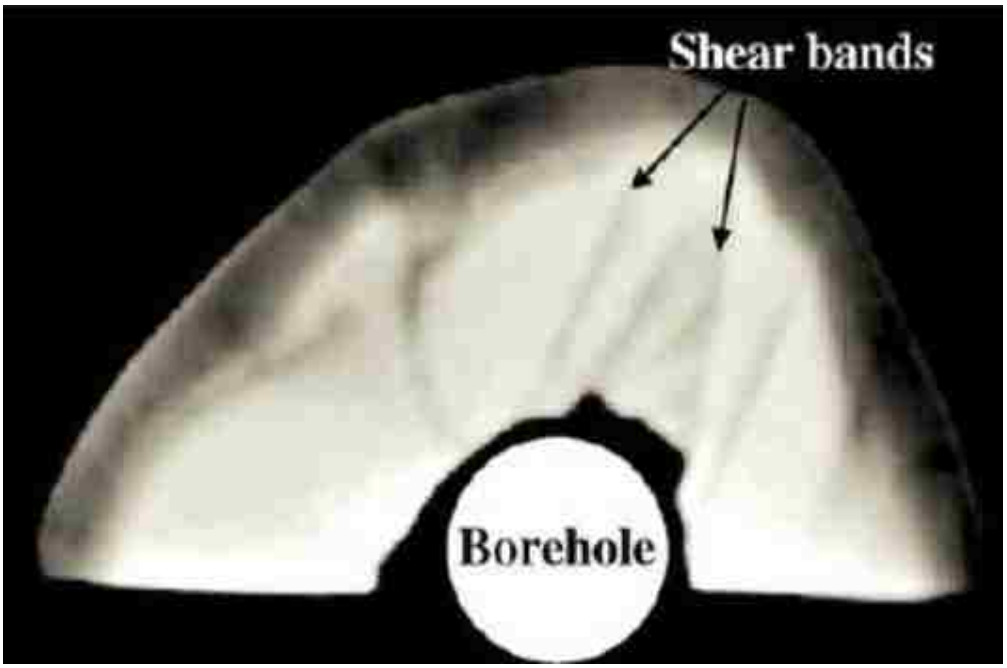

Figure 3.1. Cavity expansion and shear bands due to injection of low efficiency fluids (Bohloli, 2006)

Figure 3.2. Fractures obtained with cross linked gel plus quartz powder (Bohloli, 2006)

Huang (2011) studied different flow pattern formations for fluid injection in two dimensional porous media at surface conditions. A series of injection experiments were conducted in a Hele-Shaw cell with radial flow in a dry dense granular medium invaded by an aqueous glycerin solution. By changing the invading fluid viscosity via weight concentration of glycerin and by adjusting the normalized injection velocity and injection rate four distinct fluid displacement regimes have been observed: 1) a simple radial flow regime 2) an infiltration-dominated regime 3) a grain displacement-dominated regime 4) a viscous fingering-dominated regime. In Figure 3.3, the light-colored areas are occupied by dry sand only. The black areas indicate the fluid-only areas and the brown areas are the fluid infiltrated areas. While fluid permeates through the granular medium with a nearly circular front and no fluid channels were created in test A1, in all other cases, fluid flow resulted in significant grain displacements, which in turn created channels occupied by fluid only. Huang also conducted that by increasing fluid viscosity and velocity from test A1 to C4, a transition in the fluid flow behaviors occur from infiltration-dominated to infiltration-limited. Figure 3.4 shows the change in wellbore pressure for different injection rates.

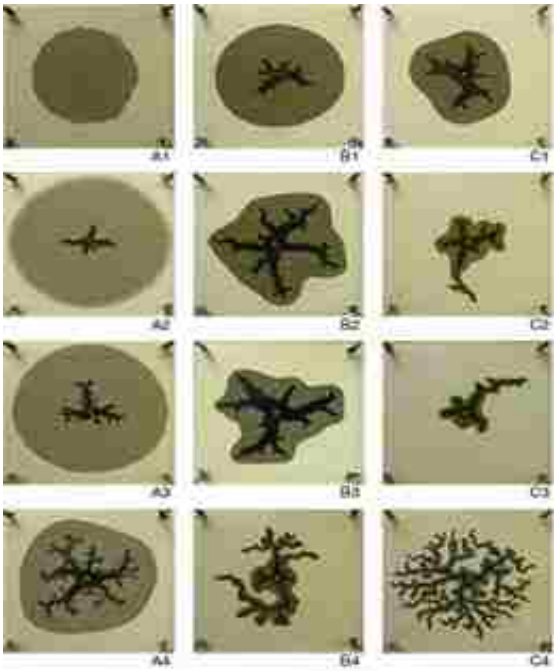

Figure 3.3: Image from series of displacement patterns from the injection of experiment with dry Ottawa sand and glycerin in a radial Hele-Shaw cell with different injection rate and fluid viscosity (Huang 2011).

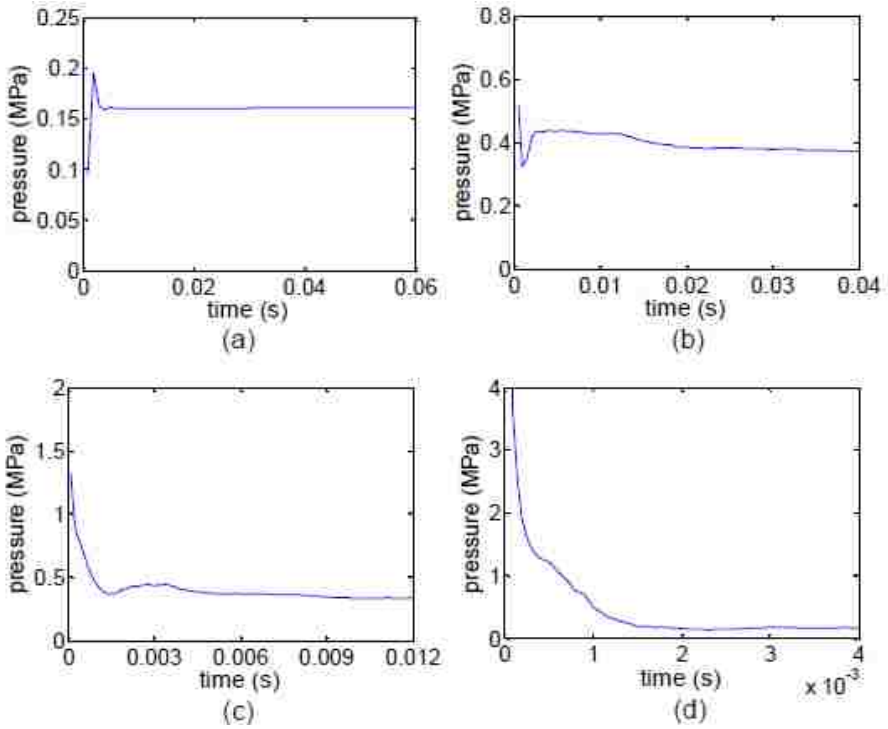

Figure 3.4. Wellbore pressure history for a) v=1m/s, b) v=3m/s, c) v=5m/s, d) v=14m/s.

Mahadevan et al. (2012) conducted an experiment following a model for flow-induced erosional channelization in a saturated, granular porous medium. The experiments were carried out in a fluid-saturated porous medium confined to a vertical quasi-two dimensional chamber based on a Hele-Shaw cell filled with bi-disperse mixture of glass beads as shown in Figure 3.5. The developed model is based on relationships between fluid flow gradient and degradation of grain matrix due to induced local fluid flow. In a square domain porous media, when a local flow-induced stress is greater than a critical threshold, the smaller grains are separated and transported which leads to a change in the porosity of a porous medium; therefore, hydraulic conductivity finally results in the development of erosional channels. Erosion mainly happens due to a drop in mean pressure gradient, while most of the flow occurs through the channels.

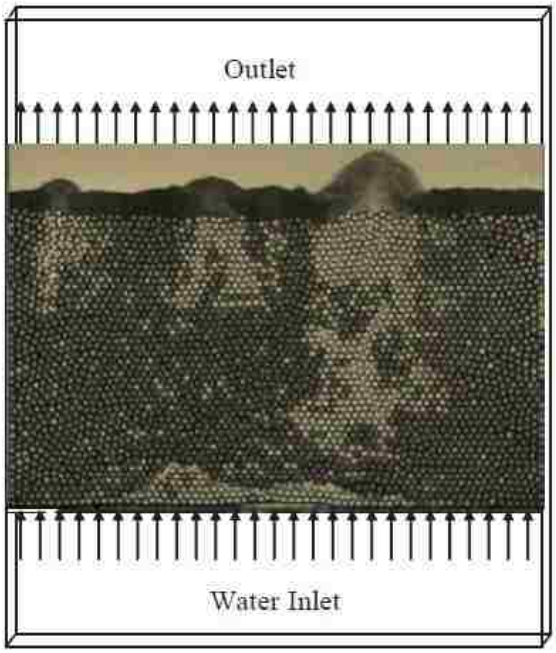

Figure 3.5. Snap shot showing the spatially varying porosity generated fluid flow

Golvin (2011) conducted multiple injection stages of a heated low viscosity dyed gel-water solution into cohesion-less sand, which is subjected to controlled 3-D confining stress, to examine the

formation of a fluid-front pattern in the invaded zone. Post-test examination of the solidified invaded zones displays a multilayered structure of sand developed during the flooding and/or fracturing stages of injection. In Figure 3.6, the effect of injection rate on the invaded zone is shown using snapshots of the experiment. Figure 3.6. A, shows a uniform sand structure with a smooth boundary that is observed under flooding condition. In contrast, a heterogeneous invaded zone structure with visible irregular higher porosity/permeability so called “channels” is formed under fracturing conditions as shown in Figure 3.6. B though Figure 3.6. D.

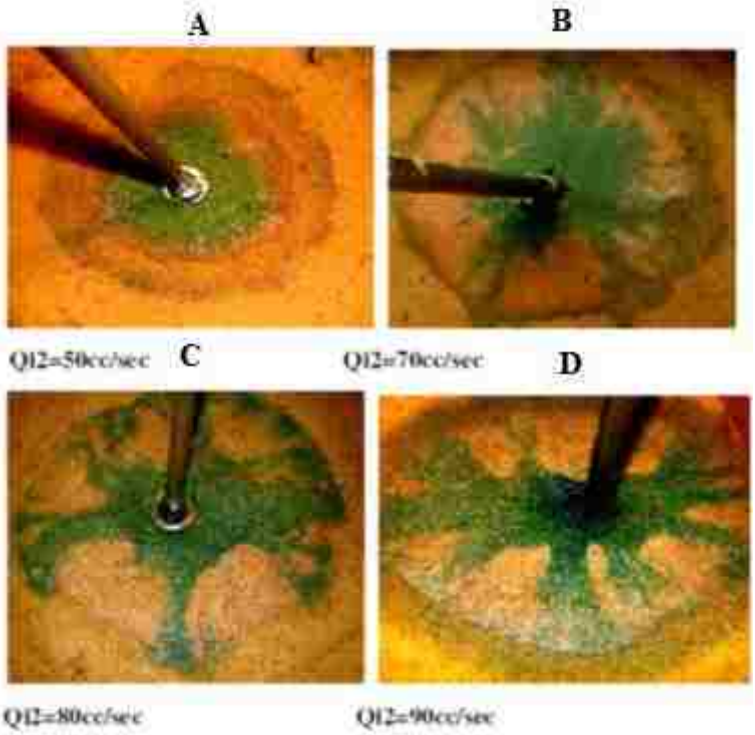

Figure 3.6. Effect of injection rate magnitude on the invaded

3.1 Numerical Methods and Model in Literature

Analytical models are limited to simple geometries and homogeneous material properties; therefore, it is essential to have a numerical solution to provide analysis for general conditions.

In most of the published works on fracture propagation at injector wells, stress singularity at the fracture tip is ignored and the fracture is mainly considered as a rectangular slot rather than incorporating a real crack geometry (Abou-Sayed et al. 2004, Sharma el al. 2000, Bedrikovetsk et al. 2001, Alote et al. 2009). Abou-Sayed et al. (2004) and Tran et al. (2010) have used Mohr-Coulomb criterion to predict fracture propagation that is implicitly a criterion for shear failure in the intact rock or along a pre-existing joint which is not a fracture propagation criterion. Silin and Patzek (2001) suggest a control model of water injection from a growing hydrofracture in a layered soft rock utilizing a modified Carter's leakoff model. They tried to show that injection pressure response depends not only on the instantaneous measurements, but also on the whole history of injection.

Alternative concepts such as viscous fingering, fluidization, and channelization have been studied for consolidated and nonconsolidated formations (Huang, 2011, Schmidt, 1994, Mahadevan, 2012). In those cases, a combination of experimental observations, continuum theory, and numerical simulations are used to solve the problem.

Finite difference method, FDM, is the most frequently used method to model fracture growth at injection sites (Gadde and Sharma 2007, Souza et al. 2005, Van den Hoek 2007, Moreno et al. 2007). FDM limits the geometry of the induced fracture to coplanar fractures. Also, due to the averaging nature of the finite difference method, grid refinement close to singularities like fracture tips become cumbersome.

Mahadevan et al. (2012) used finite volume methods (FVM). The advantage of FVM to FDM is to refer to a small node surrounding each node point on a mesh. The equations are presented in integral form which is often how they are derived from the underlying physical laws because there is no need for dependent variables to be differentiable everywhere which means that a larger class of problems can be solved.

WID model was developed by Pang, S and M. Sharma, (1994) to predict injectivity decline in injection wells. This model determines the concentration of deposited particles around the injection well as a function of time and distance from wellbore, calculates the altered permeability near the well, and it determines how near well damage changes the injectivity of the well. When particle suspension is injected into a porous medium, various forces act between particles and grains causing some particles to adhere to the pore walls. The mass conservation equation for the particles is

$$\frac{\partial(\varphi C)}{\partial t} + \mathrm{v}\frac{\partial C}{\partial x} + \frac{\partial \sigma}{\partial t} = 0 \qquad (3.1)$$

where; C is concentration of suspended particles, φ is porosity, v is superficial velocity and σ is volume concentration of particles /unit bulk volume.

The rate of particle capture function is

$$\frac{\partial \sigma}{\partial t} = \lambda \mathrm{v} C \qquad (3.2)$$

where λ is filtration coefficient and the particle concentration is given as

$$C(x) = C_{in} e^{-\lambda_0 x} \qquad (3.3)$$

$$\sigma(x,t) = \lambda C_{in} e^{-\lambda_0 x} \qquad (3.4)$$

$$\varphi(x,t) = \varphi_0 - \sigma(x,t) \qquad (3.5)$$

Where, C_{in} is particle concentration in injected fluid. λ can be derived from core experiments or estimated from empirical correlations.

$$\frac{\lambda}{\lambda_0} = (1 + b\sigma) \tag{3.6}$$

The injectivity declines as particles are trapped in the pore walls and reduce porosity and permeability. There are various relationships available in the literature which relates the decline in permeability to the concentration of deposited particles. Based on the Kozeny equation, Pang and Sharma (1997) proposed the following relation for permeability reduction due to particle plugging.

$$\mathrm{k} = \frac{\varphi^3}{K_K(1-\varphi)^2}\frac{1}{A_s^2}\frac{1}{\tau} \tag{3.7}$$

where k is the permeability, S is the specific surface area, K_K is the Kozeny constant and τ is the tortuosity. The best-fit value for factor $k' = K_K\tau$ has been found by Carman to be 5. The ratio of permeability at any instant to the initial permeability is

$$\frac{k}{k_0} = \frac{\varphi^3(1-\ \varphi_0^2)S_0^2k_0'}{\varphi_0^3(1-\ \varphi^2)S^2k'} \tag{3.8}$$

Pang and Sharma proposed that the permeability reduction could be divided into three factors: reduced porosity (k_{dp}), increased surface area (k_{ds}), and increased tortuosity (k_{dt}).

$$k/k_0 = \mathrm{k}_{dp}\mathrm{k}_{ds}\mathrm{k}_{dt} \tag{3.9}$$

where

$$\mathrm{k}_{dp} = \frac{\phi^3(1-\ \phi_0^2)}{\phi_0^3(1-\ \phi^2)} \tag{3.10}$$

G. Han et al. (2003) developed a fully coupled geomechanics model accounting for the changes of fluid pressure to quantify the effect of well shut-down on rock stability. The author presented the importance role of fluid pressure in rock deformation. In this study it has been shown that the fluid pressure not only provides a driving force to mobilize sand, but it also functions as one of the supportive forces for natural and induced loads; i.e., the effective stress in the rock matrix is affected through pressure changes, $\sigma' = \sigma - \alpha P$, where α is the Biot constant. The stress equilibrium in a cylindrical coordinate for isotropic rock with $\alpha = 1$ is calculated by

$$\frac{\partial \sigma_r}{\partial r} + \frac{\sigma_r + \sigma_\theta}{r} = \frac{\partial P}{\partial r} \qquad (3.11)$$

The deformation becomes:

$$\frac{\partial^2 u}{\partial r^2} + \frac{1}{r}\frac{\partial u}{\partial r} - \frac{u}{r^2} = \frac{E(1-\nu)}{(1+\nu)(1-2\nu)}\frac{\partial P}{\partial r} \qquad (3.12)$$

Because the pore pressure and deformation are not only dependent upon the radius, but also on time $[P = P(r,t)]$, $[u = u(r,t)]$, so equation (3.12) becomes:

$$\frac{\partial}{\partial r}\left(\frac{\partial u}{\partial r} + \frac{u}{r}\right) = \frac{(1+\nu)(1-2\nu)}{E(1-\nu)}\frac{\partial P}{\partial r} \qquad (3.13)$$

The solution of this equation can be expressed as:

$$u = \frac{C_2(t)}{r} + C_1(t) + \frac{1}{r}\frac{(1+\nu)(1-2\nu)}{E(1-\nu)}\int^r rP(r,t)dr \qquad (3.14)$$

Where $C_1(t)$, $C_2(t)$ are variables related only to time. The effective stress can be determined by:

$$\sigma_r' = P + \frac{EC_1(t)}{(1+\nu)(1-2\nu)} - \frac{EC_2(t)}{(1+\nu)}\frac{1}{r^2} - \frac{(1-2\nu)}{(1-\nu)}\frac{1}{r^2}\int^r rP(r,t)dr \quad (3.15)$$

$$\sigma_\theta' = \frac{\nu}{1-\nu}P + \frac{EC_1(t)}{(1+\nu)(1-2\nu)} - \frac{EC_2(t)}{(1+\nu)}\frac{1}{r^2} - \frac{(1-2\nu)}{(1-\nu)}\frac{1}{r^2}\int^r rP(r,t)dr \quad (3.16)$$

And total stresses ($\sigma = \sigma' + P$) are :

$$\sigma_r = 2P + \frac{EC_1(t)}{(1+\nu)(1-2\nu)} - \frac{EC_2(t)}{(1+\nu)}\frac{1}{r^2} - \frac{(1-2\nu)}{(1-\nu)}\frac{1}{r^2}\int^r rP(r,t)dr \quad (3.17)$$

$$\sigma_\theta' = \frac{1}{1-\nu}P + \frac{EC_1(t)}{(1+\nu)(1-2\nu)} - \frac{EC_2(t)}{(1+\nu)}\frac{1}{r^2} - \frac{(1-2\nu)}{(1-\nu)}\frac{1}{r^2}\int^r rP(r,t)dr \quad (3.18)$$

In the above equation, $P(r,t)$ is determined by:

$$P(r,t) = P_e\left[A + B\sum_{n=1}^{\infty} C_n\, D_n(t) J_0\left(\lambda_n \frac{r}{R_e}\right)\right] \quad (3.19)$$

Where:

$$A = 1 - \frac{1}{2}.\frac{1 - P_w/P_e}{\ln(R_e/R_w)} \quad (3.20)$$

$$B = \frac{Q\mu}{\pi khP_e} \quad (3.21)$$

$$C_n = \frac{1 - J_0(\lambda_n)}{\lambda_n^2 \, J_0(\lambda_n) J_2(\lambda_n)} \quad (3.22)$$

$$D_n(t) = exp\left(-\frac{kR_e^2}{C\mu}\right)\lambda_n^2 t \quad (3.23)$$

The fluid pressure integral is:

$$\int^r rP(r,t)dr = P_e\left[\frac{A}{2} + B\sum_{n=1}^{\infty} C_n D_n(t)\frac{R_e}{\lambda_n}.rJ_1\left(\lambda_n\frac{r}{R_e}\right)\right] \quad (3.24)$$

Applying boundary conditions into equation (3.24):

$$r = R_w, \qquad \sigma_r = P_w(t)$$
$$r = R_e \ (when \ R_e \gg R_w), \qquad \sigma_r = \sigma_h \quad (3.25)$$

The two unknown parameters $C_1(t), C_2(t)$ can be solved:

$$C_1(t) = \frac{(1+\nu)(1-2\nu)}{E}\left[-P_w(t) + \frac{EC_2(t)}{(1+\nu)}\frac{1}{R_w^2} + \frac{1-2\nu}{1-\nu}\frac{A}{2}P_e\right] \quad (3.26)$$

$$C_2(t) = \frac{(1+\nu)}{E}[\sigma_h - 2P_e(t) + P_w(t)].\frac{R_w^2 R_e^2}{R_e^2 - R_w^2} \quad (3.27)$$

Where from equation (3.19):

$$P_w(t) = P_e\left[A + B\sum_{n=1}^{\infty} C_n\, D_n(t)\right] \quad (3.28)$$

$$P_e(t) = P_e\left[A + B\sum_{n=1}^{\infty} C_n\, D_n(t) J_0\left(\lambda_n \frac{R_e - R_w}{R_e}\right)\right] \quad (3.29)$$

3.2 Case study

Sharma et al. (2000) have studied and presented well A10 from the Gulf of Mexico, where injection occurs in an unconsolidated formation. The injection history of well A10 is shown in Figure 3.7. In the injection life of this well, several acid treatments were conducted and resulted in a significant increase in the injectivity of the well. However, injectivity immediately begins to drop and the injectivity decline profile seen is similar to that observed during the first stage on injection.

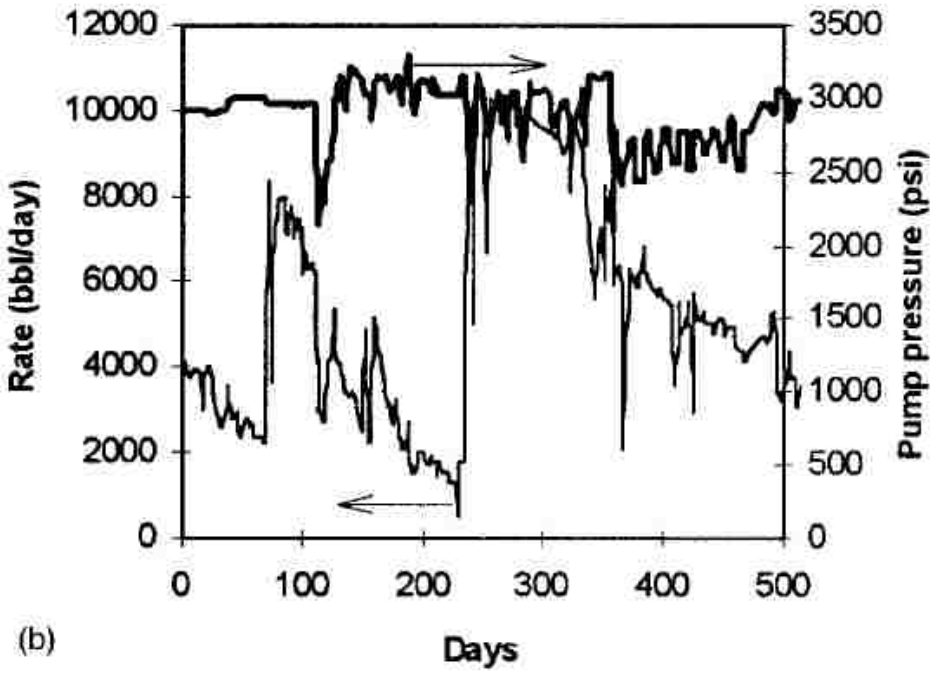

Figure 3.7. Injection history of well A10.

Bain (2013) have examined a number of injection cases where the benefits of adequate fracture closure and the detrimental impacts of insufficient fracture closure are respectively revealed. Figure 3.8

shows the pressure decline in four different injection wells for the different injection cases. The pressure decline for all the wells follows the same trend.

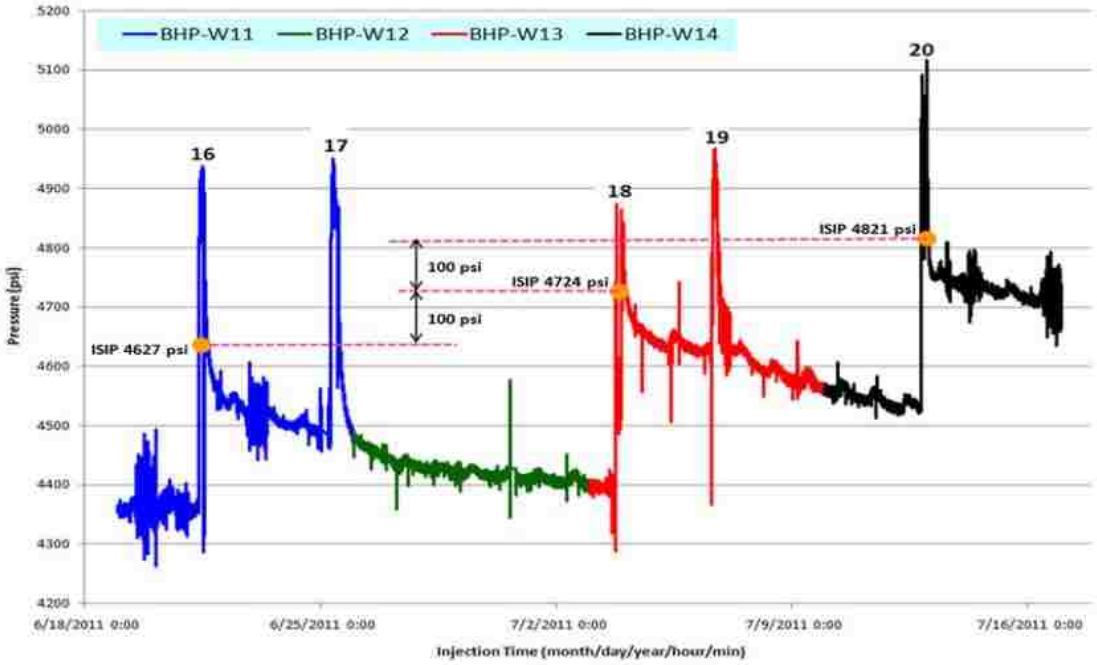

Figure 3.8. BHP for 4 wells (Bai, 2013)

Chapter 3: Erosional Channelization in Unconsolidated Sands

Among fragmental rocks, sandstone, conglomerates, arkoses, gray-wakes, and siltstones are the most common reservoir rocks, and these sediments constitute nearly half of the reservoir rocks (Levorsen, 1967). Most of these fragmental reservoir rocks are slightly cemented or recrystallized. These types of cohesion-less reservoirs with weak grain matrix are called unconsolidated formations, which are capable of releasing part of the matrix during production or injection. Production issues in unconsolidated formations are commonly addressed as sand control problems rather than formation damage, however, the effect of mobile sand and the pressure drop caused by collapsed formation channels closely corresponds to the effects of formation damage (Economides, 2000).

Flow through a saturated, granular porous medium can lead to movement of the fines in the formation in response to flow velocity and in some cases due to salinity of the formation fluid. In porous media, large variation of hydraulic conductivity will result from large flow-rates. This variation of conductivity and heterogeneity is strongly dependent on the formation and consolidation of the porous medium via grains allocation. Depending on their particle size, they can either block pore throats in the vicinity of their initial location or migrate toward the wellbore. Whether migrating particles reach the wellbore or deposit and bridge over the pore throat entrance depends on their original concentration in the formation, their size, and the maximum flow rate (Economides, 2000).

Injection at a high rate is required for economic waterflooding projects. Waterflooding in unconsolidated sand may lead to fracture or channel initiation and their subsequent propagation (Khodaverdian, 2010). Channelization in these formations happens when the local fluid-induced stress is larger than a critical threshold; grains are dislodged and carried away so that the porosity of the medium is altered by erosion (Mahadevan, 2012). Continuous particle washout will impact local hydraulic conductivity and pressure distribution in the formation, which may result in formation of channels as preferential paths to conduct the flow. Although channeling enhances permeability and injectivity of the

wellbore, channel initiation and its growth must be under control to avoid solid production in injectors in case of emergency shut-down due to power cut-off or any natural disasters. Rapid shut-down results in a water hammer, eventually, injectors that experience frequent rapid shutdown often have significantly reduced injectivity and show evidence of sanding and even failure of the downhole completion (Tang, 2010).

Sanding criteria can be divided into tensile failure and shear failure with hydrodynamic erosion. These components follow the general observation from literature reviews:

1. Tensile failure occurs when the radial pore pressure gradient exceeds the radial stress gradient on the granular surface. It is assumed that this causes immediate particle movement if there is any flow.

2. Shear failure occurs according to the Mohr-Coulomb failure criterion and leads to a weakening of the matrix. Given a sufficient pore pressure gradient, grains detach and erode away from the matrix.

4.1 Factors that lead to sanding

In injectors, there is no depletion, so any rock dislodgement would be the result of near-wellbore degradation caused by high injection rate, which may lead to shear failure that result in channelization and the pressure cycles associated with repeated shutdowns and WH effects. Sanding occurs over only the short periods immediately after a shutdown while cross flow or back flow, along with any WH pulses, will happen (Vaziri, 2008).

Cycles of Injection and Shutdown: Increase in pressure results in reduction in effective stress and thus, a reduction in particle to particle frictional resistance. In unconsolidated sand seams or disaggregated sand particles adjacent to well, this condition may exacerbate sanding right after shut in depending on the injection magnitude and the severity of WH pressure pulses.(Vaziri, 2008)

In weakly consolidated formations, injection and shut-in cycles may result in the destruction of cementation matrix and turn the material into an unconsolidated-sand mass. The magnitude of injection rate has a considerable effect on the rate of rock de-cementation and the rate of sanding.

Crossflow: The two types of cross-flow are interwell and interlayer. Interwell crossflow may occur when a well within a network of injectors is shut-in, creating a pressure differential resulting in flow being directed from the surrounding injectors toward the shut-in well. The second type of crossflow may occur when the permeability of a layer is higher than another layer. Permeability difference results in an increase in pressure in the lower-permeability zones immediately after shut-down, leading to flow toward the higher permeability and lower pressure zones. The inflow pressure gradient may be sufficient to create sanding until the pressure equilibrates sufficiently (Vaziri, 2008).

Flow-back: Flowback can happen in two cases. First, possible loss in wellbore pressure can result in imbalance pressure between the formation fluid pressure and wellbore pressure. Second, Flowback may be due to decomposition pressure pulse, which is created following injection operation shut-down. In a short period, inflow may occur as a result of pressure differential between the well and the formation. Intensity of the pressure gradient will depend on the injection pressure before shut-in, permeability, rate of shut in, wellbore diameter, and other factors.

Water-Induced Strength Reduction: Chemical reaction can be triggered by incompatibility in temperature, density, and concentration of active ions of the injected water and the reservoir fluids. Chemical reactions can lead to dissolution and weakening of cementation of rock, particularly if the clay is rich, and this can completely destroy marginal cementations that usually exist in rocks that break down into multigrain clusters.

The mechanical damage from the injection, in which the formation is subjected to very high seepage forces, particularly in C&P completions where flow is channeled, is expected to damage rock fabric in vicinity of the injection source.

WH Pressure Pulses: Rapid shutdowns that may occur because of emergencies and loss of power results in WH effects, which is an unsteady flow of water in tubing.

4.2 Governing Equations

In this section, the governing equations for fluid flow, rock deformation, thermal conduction, and convection at the vicinity of injector wells are described. The governing equations are

Darcy's law for fluid flow:

$$q = -D\nabla \mathrm{p} \tag{4.1}$$

where D is hydraulic conductivity base on definition of Carmen-kozeny relationship is function of porosity and is equal to $D = \frac{\varphi^3 l_g^2}{A\mu\,(1-\varphi^2)}$ φ is porosity, μ is dynamic viscosity.

Force equilibrium in absence of body force:

$$\sigma_{\,ij,\,j} = 0 \tag{4.2}$$

Mass conservation for fluid:

$$\frac{\partial \rho}{\partial t} + \nabla.(\rho \vec{u}) = 0 \tag{4.3}$$

Continuity equation:

$$\frac{\partial \rho}{\partial t} + \rho \nabla.\,\mathrm{u} = 0 \tag{4.4}$$

To solve for fluid flow in the medium subject to erosion, equations (4.2) through (4.1) should be solved simultaneously. These equations could be solved using coupled or uncoupled approach, but for the general case, a tool is required to solve these equations numerically. Finite element methods (FEM), finite volume methods (FVM), finite difference methods (FDM) and discrete element methods (DEM) are the common techniques to solve a system of differential equations. Each of these methods has their inherent advantages and disadvantages. For this specific problem, we preferred not to use finite difference because the fluid flow type problem is coupled with particle motions. Finite volume method is more flexible and accurate for complex geometries since in FVM, we solve the problem in a control volume in space, but in FDM you concentrate on one point and see how it changing due to neighboring points in space. FVM is discussed in detail in Chapter 4. Techniques derived from discrete element methods consider particles explicitly but due the small size of sand particles, it requires a very large model i.e. huge computational effort to solve this problem. Finite element methods (FEM) were not selected to tackle this problem because FEM is normally applied to structural analysis which in computational fluid dynamics FVM is more applicable.

4.3 Finite Volume Methods

Finite volume methods (FVM) is used to solve equations listed in the previous section. In finite volume methods the domain is divided up into a number of control volumes, with the value at the center of the control volume being held to be representative for the value over the entire control volume. By integrating the original PDE over the control volume the equation is cast into a form that ensures conservation. The derivatives at the faces of the volume are approximated by finite difference equations. The advantage of FVM to FDM is refer to small node surrounding each node, the equations are presented in the integral form which is often how they are derived in the weak form from underlying physical laws. Hence, there is no need for dependent variables to be differentiable everywhere which means that a larger class of problems can be solved. In Figure 4.1 a rectangular domain of length L_x in x-direction and L_y in

y-direction has been shown. The domain is divided into non-overlapping control volumes by lines that define the boundary of individual control volume. At the center of each control volume is a node designated with an open circle. In code implementation the grid lines that define node locations will be stored in the variables x (i) and y (j). The grid lines that define node locations will be stored in xu (i) and yv (j).

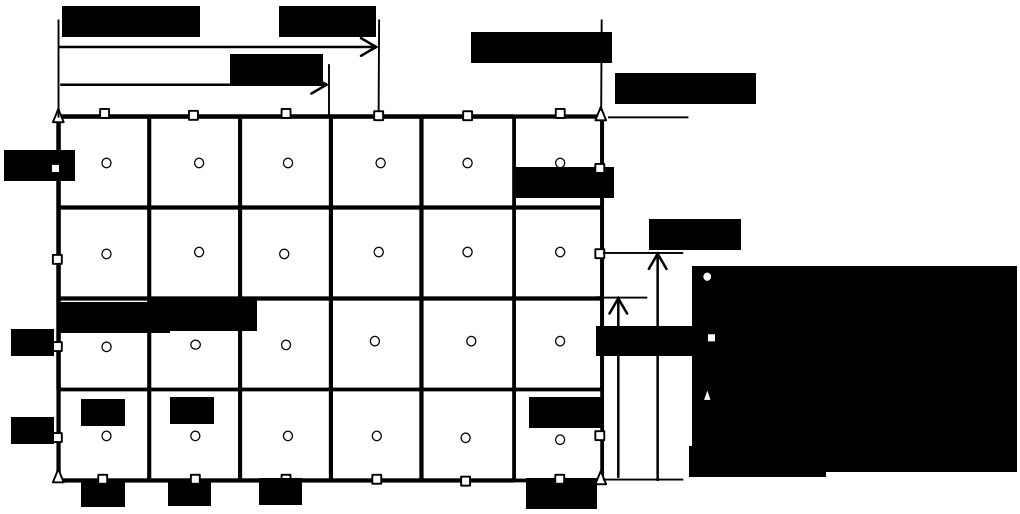

Figure 4.1. Control-volume finite-difference grid with node numbering on the interior, boundary corners

Nodes in the domain are identified by their (i, j) grid indices. A typical node in Figure 4.2 is referred to as P. The (i + 1, j) and (i - 1, j) neighbors of P are designated E for east and W for west, respectively. The (i, j+1) and (i, j-1) neighbors of P are referred to as N and S for north and south neighbors, respectively.

In general, the width, Δx, of the control volume will not be equal to the distance δx_e and δx_w between P and its east and west neighbors. Regardless of grid spacing, P is always located in the geometric center of the control volume. Therefore

$$x_P - x_w = x_e - x_P = x = \frac{\Delta x}{2} \text{ and}$$

$$x_P - x_s = x_n - x_P = x = \frac{\Delta y}{2},$$

where in these expressions, lower case subscripts refer to the location of control volume faces and upper subscripts refer to the location of the nodes.

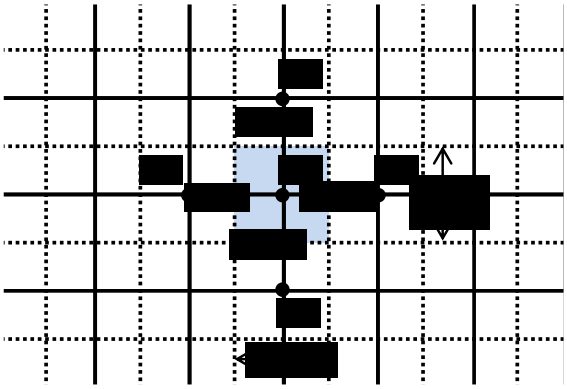

Figure 4.2. A part of the two-dimensional grids with a control volume

4.4 The Erosion Model

The basis of the model developed for motion of sand particles due to erosion is defined in the context of continuum mechanics. In order to correctly account for the early stages of erosion and its evolution, a multiphase theory consisting of fluids, mobile and immobile granular phases have been proposed. In this section, a brief description of the model and equations used to simulate fluid-induced channelization in the porous medium is described.

For continuum description of the process, we consider a representative volume much larger than the grain/pore size with $\varphi_s + \varphi_g + \varphi_l = 1.0$, where, φ_s is the volume fraction of immobile solid phase, φ_g is the volume fraction of granular mobile phase, and φ_l is the liquid volume fraction in the medium

(Mahadevan, 2012). The time-evolution of these phases is described by accounting for the transport of liquid and granular phases by velocities u_l and u_g, respectively. The transformation between the three mentioned phases is governed by erosion and deposition criteria. The mass conservation for each individual phase (which is assumed to be incompressible) leads to

$$\partial_t \varphi_s = -e + d \tag{4.5}$$

$$\partial_t \varphi_g = +e - d - \nabla.(\varphi_g u_g) \tag{4.6}$$

$$\partial_t \varphi_l = -\partial_t(\varphi_s + \varphi_g) = -\nabla.(\varphi_l u_l) \tag{4.7}$$

where, e is the rate of transformation of immobile phase to mobile phase, d is the rate of deposition or conversion of mobile phase to immobile phase. u_g and u_l are the velocities of granular and liquid phases, respectively. Adding equations (4.5) - (4.7) yields the global continuity equation

$$\nabla.(\varphi_g u_g + \varphi_l u_l) = 0 \tag{4.8}$$

For simplicity, we assume that $u_g = u_l = u$, i.e. the granular and liquid phase have the same velocity, in other words, the effect of inertia and body forces for sedimentation is considered to be negligible, which is a reasonable approximation for nearly jammed grains. Then, the continuity equation reduces to $\nabla.\ \phi$ u=0, where $\phi = \phi_g + \phi_l$ (Mahadevan, 2012). The local erosion rate e is

$$e = k_e \varphi_s((\gamma^{-1}\nabla p)^2 - \sigma) \geq 0 \tag{4.9}$$

where, k_e is the characteristic rate of erosion and γ is the nominal pressure gradient, which is equal to ration of the characteristic specific discharge to the characteristic hydraulic conductivity. Failure stress as a function of average volume fraction is described as (Mahadevan, 2012)

$$\sigma = 2 * (\tanh\left(2\pi(\overline{\varphi_s} - 0.6)\right) + 1), \tag{4.10}$$

where, $0 \leq \overline{\varphi_s} \leq 1$ which mimics the sharp dependence of the granular failure stress σ on the volume fraction of immobile phase as shown in Figure 4.3. The weighted spatial average of φ_s, is calculated numerically as

$$\begin{aligned}\overline{\varphi_s}(i,j) = 0.25\varphi_s(i,j) + 0.125(\varphi_s(i+1,j) + \\ \varphi_s(i,j+1) + \varphi_s(i-1,j) + \varphi_s(i,j-1)) + 0.625(\varphi_s(i + \\ 1,j+1) + \varphi_s(i+1,j-1) + \varphi_s(i-1,j-1) + \varphi_s(i - \\ 1,j+1))\end{aligned} \tag{4.11}$$

Equation (4.11) represents an averaging over the 8 neighbors of a grid point values located in a radius of influence of the stress that includes a few grain diameters, in contrast of using a local value of φ_s , which leads to erosion at individual grid cells. Figure 4.3 shows the dependency of each node on 8 neighbors of a grid point.

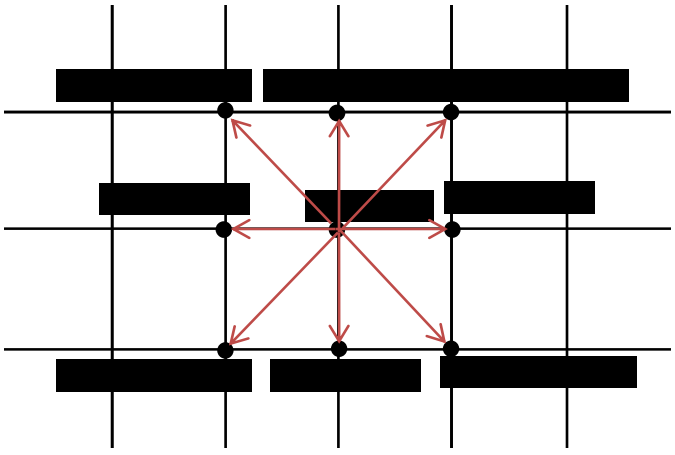

Figure 4.3. Dependency of each node on 8 neighbors

To estimate deposition, the rate at which the mobile granular grains transformed back to an immobile solid phase is given by (Mahadevan, 2012)

$$d = k_d\,(\varphi_s - \varphi_s^*)\,\varphi_g, where\ d \geq 0 \tag{4.12}$$

The characteristic deposition rate, k_d is taken as characteristic specific discharge divided by length scale:

$$k_d = k_e = \frac{q_0}{L} \tag{4.13}$$

The specific discharge for flow in porous medium is given by Darcy's law

$$q = u(\varphi_l + \varphi_g) = u\varphi = -D_\varphi \nabla p \tag{4.14}$$

$$\text{where, } D = \frac{\varphi^3\, l_g^2}{A\mu\,(1-\varphi)^2} \tag{4.15}$$

Here, *D* is the hydraulic conductivity and is assumed to follow Carmen-Kozeny relationship (4.15) and is in general a nonlinear function of local fluid (pore) volume fraction $\varphi = \varphi_l + \varphi_g$. The parameter, l_g is nominal pore size, μ is the dynamic viscosity of interstitial fluid. Parameter *A* is a dimensionless constant, which is calculated using equation (1.1) by considering the effect of flow path (tortuosity) on A (Carmen, 1937).

$$A = \Phi\left(\frac{L_e}{L}\right)^2 \tag{4.16}$$

Where Φ is the pore shape factor, L_e/L is tortuosity which is defined as the average effective streamline length,L_e scaled by the system length, L. For a constant tortuosity ($L_e/L = \sqrt{2}$) and shape factor, $\Phi = 90$. Therefore A is 180.

4.5 Finite Volume Discretization of the Governing Equations

The key step in the finite volume method is the integration of the governing equations over a control volume to yield a discretized equation at its nodal point *P*, as it shown in Figure 4.2. By substituting equation (4.14) into global continuity equation (4.8) we will obtain Poisson's equation (4.17).

The pressure in the domain is calculated by solving Poisson's equation by assuming initial condition for porosity and having a heterogeneous formation using an additive white Gaussian noise (standard deviation $sd = \sqrt{\langle \varphi_l^2 \rangle - \langle \varphi_l \rangle^2} = 0.01$).

$$\nabla.(D\,\nabla P) = 0 \tag{4.17}$$

where

$$D = \frac{\varphi^3 l_p^2}{A\,\mu\,(1-\varphi)^2} \tag{4.18}$$

$$q \equiv \varphi\, u = -D\nabla P$$

$$\frac{\partial}{\partial x}\left(D\,\frac{\partial P}{\partial x}\right) + \frac{\partial}{\partial y}\left(D\,\frac{\partial P}{\partial y}\right) = 0 \tag{4.19}$$

where q is the flux (discharge per unit area, with units of length per time, m/s) and ∇P is the pressure gradient vector (*Pa/m*). This value of flux, often referred to as the Darcy flux, is not the velocity which the liquid traveling through the pores is experiencing. The pore velocity (u) is related to the Darcy flux (q) by the porosity (n). The flux is divided by porosity to account for the fact that only a fraction of the total formation volume is available for flow. The pore velocity is the velocity that a conservative tracer would experience if carried by the fluid through the formation.

By integrating equation (4.19) over the control volume in two dimensions, it reduces to an equation that involves only first derivatives in space. Then these first derivatives are replaced with a central difference approximation using the discretization format that is demonstrated in Figure 4.2.

$$\int_{\Delta V} \frac{\partial}{\partial x}\left(D\ \frac{\partial P}{\partial x}\right) dxdy + \int_{\Delta V} \frac{\partial}{\partial y}\left(D\ \frac{\partial P}{\partial y}\right) dxdy = 0 \tag{4.20}$$

Using notation for neighbors of general grid node *P*, as east (E), west (W), north (N) and south (S) as it shown in Figure 4.2, equation (4.20) can be simplified to

$$\left[D_e\ A_e \left(\frac{\partial P}{\partial x}\right)_e - D_w\ A_w \left(\frac{\partial P}{\partial x}\right)_w\right] + \left[D_n\ A_n \left(\frac{\partial P}{\partial y}\right)_n - D_s\ A_s \left(\frac{\partial P}{\partial y}\right)_s\right] = 0 \tag{4.21}$$

The above equation represents the balance pressure in a control volume and the fluxes through cell faces. Using the approximations that $A_e = A_w = \Delta y$ and $A_n = A_s = \Delta x$ the following expressions for the flux through control volume faces can be obtained

Flux across the east face $$D_e\ A_e \left(\frac{\partial P}{\partial x}\right)_e = D_e\ A_e \left(\frac{P_E - P_P}{\delta x_{PE}}\right) \tag{4.22}$$

Flux across the west face $$D_w\ A_w \left(\frac{\partial P}{\partial x}\right)_w = D_w\ A_w \left(\frac{P_P - P_W}{\delta x_{PW}}\right) \tag{4.23}$$

Flux across the north face $$D_n\ A_n \left(\frac{\partial P}{\partial x}\right)_n = D_n\ A_n \left(\frac{P_N - P_P}{\delta y_{NP}}\right) \tag{4.24}$$

Flux across the south face $$D_s A_s \left(\frac{\partial P}{\partial x}\right)_s = D_s A_s \left(\frac{P_P - P_S}{\delta y_{PS}}\right) \quad (4.25)$$

By substituting the above expressions into equation (4.21) we obtain

$$D_e A_e \left(\frac{P_E - P_P}{\delta x_{PE}}\right) - D_w A_w \left(\frac{P_P - P_W}{\delta x_{PW}}\right) + D_n A_n \left(\frac{P_N - P_P}{\delta y_{NP}}\right) - D_s A_s \left(\frac{P_P - P_S}{\delta y_{PS}}\right) = 0 \quad (4.26)$$

This equation can be rearranged to

$$\left(\frac{D_e A_e}{\delta x_{PE}} + \frac{D_w A_w}{\delta x_{WP}} + \frac{D_n A_n}{\delta y_{NP}} + \frac{D_s A_s}{\delta y_{PS}}\right) P_P = \left(\frac{D_e A_e}{\delta x_{PE}}\right) P_E + \left(\frac{D_w A_w}{\delta x_{WP}}\right) P_W + \left(\frac{D_n A_n}{\delta y_{NP}}\right) P_N + \left(\frac{D_s A_s}{\delta y_{PS}}\right) P_S \quad (4.27)$$

Equation (4.27) is now put in general discretized equation form for interior nodes as:

$$a_P P_P = a_E P_E + a_W P_W + a_N P_N + a_S P_S \quad (4.28)$$

where

a_E	a_W	a_N	a_S	a_p
$\frac{D_e A_e}{\delta x_{PE}}$	$\frac{D_w A_w}{\delta x_{WP}}$	$\frac{D_n A_n}{\delta y_{NP}}$	$\frac{D_s A_s}{\delta y_{PS}}$	$a_E + a_W + a_N + a_S$

4.5.1 Non-uniform Hydraulic Conductivity, D

Calculation of the above coefficients, require a value of *D* at the interfaces of the control volumes. Instead of using an interpolation scheme, the interface value of D can be defined by requiring the diffusive flux at the control volume interfaces to be a situation where two control volumes meet along a material discontinuity as it shown in Figure 4.4 which shows discontinuous variation in D at the interface between two control-volumes. By assuming that D is uniform within each of the control volumes, continuity of flux at the interface requires

$$D_P \left.\frac{\partial P}{\partial x}\right|_{x_e^-} = D_E \left.\frac{\partial P}{\partial x}\right|_{x_e^+} = D_e \left.\frac{\partial P}{\partial x}\right|_{x_e} \tag{4.29}$$

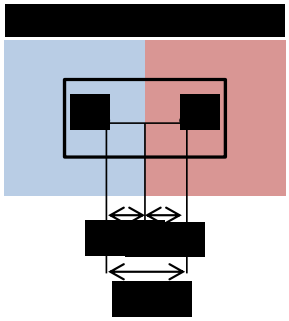

Figure 4.4: Discontinuous variation in D at the interface between two control-volumes

Equation (4.29) defines D_e in a way that the value of D_e is chosen such that the flux, $\partial P/\partial x$, is continuous. The central difference approximation to the flux continuity conditions in equation (4.29) are

$$D_e \left(\frac{P_E - P_P}{\delta x_e}\right) = D_P \left(\frac{P_e - P_P}{\delta x_{e^-}}\right) \tag{4.30}$$

$$D_e \left(\frac{P_E - P_P}{\delta x_e}\right) = D_E \left(\frac{P_E - P_e}{\delta x_{e+}}\right) \tag{4.31}$$

where P_e is the value of P at interface. Equation (4.30) and (4.31) are the discrete approximations for the diffusion into the left (minus) and right (plus) sides of the control volume in Figure 4.4. These equations can be rearranged as

$$P_e - P_P = \frac{\delta x_{e-}}{D_P} \frac{D_e}{\delta x_e} (P_E - P_P) \tag{4.32}$$

$$P_E - P_e = \frac{\delta x_{e+}}{D_E} \frac{D_e}{\delta x_e} (P_E - P_P) \tag{4.33}$$

Adding equation (4.32) and (4.33) gives

$$P_E - P_P = \frac{D_e}{\delta x_e} (P_E - P_P) \left[\frac{\delta x_{e-}}{D_P} + \frac{\delta x_{e+}}{D_E}\right] \tag{4.34}$$

By canceling the term $(P_E - P_P)$ and solve for $D_e / \delta x_e$ we get

$$\frac{D_e}{\delta x_e} = \left[\frac{\delta x_{e-}}{D_P} + \frac{\delta x_{e+}}{D_E}\right]^{-1} = \frac{D_E D_P}{\delta x_{e-} D_E + \delta x_{e+} D_P} \tag{4.35}$$

thus,

$$D_e = \frac{D_E D_P}{\beta D_E + (1 - \beta) D_P} \tag{4.36}$$

where

$$\beta = \frac{\delta x_{e^-}}{\delta x_e} = \frac{x_e - x_P}{x_E - x_P} \tag{4.37}$$

Using similar concept used for east interface (D_e), hydraulic conductivity for west interface (D_w) is estimated as

$$D_P \left.\frac{\partial P}{\partial x}\right|_{x_w^+} = D_W \left.\frac{\partial P}{\partial x}\right|_{x_w^-} = D_w \left.\frac{\partial P}{\partial x}\right|_{x_w} \tag{4.38}$$

Equation (4.38) defines D_w . In other words, the value of D_w is chosen such that the flux, $D\,\partial P/\partial x$, is continuous. The central difference approximation to the flux continuity conditions in equation (4.38) are

$$D_w \left(\frac{P_P - P_W}{\delta x_w}\right) = D_P \left(\frac{P_P - P_w}{\delta x_{w^+}}\right) \tag{4.39}$$

$$D_w \left(\frac{P_P - P_W}{\delta x_w}\right) = D_W \left(\frac{P_w - P_W}{\delta x_{w^-}}\right) \tag{4.40}$$

where P_w is the value of P at interface. Equations (4.39) and (4.40) are the discrete approximations for the diffusion into the left (minus) and right (plus) sides of the control volume in Figure 4.4. These equations can be rearranged as

$$P_P - P_w = \frac{\delta x_{w^+}}{D_P}\frac{D_w}{\delta x_w}(P_P - P_W) \tag{4.41}$$

$$P_w - P_W = \frac{\delta x_{w^-}}{D_W}\frac{D_w}{\delta x_w}(P_P - P_W) \tag{4.42}$$

Adding equations (4.41) and (4.42) gives

$$P_P - P_W = \frac{D_w}{\delta x_w}(P_P - P_W)\left[\frac{\delta x_{w^+}}{D_P} + \frac{\delta x_{w^-}}{D_E}\right] \tag{4.43}$$

By canceling the term $(P_P - P_W)$ and solve for $D_w\ /\delta x_w$ we get

$$\frac{D_w}{\delta x_w} = \left[\frac{\delta x_{w^+}}{D_P} + \frac{\delta x_{w^-}}{D_E}\right]^{-1} = \frac{D_W D_P}{\delta x_{e^+} D_W + \delta x_{e^-} D_P} \tag{4.44}$$

Thus,

$$D_w = \frac{D_W D_P}{\beta D_W + (1-\beta) D_P} \tag{4.45}$$

where

$$\beta = \frac{\delta x_{w^-}}{\delta x_w} = \frac{x_P - x_w}{x_P - x_W} \tag{4.46}$$

For north and south neighbors using similar terminology, we will obtain

$$D_n = \frac{D_N D_P}{\beta D_N + (1-\beta) D_P} \tag{4.47}$$

$$\beta = \frac{\delta x_{n^-}}{\delta x_n} = \frac{x_n - x_P}{x_N - x_P} \tag{4.48}$$

$$D_s = \frac{D_S D_P}{\beta D_S + (1-\beta) D_P} \tag{4.49}$$

$$\beta = \frac{\delta x_{s^-}}{\delta x_s} = \frac{x_P - x_s}{x_P - x_S} \tag{4.50}$$

The pressure at interior node *P*, knowing all the coefficients evaluated above, can be calculated by

$$P_P = \frac{a_E * P_E + a_W * P_W + a_N * P_N + a_S * P_S}{a_p} \tag{4.51}$$

4.5.2 Staggered grid

Staggered grid combines several types of nodal points located in different geometrical positions. Staggered grid allows for very natural and accurate formulation of several crucial partial differential equations (such as Stokes and continuity equations).

After discretizing the governing equation using the finite volume method in the previous section, we need to decide where to store our variables other than pressure in the numerical grid. Since we stored the scalar variable pressure in the main node (*P*), it seems logical to define velocities at the same nodes. However, if velocities and pressures are both defined at the same node of a control volume, a highly non-uniform pressure field can act like a uniform filed in the discretized momentum equations (Versteeg, 2007). A solution to this problem is to use a staggered grid for velocity components. The idea is to evaluate scalar variables, such as pressure at ordinary nodal points but to calculate velocity components on staggered grids centered on the cell faces. In Figure 4.5, the scalar variables, including pressure, are stored at the nodes marked (●). The velocities are defined at the interface of the control volume between the nodes and are indicated by ( ) for velocity in x direction and ( ) for velocity in y direction.

Using the *E*, *W*, *N*, *S* notations; the velocity in x-direction are stored at cell face *e* and *w* and the velocity in y-direction are stored at cell face *n* and *s*.

In the staggered grid, the pressure gradient is also located at the cell faces of the control volume. The pressure gradient term $\partial p/\partial x$ is given by

$$\frac{\partial p}{\partial x} = \frac{P_P - P_W}{\delta x_u} \tag{4.52}$$

where δx_u is the width of the u-control volume. Likewise $\partial p/\partial y$ for the v-control volume is given by

$$\frac{\partial p}{\partial x} = \frac{P_P - P_S}{\delta y_v} \tag{4.53}$$

where δy_v is the width of the v-control volume.

In general, "complex" staggered grid often allows for very elegant and accurate discretization of equations and provides the most simple and natural geometry of grid stencils needed for different equations that should be solved simultaneously.

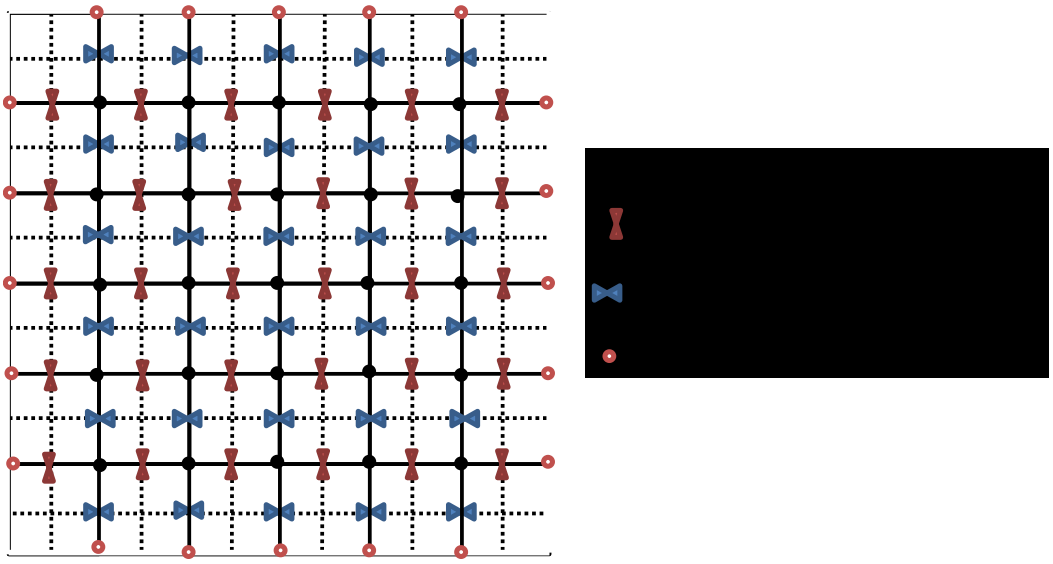

Figure 4.5. Staggered grid used in model

4.5.3 Type of Boundary Condition

Neumann boundary: In this model, flow injection rate is set at the bottom boundary, Neumann boundary (NBC), at inlet, and enforce constant uniform pressure (Dirichlet boundary condition (DBC)) at the outlet. NBC is set as a specific constant flow rate at the ghost nodes shown in Figure 4.5. The ghost nodes in Figure 4.5 are shown on four boundaries with red dots (⊙).

Dirichlet boundary: For DBC, we set a fixed pressure condition in the ghost nodes at the outlet. The ghost nodes approach (Leveque, 2004) is used to avoid discontinuous derivatives across the boundary and allow the real nodes on the boundary to access the extended boundary or so-called ghost cells.

Periodic boundary: In the direction normal to the flow, the periodic or cyclic boundary condition (PBC) is used to periodically extend the lattice to model a large system by solving the equations for a small region, which is far from the edges. Periodic boundary conditions are well described in Chapter 3.To apply periodic boundary conditions, we need to set the flux of all flow variables at the east boundary equal to the flux variables at the west boundary. This is achieved by equating the values of each variable at the ghost nodes of east to the associated nodal ghost values of west as shown in Figure 4.5. Updating flow rate at the first node, Q_1 , requires values Q_0 from the left and Q_2 for the right (Figure 4.6). In the case of PBC, the value Q_0 should be equal to the value Q_N instead of Q_{i-1} that would normally be used for $i > 1$. However, it is simpler to use ghost cell's approach and simply set $Q_0^n = Q_N^n$ before computing fluxes and updating the cell values (Leveque, 2004). This formulation for a five-point stencil in a two dimensional grid can be derived as follow

$$Q_{-1}^n = Q_{N-1}^n,\ Q_0^n = Q_N^n,\ Q_{N+1}^n = Q_1^n, Q_{N+2}^n = Q_2^n \tag{4.54}$$

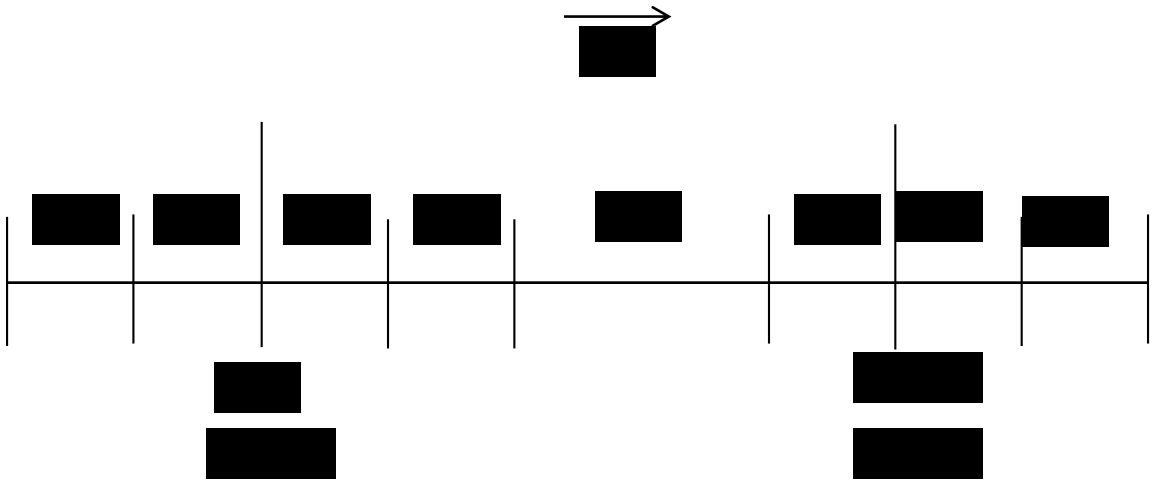

Figure 4.6. The scheme for considering flow boundary condition is shown for a typical one-dimensional domain [a, b], which is extended to include ghost cells (Q_{-1}, Q_0, Q_N, Q_{N+1}).

4.5.4 Discretization of Transport Equations

In this section, we describe the finite volume discretization of erosion and deposition equation and also the erosion criteria which have critical impact on the model.

The erosion rate is given by

$$e = k_e \, \varphi_s \, ((\gamma^{-1}\nabla \mathrm{p})^2 - \sigma) \geq 0 \tag{4.55}$$

Where

$$\gamma = \frac{q_0}{D_0} \tag{4.56}$$

Note that in above equation, γ is a scalar

$$\nabla \mathrm{p} = \frac{\partial P}{\partial x}\hat{\imath} + \frac{\partial P}{\partial y}\hat{\jmath} \tag{4.57}$$

$$\nabla \mathrm{p} = \left(\frac{P_E - P_W}{2\delta x_{EW}}\right)\hat{\imath} + \left(\frac{P_N - P_S}{2\delta x_{NS}}\right)\hat{\jmath} \tag{4.58}$$

$$(\gamma^{-1}\nabla \mathrm{p})^2 = \gamma^{-2}\left[\left(\frac{P_E - P_W}{2\delta x_{EW}}\right)^2 + \left(\frac{P_N - P_S}{2\delta x_{NS}}\right)^2\right] \tag{4.59}$$

$$\sigma = 0.5(\tanh(2\pi(\bar{\varphi}_s - 0.6) + 1) \tag{4.60}$$

$$0 \leq \bar{\varphi}_s \leq 1$$

$$\bar{\varphi}_s(i,j) = 0.2\varphi_s(i,j) + 0.1\varphi_s(i \pm 1, j \pm 1) \tag{4.61}$$

4.5.5 Failure Criteria

In equation (4.55) $\gamma = q_0/D_0$ is the ratio of the characteristic specific discharge q_0 to characteristic hydraulic conductivity D_0, is used to normalize pressure gradient. In this equation the form of *e* follows from a consideration which a hydrostatic pressure *p* cannot lead to erosion, but a gradient can.

The critical stress σ should be a function of the solid fraction φ_s. However, the non-local nature of elastic stress distribution in the porous medium justify σ be more appropriately cast in term of $\bar{\varphi}_s = V^{-1}\int_V \varphi_s dv$, a regional average of φ_s over a region associated with a few grain volumes.

In order to describe the dependency of failure stress σ on volume fraction, the functional form as equation (4.60) is used that represent the sharp dependence of σ on volume fraction.

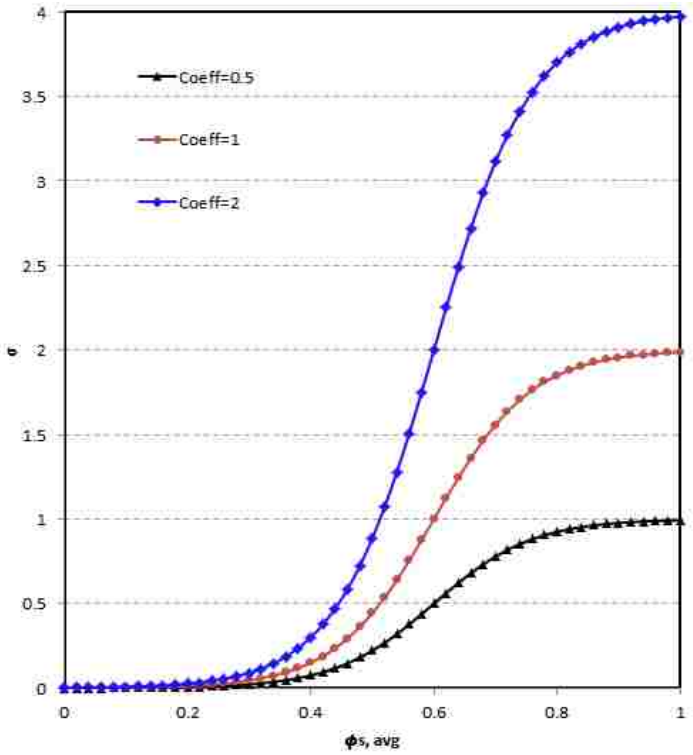

Figure 4.7. Failure Stress Criteria

A simple model for deposition, the rate at which the mobile granular grains transformed back to immobile solid phase is given by

$$d = k_d \ (\varphi_s - \varphi_s^*)\varphi_g \geq 0 \tag{4.62}$$

4.5.6 Formulation to Update Individual phases

Volume conservation for individual phases will be updated by equation (4.5) - (4.7).

Immobile volume fraction

$$\partial_t \varphi_s = -e + d \tag{4.63}$$

$$\varphi_s^{t+1} = (-e + d)dt + \varphi_s^t \tag{4.64}$$

Mobile volume fraction

$$\partial_t \varphi_g = e - d - \nabla.(\varphi_g\, u_g) \tag{4.65}$$

Let say S = e - d

$$\frac{\partial \varphi_g}{\partial t} = S - \nabla.(\varphi_g\, u_g) \tag{4.66}$$

The LHS of the above equation represents the rate of change term for mobile volume fraction. The finite volume integration of above equation over a control volume (CV) must be added with a further integration over a finite time step Δt. Using Stokes's theorem the volume integral of flux term can be replaced with surface integral and changing the order of integration in the rate of change term we obtain

$$\int_{CV}\left(\int_t^{t+\Delta t}\frac{\partial \varphi_g}{\partial t}dt\right)dV = \int_t^{t+\Delta t}\int_{CV} S dV dt - \int_t^{t+\Delta t}\left(\int_A n.\left(\varphi_g u_g\right)dA\right)\mathrm{dt} \tag{4.67}$$

In this equation, A is the face area of the control volume, ΔV is its volume, which is equal to $A\Delta x$, where $\Delta x = \delta x_{EW}$.

If the mobile volume fraction at the node is assumed to dominate over control volume, the left hand side of the above equation can be written as

$$\int_{CV}\left(\int_t^{t+\Delta t}\frac{\partial \varphi_g}{\partial t}dt\right)dV = \left(\varphi_g^{t+1} - \varphi_g^{t}\right)\Delta V \tag{4.68}$$

The first term in right hand side can be written as

$$\int_{t}^{t+\Delta t} \int_{CV} S dV dt = S\,\Delta V \tag{4.69}$$

The second term in right hand side can be written as

$$\int_{t}^{t+\Delta t} \left(\int_{A} n.\left(\varphi_g u_g\right) dA \right) \mathrm{dt} = \left(\left(\varphi_g u_g A\right)_e - \left(\varphi_g u_g A\right)_w + \left(\varphi_g u_g A\right)_n - \left(\varphi_g u_g A\right)_s \right) dt \tag{4.70}$$

Liquid volume fraction

$$\partial_t \varphi_l = -\partial_t(\varphi_s + \varphi_g) = -\nabla.(\varphi_l\, u_l) \tag{4.71}$$

This can be written as

$$\frac{\partial \varphi_l}{\partial t} = -\frac{\partial(\varphi_s + \varphi_g)}{\partial t} = -\nabla.(\varphi_l\, u_l) \tag{4.72}$$

The first term of equal sign is equal to

$$\frac{\phi_l^{t+1} - \phi_l^t}{\Delta t} = -\frac{\phi_s^{t+1} - \phi_s^t}{\Delta t} - \frac{\phi_g^{t+1} - \phi_g^t}{\Delta t} \tag{4.73}$$

$$\phi_l^{t+1} = (\phi_l^t + \phi_s^t + \phi_g^t) - (\phi_s^{t+1} + \phi_g^{t+1}) \tag{4.74}$$

Where $\phi_l^t + \phi_s^t + \phi_g^t = 1.0$

Therefore $\phi_l^{t+1} = 1 - (\phi_s^{t+1} + \phi_g^{t+1})$ (4.75)

Or using the second term in right hand side to update liquid volume fraction, we can by integrating both side we will have

$$\frac{\partial \varphi_l}{\partial t} = -\nabla.(\varphi_l\, u_l) \tag{4.76}$$

$$\int_{CV}\left(\int_t^{t+\Delta t}\frac{\partial \varphi_l}{\partial t}dt\right)dV = -\int_t^{t+\Delta t}\left(\int_A n.(\varphi_l u_l)\,dA\right)\mathrm{dt}$$

In this equation, A is the face area of the control volume, ΔV is its volume, which is equal to $A\Delta x$, where $\Delta x = \delta x_{EW}$.

If the liquid volume fraction at the node is assumed to dominate over control volume, the left hand side of the above equation can be written as

$$\int_{CV}\left(\int_t^{t+\Delta t}\frac{\partial \varphi_l}{\partial t}dt\right)dV = \left(\varphi_l^{t+1} - \varphi_l^{t}\right)\Delta V \tag{4.77}$$

The second term in right hand side can be written as

$$\int_t^{t+\Delta t}\left(\int_A n.(\varphi_l u_l)\,dA\right)\mathrm{dt} = ((\varphi_l u_l A)_e - (\varphi_l u_l A)_w + (\varphi_l u_l A)_n - (\varphi_l u_l A)_s)dt \tag{4.78}$$

By equalizing the above two equation we will get

$$\left(\varphi_l^{t+1} - \varphi_l^{t}\right)\Delta V = ((\varphi_l u_l A)_e - (\varphi_l u_l A)_w + (\varphi_l u_l A)_n (\varphi_l u_l A)_s)dt \tag{4.79}$$

Chapter 4: 2-Dimensional Channelization Model

The results of the model developed in the previous chapter for simulating formation and propagation of high porosity channels in unconsolidated formations are presented and discussed in this chapter. This methodology describes channelization as evolution of formation porosity driven by fluid flow as a function of space and time. The results show that the initially fairly uniform porous medium becomes increasingly heterogeneous as flow rate increases beyond a threshold, as flow-induced erosion generates bands of enhanced porosity that merge together to form channels with high hydraulic conductivity. Eventually toward the end of the transient state, just few channels preferentially conduct most of the injected fluid. In the reached steady-state conditions, the geometry of channels will not change as long as injection rate is constant.

In this chapter, we investigate how the results of channelization model may depend on different parameters such as flow rate, formation heterogeneity, initial average porosity, and stress distribution, and how these changes agree with the trends observed in the field. Depending on formation properties, any of the mentioned factors could be crucial in determining the rate for the onset of channel formation or injectivity loss.

For the finite volume model, we consider the characteristic domain size to be equal to 1m, and specific discharge in the order of 1cm/s, hence time-scale $T = L/q_0$to make the model dimensionless i.e. erosion and deposition rates will be equal to one. The dimensionless parameters in the problem include the thresholds for erosion (σ) and deposition (φ_s^*), respectively in equations (3.9) and (3.12).

5.1 Model Validation

The base case for one-dimensional flow with constant specific discharge and with small heterogeneity in initial porosity is considered for sensitivity analysis of various parameters considered in this model.

Table 1 provides an overview of the parameters used for the base case in these models.

Table 1. Parameter used for the base case in 2-dimensions

Parameter	Value
Dimensions	$L_x = L_y = 0.32m$
Number of cells in x, y direction	100
Time-step	1e-2
Simulation time	6s
Domain size	1m
Initial porosity, φ_l	20%
Conductivity	$4.67 * 10^{-8} m^2$
Injection rate	0.01m/s
Pore size	0.001m(1000μ)
Viscosity of fluid	$10^{-3}\, kg/m.s$
Dimensionless constant (A)	180
Characteristic hydraulic conductivity	$10^{-6}\, m^3.s/kg$
Distribution noise	10%

The discretized equations derived from governing equations in Chapter 3 (i.e. Equation 3.5 – 3.15) are solved for a two-dimensional structured grid shown in Figure 3.2. In this model, Neumann boundary condition (NBC), is used at the inlet, and at the outlet Dirichlet boundary condition (DBC), constant pressure, is enforced. NBC is set as a specific constant flow rate at the ghost nodes shown in Figure 3.5. The ghost nodes in Figure 3.5 are shown on four boundaries with red dots (⊙). For DBC, we utilized fixed pressure condition in the ghost nodes at outlet to maintain pressure continuity. The ghost nodes approach

(Leveque, 2004) is introduced to avoid discontinuous derivatives across the boundary and allow the real nodes on the boundary to access the extended boundary or so-called ghost cells.

The initial configuration is assumed to have no volume fraction of mobile grains throughout the domain (i.e.$\varphi_g = 0$) because no flow is injected into the domain. The volume fraction of large grains (immovable grains) is 0.8 and for small moveable grains is 0. Therefore, maximum possible fluid porosity will be 0.2. We scale the porosity by the maximum attainable porosity. The scaled porosity is denoted by φ_l and its mean porosity, which may vary from 0 to 1. Hence, φ_l equal to one means complete erosion of the fine grains not the whole medium. Average scaled initial porosity,φ_l, 0.20 (liquid volume fraction) is considered for the model which is perturbed with 10% standard deviation generated by utilizing additive white Gaussian noise (AWGN) to obtain initial porosity distribution in the domain (Figure 5.1).

Gaussian noise is statistical noise that has its probability density function equal to that of the normal distribution, which is also known as the Gaussian distribution. In other words, the values that the noise can take on are Gaussian-distributed. A special case is white Gaussian noise, in which the values at any pair of times are identically distributed and statistically independent (Truax, 1999).

Porosity variation could be described as the weak heterogeneity in the strength of rock (σ). Erosion occurs when the fluid shear stress acting on a given sand particle becomes greater than the cohesion force holding the grains together. Fluid induced stress is a function of pressure gradient which could be initiated by higher flow rate (Darcy law) or porosity gradient ($P \sim \nabla\phi$). Hence channelization may not occur in uniform homogeneous formation till reaching a very high interstitial flow velocity. Small perturbations of porosity field may induce stresses exceed inter-granular forces locally, but these forces are localized and are not large enough to cause fluidization of the whole medium.

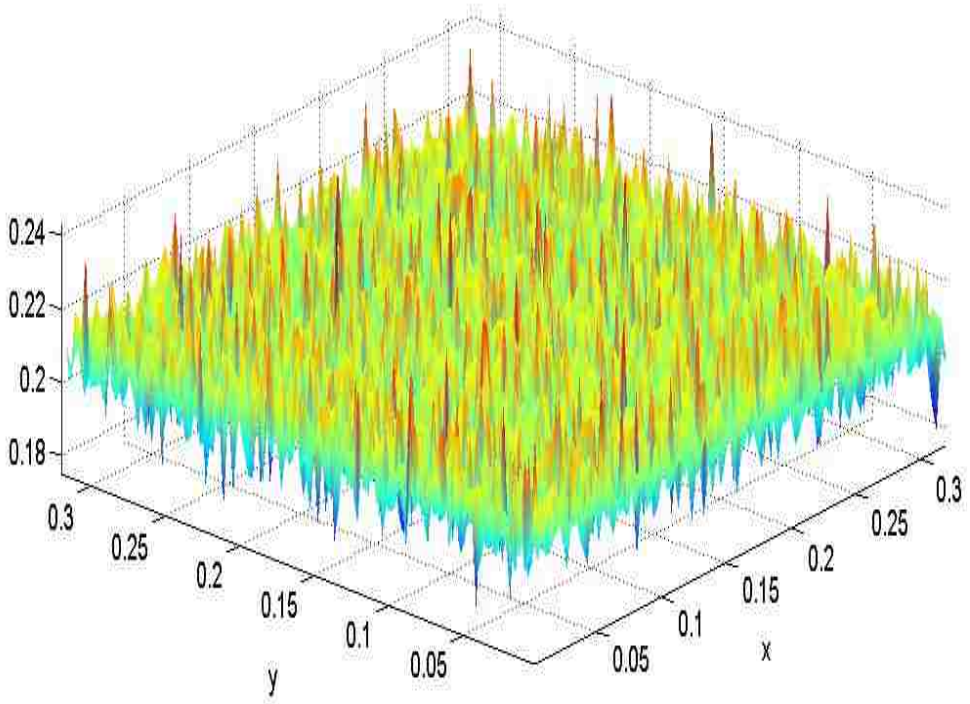

Figure 5.1. Heterogeneity in the initial porosity distribution for base case simulation is shown. There is 10% variation in the initial porosity in entire domain which is resulted from White Gaussian random method.

Numerical solution of equations (3.6) to (3.15) for constant flow rate, $q_0 = 0.01\, m/s$ at the lower boundary (i.e.$y = 0$), and constant pressure at the upper boundary is presented here. The initial and final distribution of pressure field and velocity profile in the domain is shown in Figure 5.2 and Figure 5.3, respectively. It is notable that the porous medium which was initially fairly uniform becomes increasingly heterogeneous as erosion generates regions of enhanced porosity that connect to form channels with high conductivity and lower pressure gradient.

In Figure 5.3. B., the heterogeneity distribution in velocity profile at different time-step is compared. As shown in Figure 5.3. B., the velocity at some regions continually increasing where at the other regions is decreased, meaning that at the regions where velocity increasing, erosion is happening, where the regions that velocity is decreasing, deposition of mobile particles occurred.

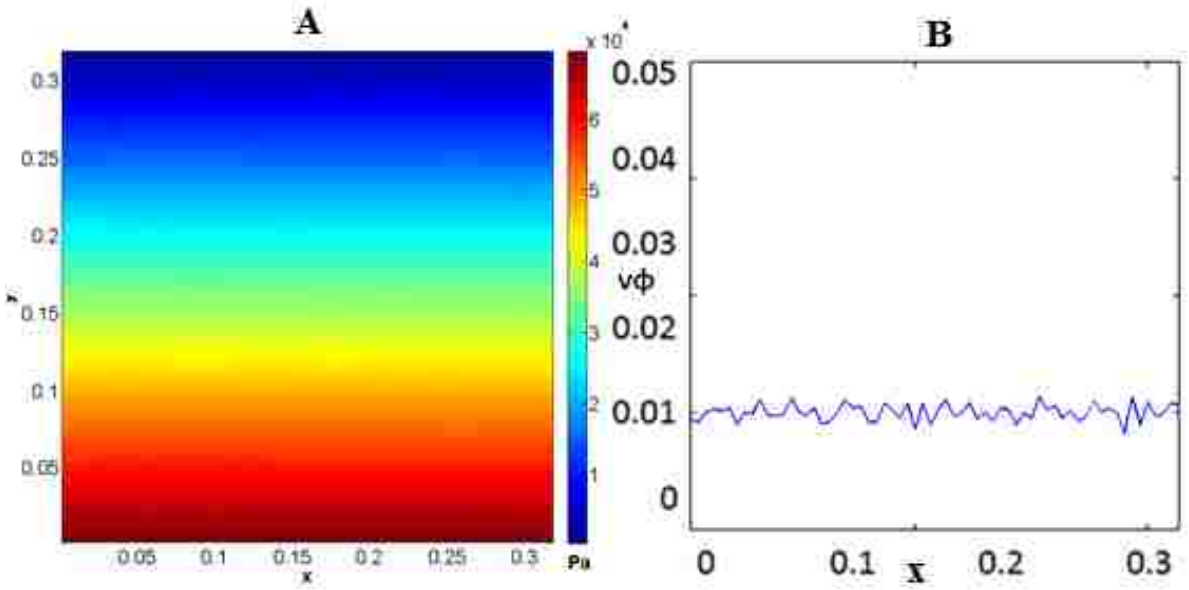

Figure 5.2. A. Initial pressure distribution in the domain shows smooth changes of pressure from inlet to outlet. B. Initial homogenous velocity distribution in the domain.

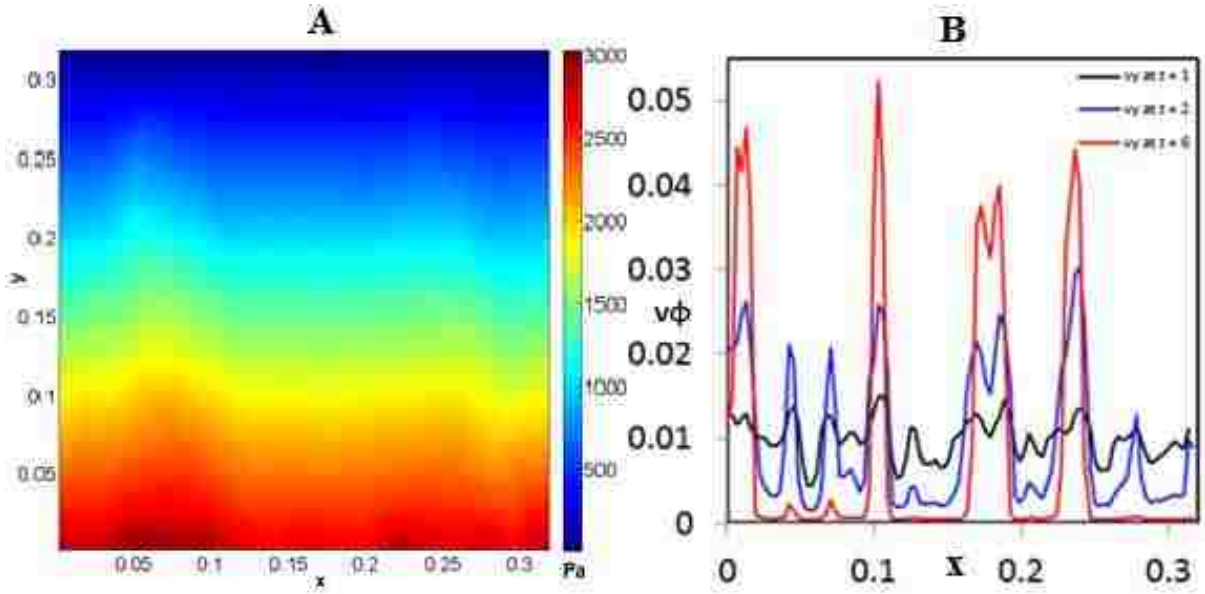

Figure 5.3. A. Final pressure distribution in the domain lacks the uniformity observed in the initial model. This heterogeneity arose from formation of channels, which fractionates the formation into more favorable and less favorable zones for fluid flow. B. Heterogeneity distribution in velocity profile at different time step.

In this test, the pressure is estimated by iteratively solving the Poisson's equation, $\nabla.(D\,\nabla P) = 0$, which is obtained by substituting equation (3.15) into equation (3.9) to calculate the erosion rate, e, and the deposition rate, d, from equations (3.10) and (3.13) respectively. Finally, equations (3.6) to (3.8) are used to update the volume fractions $\varphi_l, \varphi_g, \varphi_s$ from one time step to the next with the scaled time step $\Delta t = 10^{-2}$s.

Validation of the basic case is implemented by comparing the results obtained from experimental and simulation for fluid flow-induced channelization in porous medium published by Mahadevan et al. (2012). They conducted lab experiments by injecting water through a saturated, granular, porous medium, which is a Hele-Shaw cell packed with bi-disperse grains. The smaller grains were 8 times smaller than the larger beads in the cell. When the local fluid flow-induced stress exceeds a critical threshold, the smaller grains are dislodged and transported, thus changing the porosity of the medium and thence the local hydraulic conductivity and the development of erosional channels. They conducted experiments and then ran simulations for different flow rates and different distribution of initial porosity to validate their simulation approach. Hence, we are using the same simulation approach, we use their validation to present a validation for simulations performed here.

In Figure 5.4, A. and B and Figure 5.5, pressure gradient versus failure stress at dimensionless time t = 1s and t = 6s is compared with Mahadevan et al. (2012). As shown, comparison of the calculated pressure gradient and failure stress in our model follows the same trend of experiment done by Mahadevan and the numbers are in a reasonable agreement with the experimental study. The small difference in results provided here and Mahadevan et al. (2012) is mainly derived by Gaussian random model since the random field that is generated in this model is different from their model.

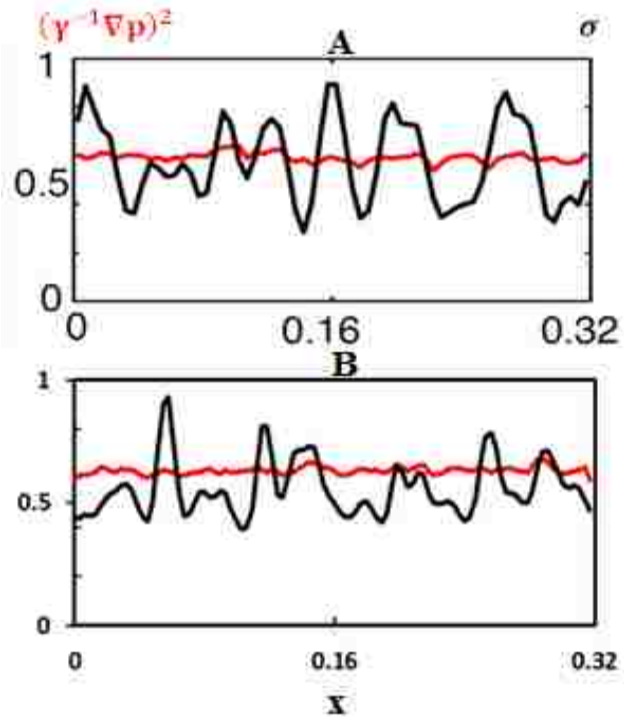

Figure 5.4. Comparison of pressure gradient and failure stress at t = 1s, obtained by (A) Mahadevan et al. (2012) (B) Results of model developed here.

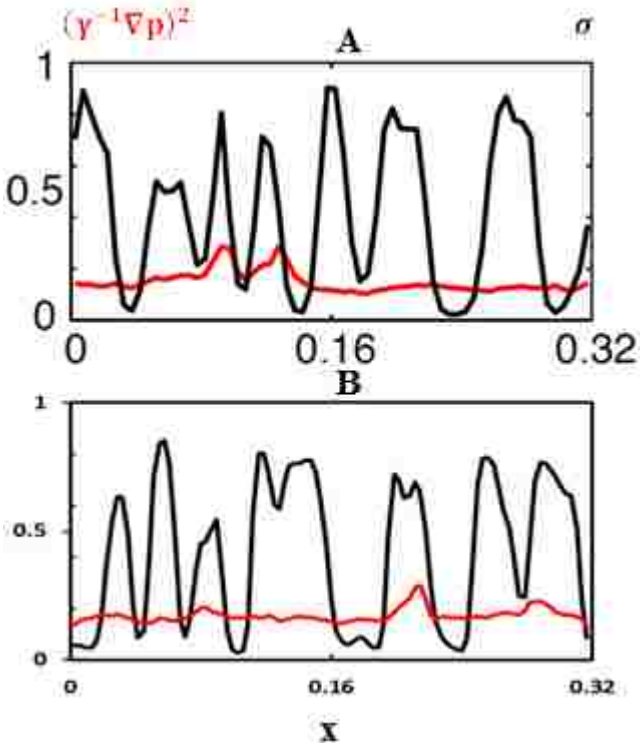

Figure 5.5. Comparison of pressure gradient and failure stress at t = 6s, obtained by (A) Mahadevan et al. (2012) (B) Results of model developed here.

To further investigate results validity, the velocity profile in the medium at different time step is compared in Figure 5.6. A. B. We see that there is good correlation between the results from the generated model (Figure 5.6. A) and the results from Mahadevan (Figure 5.6. B).

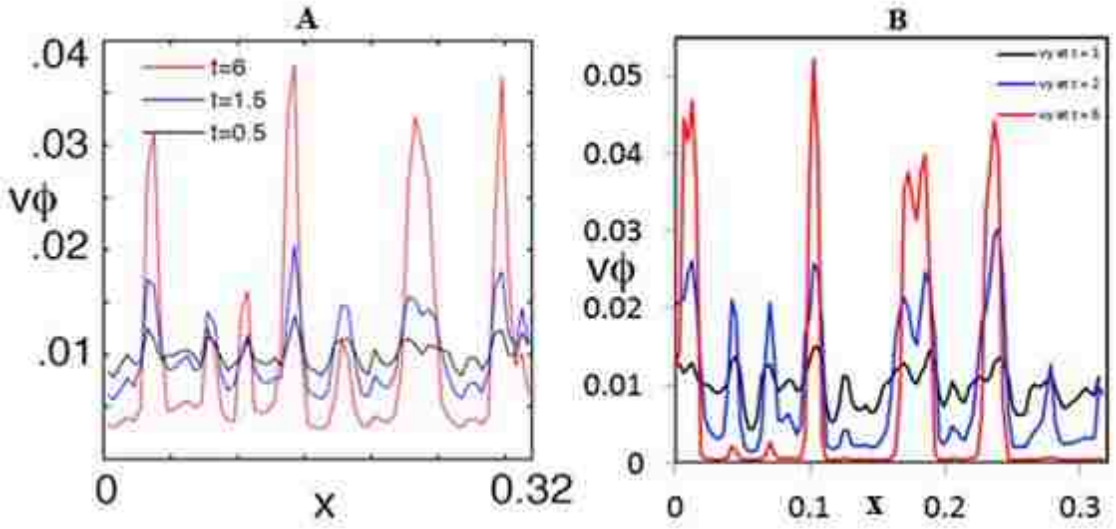

Figure 5.6. Comparison of velocity profile in y direction at t = 1,2 and 6, obtained by (A) Mahadevan et al. (2012) (B) Results of model developed here

5.2 Model Verification

The technique used in choosing appropriate model size here was to start with coarse mesh and gradually refine until the changes observed in the results becomes negligibly small in comparison to the results obtained with larger mesh. Refining a mesh by a factor of 2 can lead to a 4 fold increase in the size of problem, so even more time is needed to run the simulation. Therefore, an optimum mesh size should be selected to avoid increasing time of simulation.

In this section, we compared the results for three different runs of the model on different gird sizes. The three runs were, coarse mesh, with cell sizes of 0.01m giving a mesh size of 32x32 or 1024 cells, medium mesh, with a cell size of 0.005m giving a mesh size of 64x64 or 4096 cells, fine mesh, with a cell

size of 0.0032m giving a mesh size of 100x100 or 10000 cells. Figure 5.7 shows channelization at t = 1.5 for different grid size and verifies that the solution is converging to similar channel pattern generation.

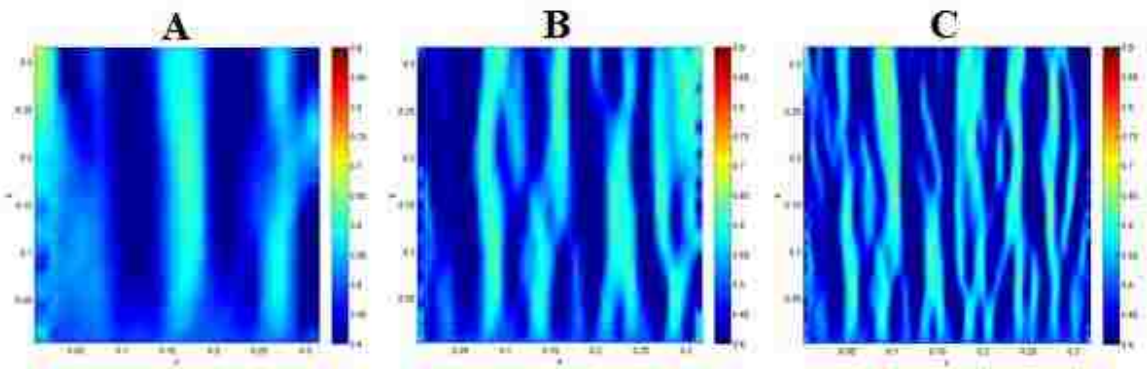

Figure 5.7. Channelization at t = 1.5s for different grid size. (A) Coarse grid, 32x32 (B) medium grid, 64x64 (C) fine grid, 100x100

Figure 5.8 shows the comparison between pressure profiles for five different grid sizes. As shown, the pressure profile after 4096 cells becomes grid independent. Therefore for accuracy and cost efficient of the model, 100000 grid cells are chosen for the rest of simulations. In Figure 5.9, we see the comparison of velocity profile in y-direction for five different runs. The computed results show that there is no change in local velocity profile when the cells number exceed of 4096 cells.

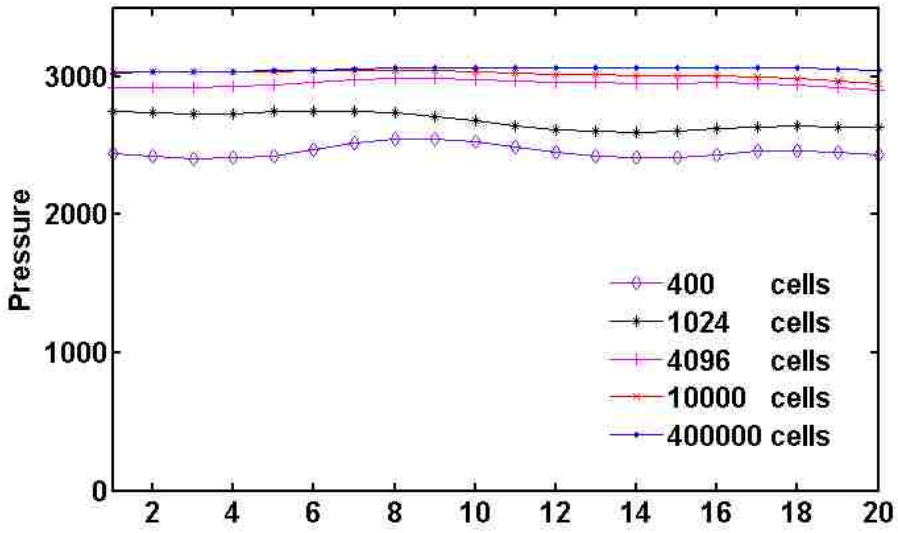

Figure 5.8. Pressure counter for five different grid sizes

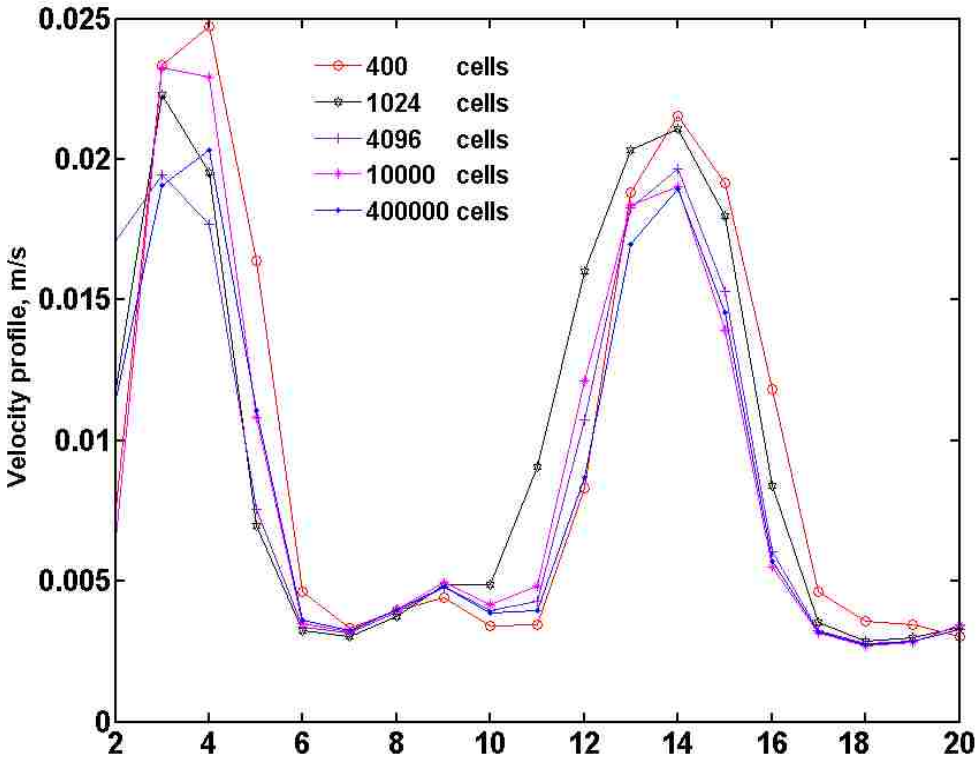

Figure 5.9. Comparison of velocity profile for five different grid size

The transient state reaches the steady state condition for a given constant injection rate after a while. This state represents the situation that flow is enhanced through the region of low solid fraction (high hydraulic conductivity), while regions with higher solid fractions, lower hydraulic conductivity, are avoided by the flow. The evolution of the initial system in time and space is shown by multiple snapshots at different time steps in Figure 5.10. As shown, in Figure 5.10A, the system is initially homogenous porous medium, as it evolves spatially; it becomes eroded and channelized, which is shown in Figure 5.10 B through D. Histogram of the porosity for base case with flow rate $q = 0.01q_0$ at $t = 6$ is shown in Figure 5.11; the bimodality in that case is due to channelization since the bimodal histogram shape often reflects the presence of two different processes being mixed which in this case is the formation being channelized or not.

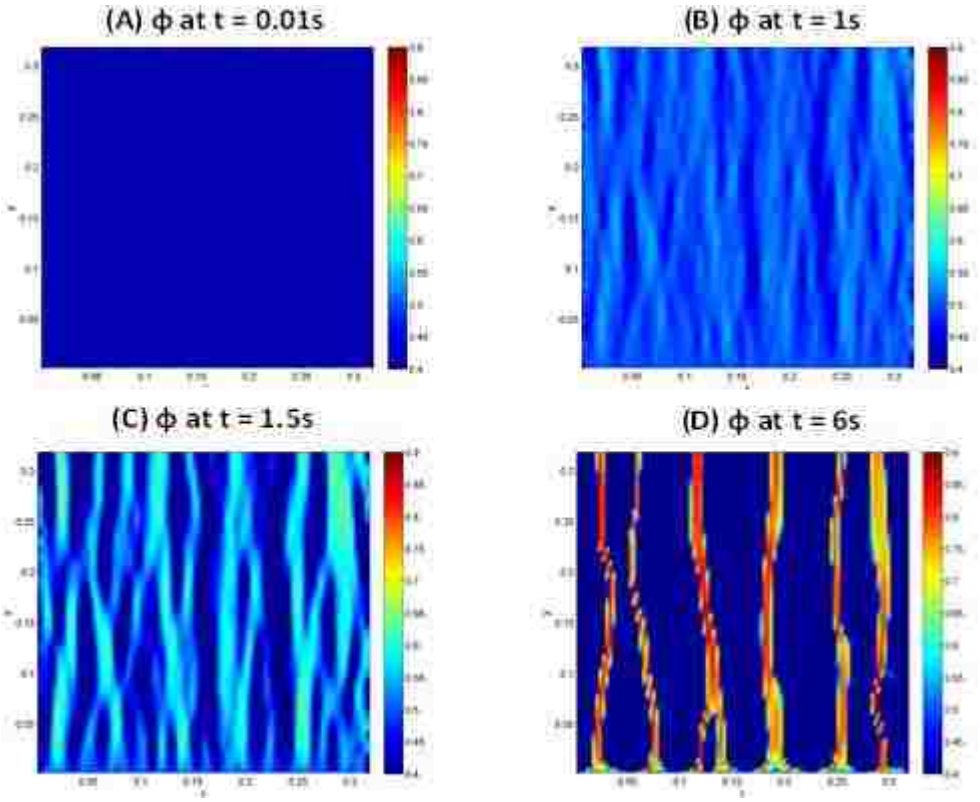

Figure 5.10. Spatial distribution of porosity at different time steps are shown here. The initially fairly uniform medium (Part a) develops small erosional channels (Part b). Small channels are coalescing to form wider channels (Part c). Channel merging terminates upon reaching the steady-state condition (Part d).

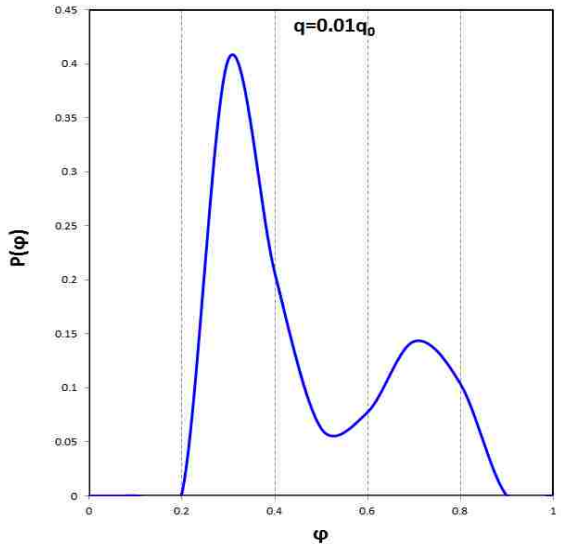

Figure 5.11. Histogram of porosity distribution for q = 0.01 at t = 6 shows bimodality due to channelization.

The existence of a stress threshold above which the grains become cohesion-less and begin to move is due to friction between immobile solid phase and the confining stress, σ, that estimated by using neighbor grains in equation (3.12). The functional form of stress threshold is important in channel initiation and its further development. Grain-size distribution, grains geometry and confining stress are factors in determining this stress threshold; therefore, this stress threshold cannot have the same value everywhere in a heterogeneous porous medium. In equation (3.9), the form of erosion revealed the consideration that a hydrostatic pressure, p, may not lead to erosion, but a pressure gradient can. In order to make the pressure gradient normalize, we use $\gamma = q_0/D_0$, which is the ratio between a characteristic specific discharge ($q_0 = 10^{-2} m/s$) and characteristic hydraulic conductivity ($D_0 = 10^{-6}\, m^3.s/kg$).

In Figure 5.12, we compare the interplay between the heterogeneity in erosion threshold with the squared pressure gradient$(\gamma^{-1}\nabla p)^2$ at t=1s and also when the system reaches to the quasi-steady state at t = 6s. In the areas where$(\gamma^{-1}\nabla p)^2 > \sigma$, sand particles switching from solid to mobile phase and transported by flow, which results in reducing $\bar{\varphi}_s$, lowering the failure stress of rock σ, and consequently developing erosion.

The rate of decrease in pressure gradient with time for different flow rate is compared in Figure 5.13. As it shown, for higher flow rate, the rate of pressure drop is higher.

Figure 5.14 compares flow rate evolution at early time of injection and final stage of injection along a cross-section. In this figure, we see that channelization has led to enhanced or preferential flow paths though regions of higher conductivity at the expense of low reduced flow though other regions even as the total flow rate remains the same. Additionally, there is no strong correlation between the local magnitude of initial flow rate and formation of channels.

As erosion gradually developing, the average porosity and overall hydraulic conductivity over the entire domain increases, as shown in Figure 5.16. The pressure gradient condition requires sustaining the same flow rate drops until flow rate decreases to the level below the erosion threshold till the system reaches the steady state condition.

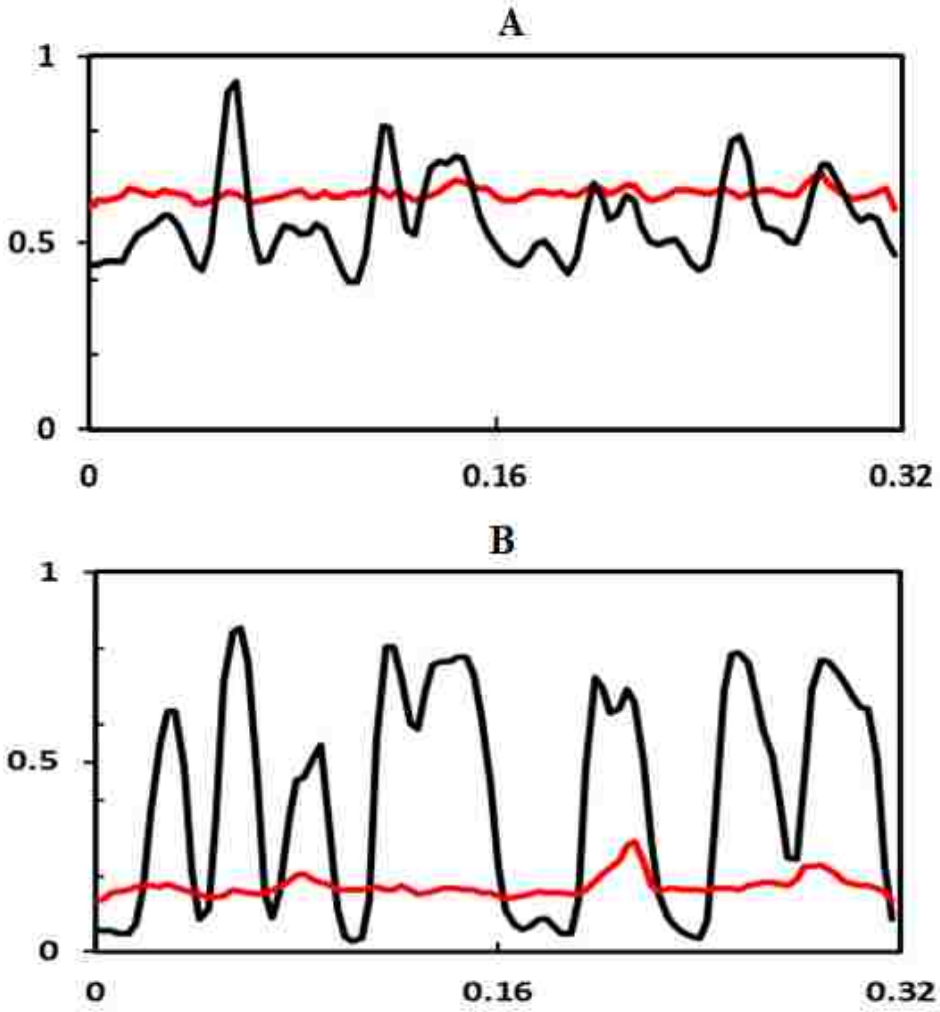

Figure 5.12. Failure stress, σ (black) and squared pressure gradient, $(\gamma^{-1}\nabla p)^2$ (red) along middle cross section of the domain at (A) t = 1s and (B) at t = 6s. At early times, this occurs at several locations. As erosion progresses, the pressure gradient drops, heterogeneity in σ increases, and erosion is limited only to the channels.

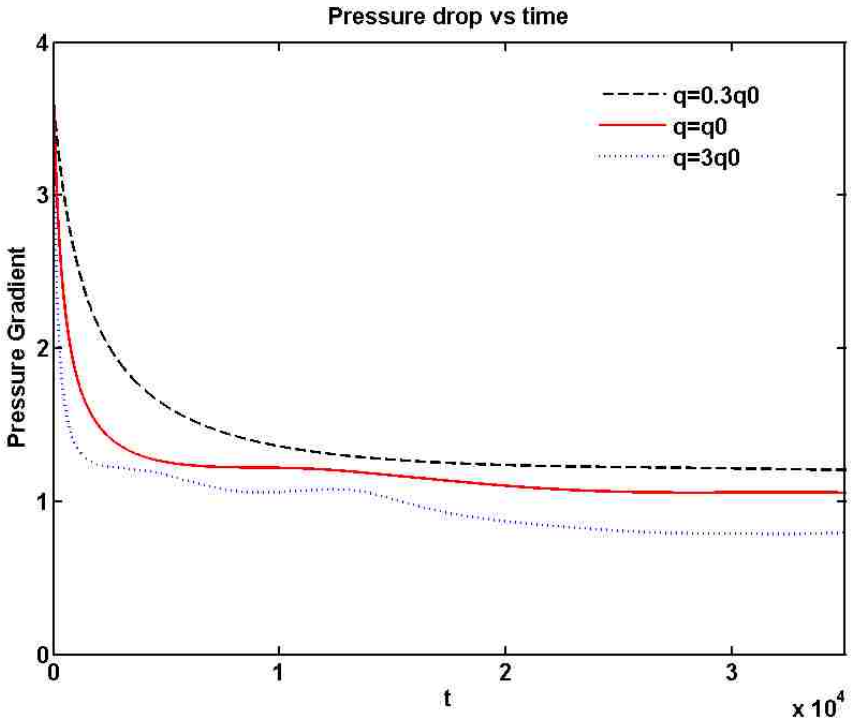

Figure 5.13. Change in pressure gradient for different flow rate of q = 0.3q0, q = q0, and q = 3q0 is compared. For higher flow rate, the rate of pressure drop is higher.

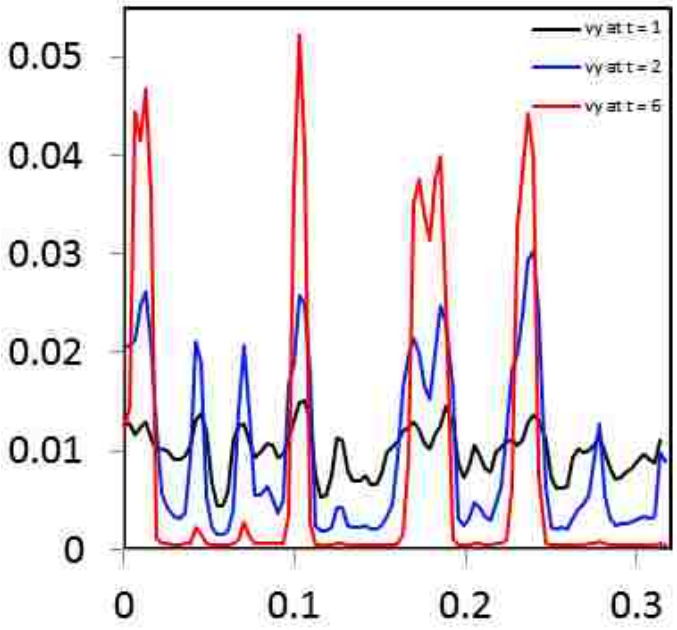

Figure 5.14. Increase in flux in y direction at different time, t = 1,3 and 6 is shown here.

5.3 Parameter Sensitivity Analysis

Experimental studies are limited by lab equipment capacity i.e. the range of pressure and sample size that lab apparatuses may handle and the amount of time that it takes to conduct several tests. Therefore having a good model honor lab measurements, could be used for virtual numerical experiments to model possible situations in the field-scale. Additionally, any field correlation or empirical correlation driven from lab experiments should follow solid theoretical bases to be reliable for practical purposes. Once a model is calibrated with the field data, it could be very useful to run different cases that show the impact of any parameter while other parameters are held constant.

5.3.1 Flow Rate Effect

Different scaled specific discharge at the inlet q/q_0 is considered to understand how geometry of channels in the steady-state condition and injectivity in general may depend on injected flow rate. When flow rate is less than the critical scaled flow rate, $q_{c,}$ which depends on the initial porosity distribution in the medium, no erosion or channelization occurs, as pressure gradient is everywhere smaller than the erosion threshold. However when flow rate becomes equal to critical flow rate, multiple narrow channels are forming as shown in Figure 5.15. B. As injection rate increases further, the number of channels as well as the width of channels increases. In extremely high flow rates, the entire medium begins to erode away and fluidization happens, as shown in part C of Figure 5.15. In all depicted cases, the porosity increases with time after initiation of the flow linearly and then slowly reaching the steady state condition that depends on the inlet specific discharge. The following results obtained by varying the constant parameters such as, flow rate (q_0) and keeping other parameters same as values in Table 1. In Figure 5.16, we see that for different injection rates, the average porosity is increasing with time, until the system reaches steady state that depends on inlet specific discharge. The rate of change in pressure gradient for different injection rate across a cross-section is compared in Figure 5.18. As shown in this figure, we see that for higher injection rate, the pressure drop is higher.

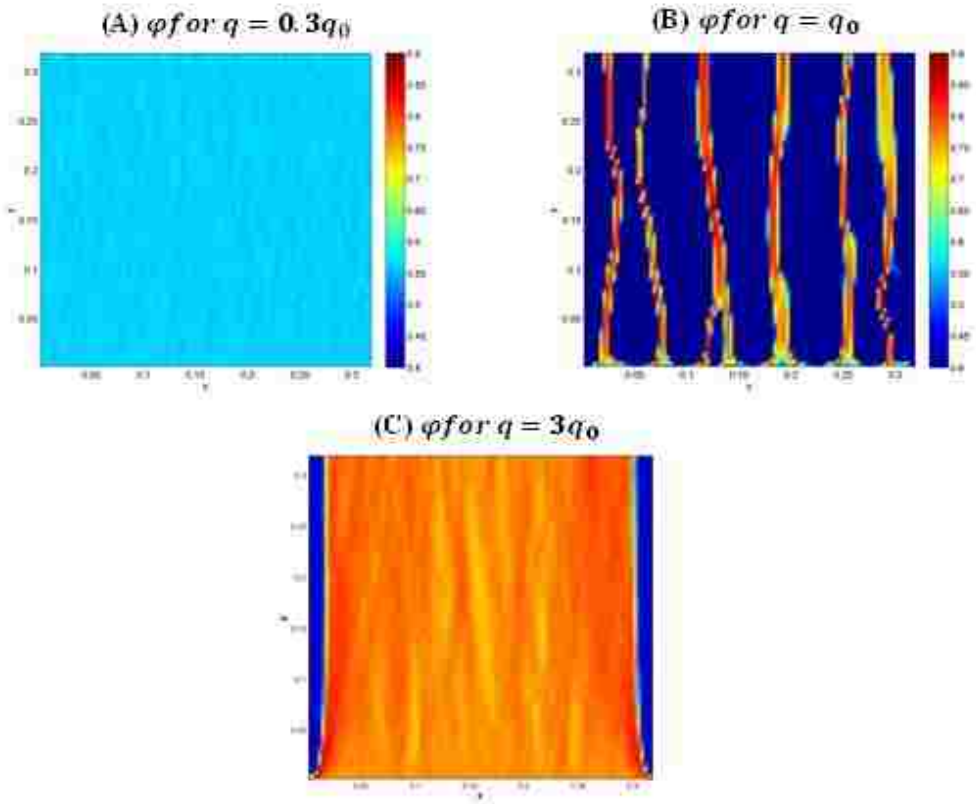

Figure 5.15: Spatial distribution of porosity for different flow rates. A)for $q = 0.3q_0$, erosion occurs but there is no channel initiation. B) for $q = q_0$, conductive channels are formed. , C) for $q = 0.3q_0$, most of the system is washed away and eroded.

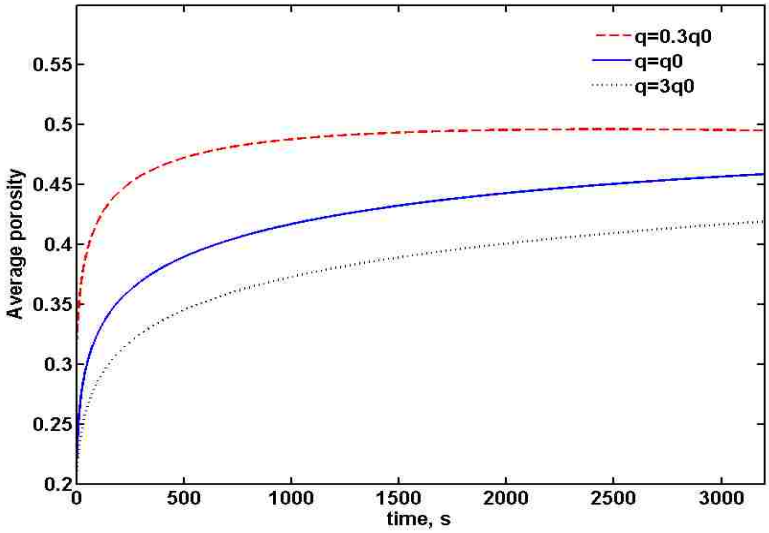

Figure 5.16. Evolution of average porosity ($\varphi_g + \varphi_l$) with time is shown for different fluid flow rate. Higher flow rates leads to higher final porosities. It is notable that in higher flow rates, system reaches steady-state condition faster than slow flow rates.

Histogram of the porosity for varying flow-rates are shown in Figure 5.17; the case q = 0.01 m/s, produce the most bimodal porosity due to channelization. High porosity mode is representing channels while the low porosity mode is depicting formation. These observations can demonstrate the effect of flow rate on channelization.

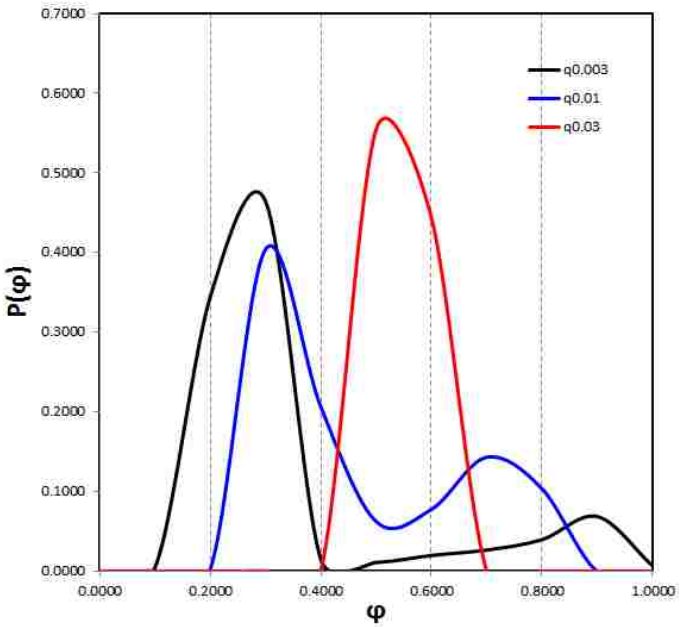

Figure 5.17. Histogram of porosity distribution for q = 0.3, 1. 2 shows bimodality for q = 1 and partially for q = 0.3 due to

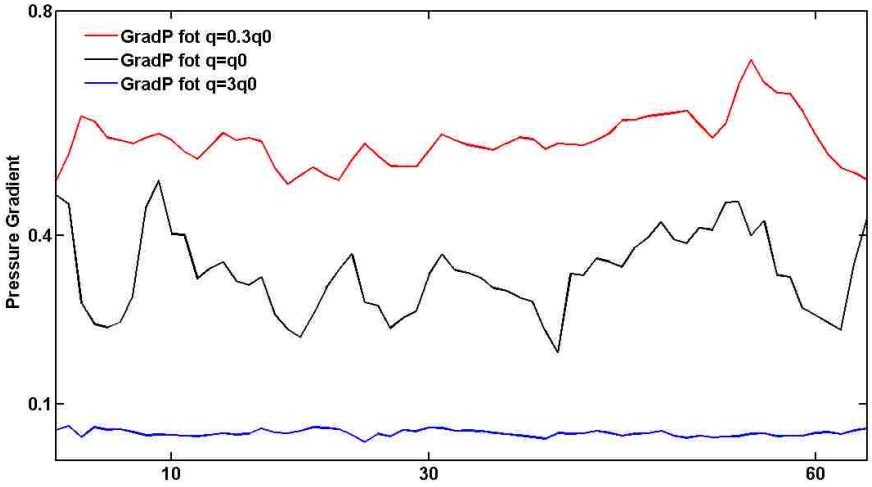

Figure 5.18. Pressure gradient for injection rates q = $0.3q_0$, q = $1q_0$ and q = $3q_0$. For higher injection rate, higher pressure drop is examined.

5.3.2 Effect of Formation Heterogeneity

Change in erosion and deposition rates also lead to variations in the erosion patterns. Increase in erosion rate leads to faster evolution of channels. In Figure 5.19.A, we show the effect of 10-fold increase in erosion rate (π_1=0.1). Increasing k_d to 100 fold so that π_1=100 increases the deposition rate and causes blockage that leads to termination and re-initiation of channels (Figure 5.19.B). In this model deposition remains small even when $k_d = k_e$, because $\varphi_g \ll \varphi_l$ and a significant (100-fold) increase in k_d is needed before we start to see the effect of deposition. The average size of channels does not change in either case relative to when π_1=1.

The spacing and width of channels are independent to the domain size of the model in a sense which doubling the model size does not change the result. The natural length scales in the problem are the system size L, the nominal pore size l_p which evolves with time, but remains a microscopic length, and the length scales q_0/k_e, q_0/k_d control the dynamical evolution of the channels but not their final state. What remains is the threshold for erosion σ; since the onset of channelization is strongly influenced by variations in the porosity (and thus the instability) of the medium, we expect that linear stability analysis of the base state should predict that channels form at locations where σ is smallest initially. Therefore for the same inlet specific discharge, the size and number of channels is a function of σ (x,y,0). In Figure 5.19.A we show that for a given inlet specific discharge, if σ (x,y,0) ≡ f(x) has a single minimum, a single channel forms and grows until the pressure gradient falls below the erosion threshold, while in Figure 5.19.B, wee that if σ (x,y,0) has multiple minima, multiple channels form. For the Gaussian model of disorder that used, if the variance in the threshold for erosion (or equivalently the porosity variations) is also changed, this leads to variations in the patterns as well. Figure 5.20. A,B. it is shown that an increase in standard deviation of the initial white noise leads to greater heterogeneity in the channel number and spacing. Figure 5.20 A shows that heterogeneity in final stage is weak when the initial standard deviation of porosity is small so that the wormholes compete evenly to break through domain with smoother walls.

For higher standard deviation, Figure 5.20 B demonstrates larger heterogeneity. Histogram of porosity for varying standard deviations are shown in Figure 5.21; where the bimodality in both cases seen which is due to channelization.

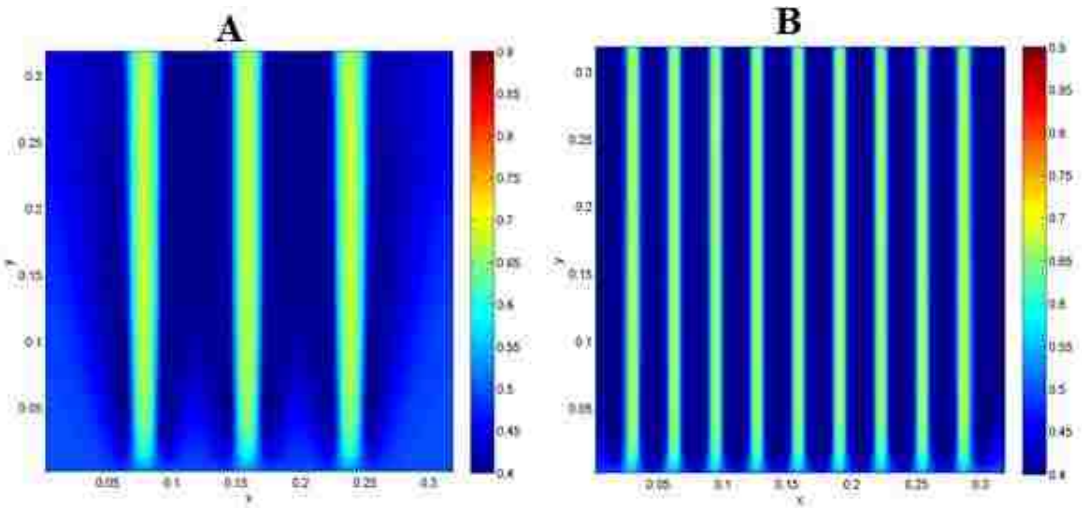

Figure 5.19. Erosion channels develop along the bands with only slightly higher porosity from the matrix for porosity distribution (at t = 3s) with increment of 1% (A) along three line, and (B) along nine lines (at t = 3s), each being one grid cell wide.

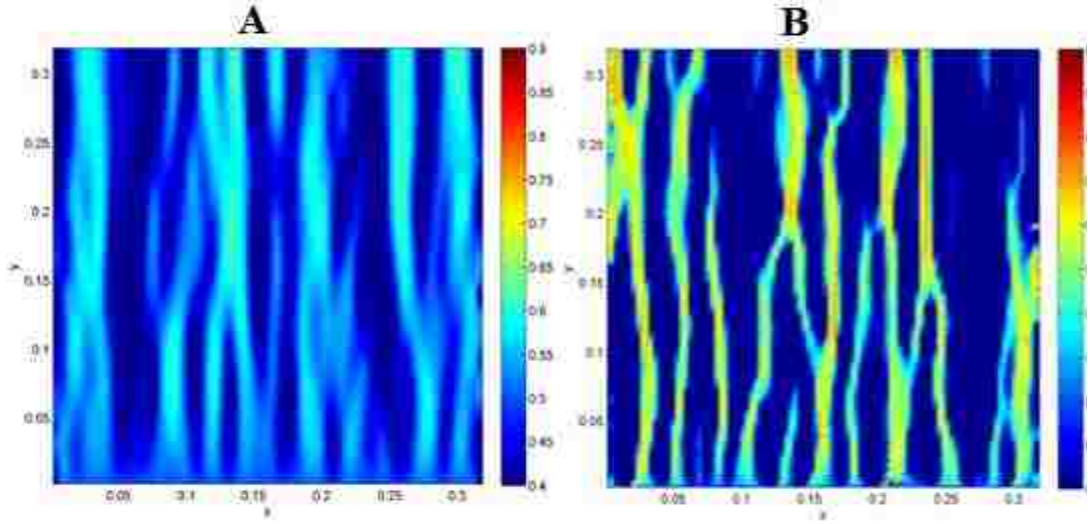

Figure 5.20. The final distribution of porosity at (t = 6) is shown to be sensitive to the initial heterogeneity in σ arising from φ_s. The standard deviation in initial perturbation to φ_s is (A) sd =0.001, (B) sd = 0.03

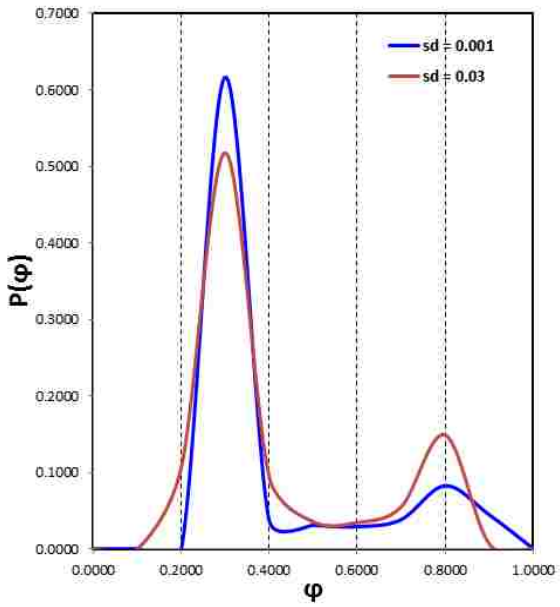

Figure 5.21. Porosity histogram for different standard deviation of distribution, sd = 0.001, sd = 0.03. Bimodality arises from channelization in both cases.

5.3.3 Rock Property Effect

In this section, we explore the effect of rock strength and its strength properties on channelization. The proposed model considers rock strength role in the functional form of strength, σ and its parameters. We consider two different venues: First one is examining different functional form for strength $\sigma = (\overline{\varphi_s})$. In Figure 5.22., we see that different range for σ is obtained by varying the function form of the erosion threshold, but we want the range to be between $0 \leq \sigma \leq 1$ since the dimensionless variables change between 0 and 1. Considering the change in failure stress function, we thus see that the form of the erosion threshold function and its initial, possibly heterogeneous spatial distribution are crucial in determining the growth and form of the channels. In Figure 5.23. A, the porosity evolution at t = 3s is showed for the function of local failure stress $\sigma = 0.5 * (\tanh(2\pi(\overline{\varphi_s} - 0.6)) + 1)$ and in Figure 5.23. B, this function is $\sigma = 2 * (\tanh(2\pi(\overline{\varphi_s} - 0.6)) + 1)$, which gives a range of $0 \leq \sigma \leq 4$ as demonstrated in Chapter 3.

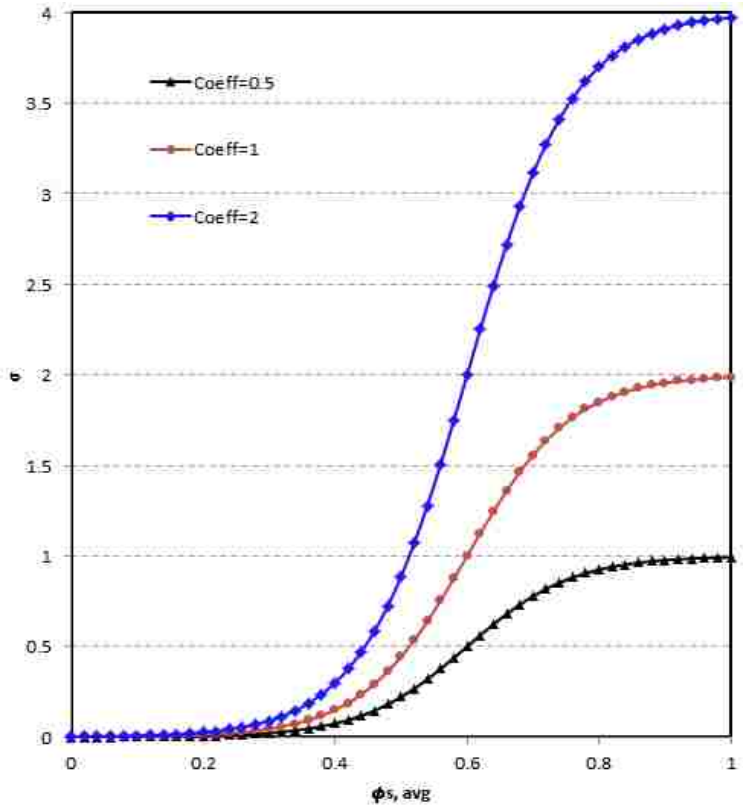

Figure 5.22. Different function form of erosion threshold

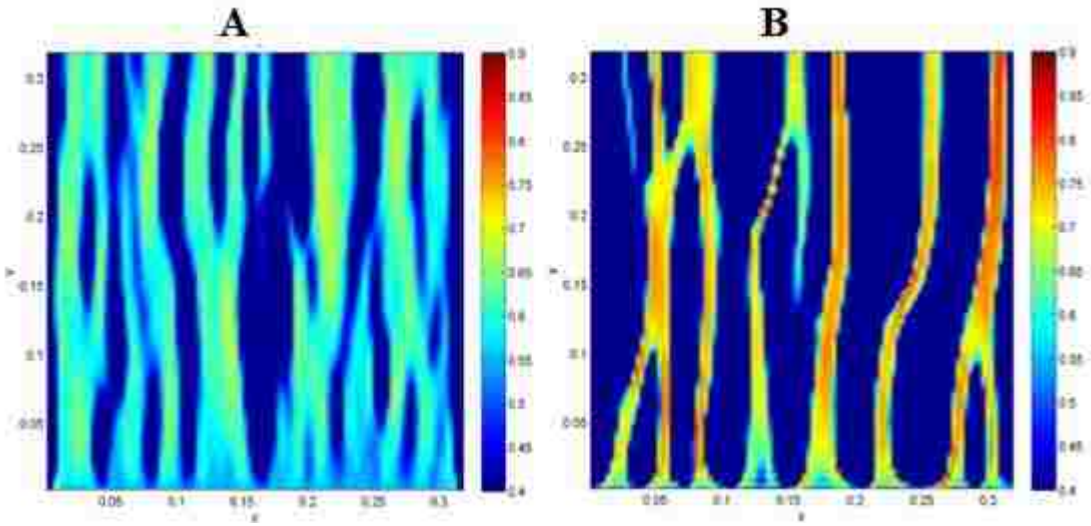

Figure 5.23. The evolution of porosity is sensitive to the functional form of the erosion threshold, σ. Here the $\sigma = coeff * (\tanh(2\pi(\overline{\varphi_s} - 0.6)) + 1)$ is shown for the choices of (A) coeff = 0.5 , (B) coeff = 2.

Second venue is showing how changes of parameters/coefficients in a specific strength functional may change the pattern of channelization. In Figure 5.24, we compare different trends for rock strength that obtained by varying the coefficients in erosion threshold function σ, to $\sigma_1 = \overline{\varphi_s}$ where the rate of change in rock strength is proportional to change in average rock porosity, $\sigma_2 = \overline{\varphi_s}^2$ where there is a parabolic relationship between change in rock strength and average porosity, $\sigma_3 = 0.5 * (\tanh\big(2\pi(\overline{\varphi_s} - 0.6)\big) + 1)$ where with average porosity of 60% the rock strength is approximately 0.5, and $\sigma_4 = 0.5 * (\tanh\big(2\pi(\overline{\varphi_s} - 0.5)\big) + 1)$ where with average porosity of 50% the rock strength is 0.5. The comparison between functional forms of rock strength, σ_3 and σ_4, demonstrate that the second form of equation would fit unconsolidated rock more than the first form since with higher average porosity similar rock strength is obtained as the f form of rock strength equation.

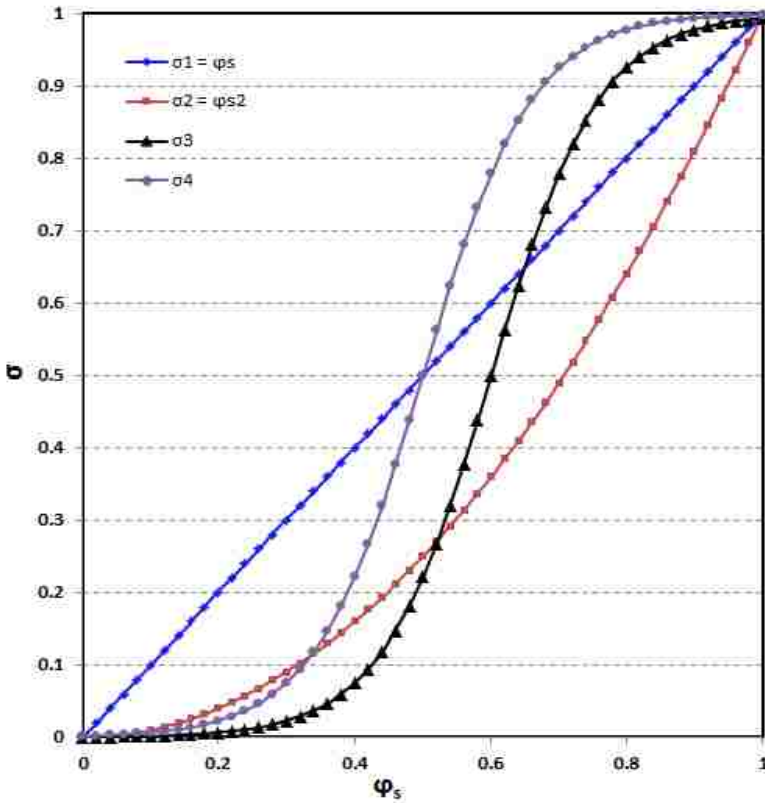

Figure 5.24. Different coefficients in functional form of erosion threshold.

The initial porosity also leads to different porosity distribution at the end of erosion process. Based on the obtained results, high initial porosity results in increasing high porous regions. Figure 5.25 shows the comparison of finial porosity distribution for different initial porosities. As shown in Figure 5.16. A, for smaller initial porosity, the channels will become thinner and number of channels increases as well, but for higher initial porosity the channels become thicker and the number of channels decreased (Figure 5.16. B).

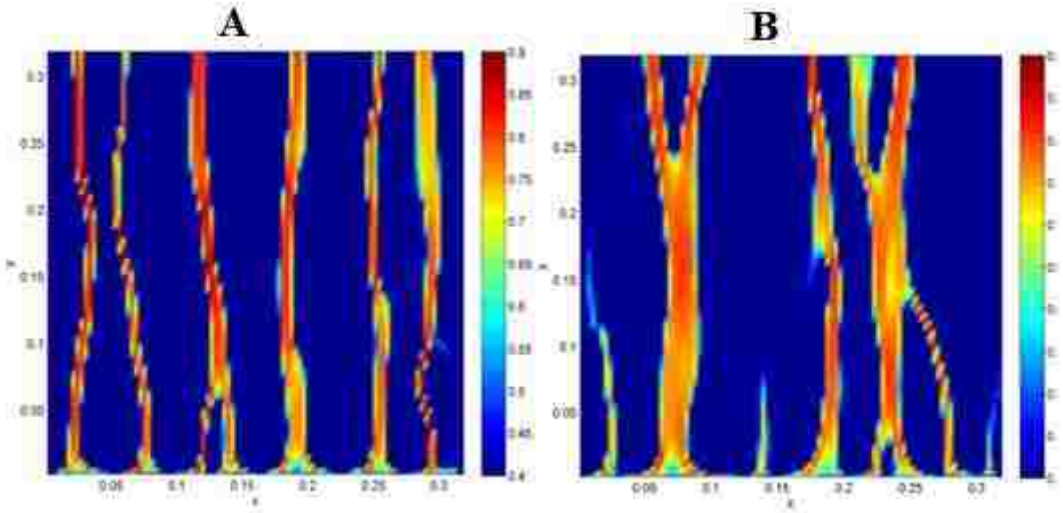

Figure 5.25. Effect of initial porosity on channelization for A) $\varphi_l = 20\%$, the number of channels is higher, but the channels are thinner B) $\varphi_l = 30\%$, the numbers of channel are less and the channels are thicker.

5.3.4 Effect of Fluid Property

Due to the current evolution of environmental regulations and operator company rules, the percentage of produced water that is re-injected in the reservoir or injected in disposal wells is increasing and will continue to do so in the coming years. The type of injected fluid (i.e. produced water versus treated sea water, surface water or aquifer water) may impact how the injector completions are designed, how the injector wells are operated, and how they perform in terms of injectivity and flow conformance. Hence, we need to consider the effect of fluid viscosity μ on formation of channelization patterns. In

Figure 5.26, we see that for higher fluid viscosity, $\mu = 2e-3\ kg/ms$, the pressure gradient is higher than lower viscosity $\mu = 5e-4\ kg/ms$. Therefore higher pressure gradient will results on higher degradation of formation matrix which results in creating bigger channels and in some case complete washout of the system. This phenomenon is justified in Figure 5.27 by comparing the histogram of porosity for different fluid viscosity that used.

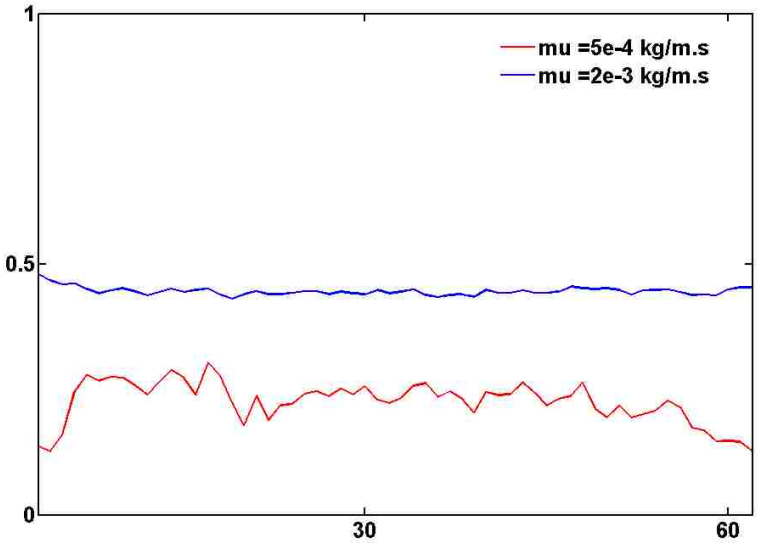

Figure 5.26. Pressure gradient for different fluid viscosity.

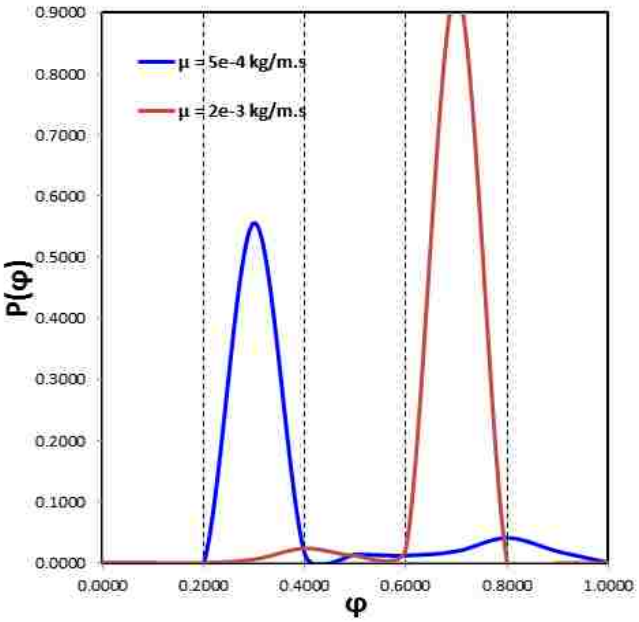

Figure 5.27. Porosity histogram for different fluid viscosity of μ=2e-3 and 5e-4

5.4 Summary

In this chapter, linear flow simulation is developed to model channelization in porous medium. In the presented simulations, a two-dimensional rectangular grid with finite volume method is used. The initiation and propagation of channels is described by interactions between pressure gradient of fluid flow and failure stress of rock. Meaning that where pressure gradient is greater than failure stress the grains are dislodged and transformed from stationary to mobile because of reduction in immobile grains, which result in lowering rock stress. In this model, Additive White Gaussian Noise method used to generate a random porosity field to include the effect of heterogeneity. Model verification and validation is conducted by running the simulation for different model and gird size and validating the obtained results with experimental data.

A series of sensitivity studies are conducted to investigate how the results of channelization model may depend on different parameters such as flow rate, formation heterogeneity, initial average porosity, and stress distribution, and how these changes agree with the trends observed in the field. Depending on formation properties, any of the mentioned factors could be crucial in determining the rate for the onset of channel formation.

Chapter 5: Channelization in Radial Flow and Possible Flow-back

We need to consider radial geometry for fluid flow in injectors to mimic the real geometry of injector wells. Axisymmetric geometry may not be a good representative of the real situation as channelization break down the radial symmetry around the wellbore; hence, two dimensional planar models or fully three dimensional models is required to simulate channelization. Due to the complexity of three-dimensional modeling, we limit our analysis to two-dimensional geometry; however, a complete solution of this problem should consider the third dimension effect, as channelization might lead to geometrically complex flow patterns. From computational point of view rather than attempting to use unstructured grids, we use structured grids which conform to the wellbore boundaries within an acceptable approximation. In Figure 6.1. A, a uniform two-dimensional Cartesian grid is shown. The main advantage of using a Cartesian grid is its inherent simplicity in comparison to unstructured grids for finite volume formulation. The main challenge is laid on specifying fluxes at the edges of the small cut cells in such a way that good accuracy is obtained, while numerical stability is preserved.

In order to obtain a good approximation of radial flow geometry injected from the wellbore, wellbore interior is assumed to have high permeability and very high porosity to minimize pressure drop inside the wellbore profile. Obviously, no channelization is expected inside the wellbore. The wellbore perimeter is the most sensitive part in initiating channelization since fluid flow velocity is maximum at the perforation holes. The distribution of flow needs to be specified at the inlet boundary in different nodes around the wellbore. Figure 6.1 shows the numerical grid and a close-up view of the part of the domain containing the wellbore with diameter of $7\Delta x$, where Δx is the grid size in the wellbore vicinity. In this example, 44 nodes are located inside the wellbore. From those nodes, 12 nodes have been selected to apply injection rate, these nodes are laying on the wellbore perimeter. The remaining 32 nodes are representing wellbore inner space. The inner nodes are chosen to be 10 times more permeable than the formation permeability to minimize pressure gradient inside the wellbore. For outer boundary, we use

fixed pressure boundary at all exterior boundaries. Due to the fact that later flow induced channelization will break down the radial symmetry of the fluid flow, it is more appropriate to apply injection at the inner nodes to give a chance to the flow to redirect itself to more favorable directions. By applying injection rate at the inner nodes, location and direction of induced channels will be independent of location of applying injection nodes. In general if injection is performed through perforation holes, previous approach is a better approximation of the real situation, however, in case of gravel-packs applying injection rates at the inner nodes is more realistic. The pressure gradient for applying injection rate at different nodes is compared in Figure 6.3.

Parameters for the base model are summarized in Table 2. Sensitivity analyses have been conducted for this model in order to understand how different parameter values may affect initiation and propagation of flow channels followed by flow-back model which is coupled to the radial flow model and simulates the change in porosity and permeability of the induced channels because of particle migration toward the wellbore in case of shut-in.

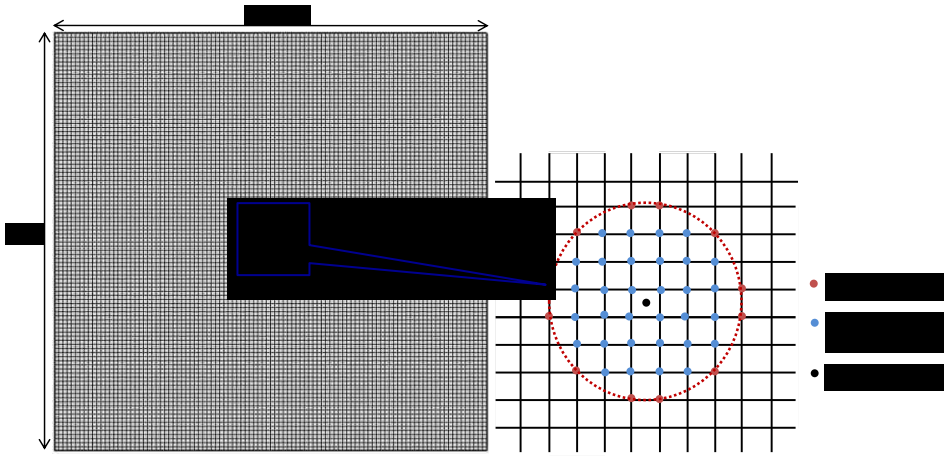

Figure 6.1. (A) Cartesian grid for finite volume calculations. Injection well is located at the center of the grid. (B) Injection nodes in and around the wellbore is shown in a close-up view.

Table 2. Parameters used in radial model

Parameter	Value
Dimensions	$L_x = L_y = 50m$
Number of grids	400×400
Wellbore nodes	32
Injector nodes	12
Wellbore diameter	dx=0.125 m
Reservoir size	$400 \times dx$
Time-step	1e-2
Simulation time	6s
Initial porosity, φ_l	20%
Immobile volume fraction, φ_s	80%
Mobile volume fraction, φ_g	0.0%
Conductivity	$1 * 10^{-8} m^2$
Injection rate	0.01 - 2 m/s ($0.2 - 34\ bbl/min$)
Pore size	0.001m(1000μ)
Viscosity of fluid	$10^{-3}\ kg/m.s$
Characteristic hydraulic conductivity	$10^{-6}\ m^3.s/kg$
Porosity distribution noise	10%

Numerical solution to equations (4.5) through (4.13) is calculated with a specific injection rate $q = q_0 = 0.1m/s$ distributed and enforced at the injection nodes demonstrated in Figure 6.1, which represent perforation holes. Having equal specific discharge for those nodes, the injection rate for the wellbore is equal to nq_0, where n is the number of injection nodes. Figure 6.2. A shows the initial

pressure distribution before injection and Figure 6.2. B shows the final pressure distribution in the domain after injection reaches to the steady-state condition, which describes transition from a fairly uniform and homogenous pressure distribution at the beginning to quite heterogeneous porosity and pressure distribution in later time driven mainly by channels propagated radially from the wellbore. Analogous to the linear flow simulations, porosity distribution at different time steps is sensitive to initial injection rate, and other factors discussed in parallel flow model and will be studied in following sections.

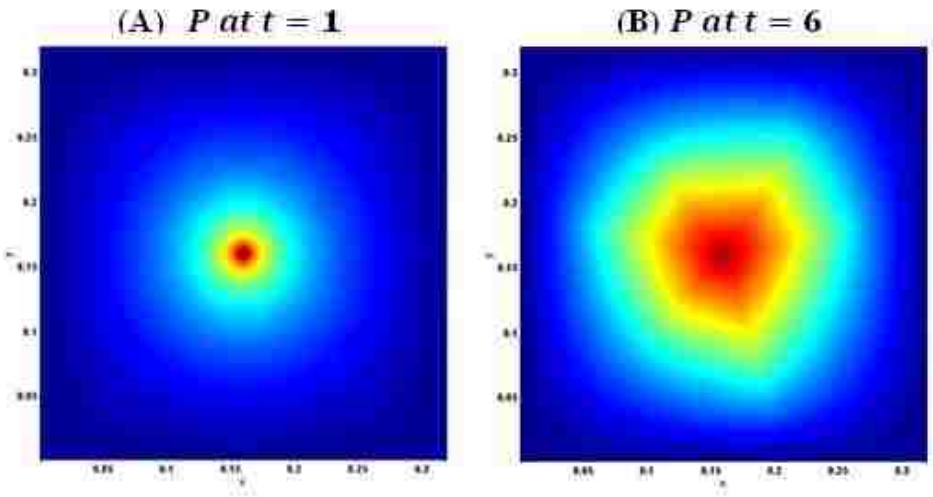

Figure 6.2. (A) Homogenous initial pressure distribution (B) Heterogeneous final pressure distribution

6.1 Model verification

Similar to linear flow model, the common technique used for verification is to start with a coarse mesh and gradually refining the mesh to check the convergence of results with mesh refinement. Refining a mesh by a factor of 2 leads to a 4 fold increase in the size of problem, even more time might be needed to run the simulation. Therefore, an optimum mesh size should be selected to avoid unnecessary increase in simulation time and maintaining reliable numerical accuracy.

Four different discretization's grids of the same problem are tested for one case (q = 0.1m/s), these grids consist of 90000, 160000, 360000, and 1000000 cells with the same size and dimensions. In Figure 6.4, the pressure gradient is compared for these different cell numbers. It is seen that the prediction are almost identical for grid number greater than 90000, and change in pressure gradient follows the same trend for finer mesh than 90000. Thus, to keep the balance between numerical accuracy and computational economy, 160000 grids are employed for the rest of simulations for this problem.

Four models with different sizes are also tested with dimensions as $L_x = L_y$ = 0.32m, 10m, 50m, and 100m but with the same flow rate and boundary conditions to see the effect of the model size on the results. As shown in Figure 6.5, the decline in dimensionless bottom-hole pressure for different model size follows the same trend and there is good agreement for different cases. However, for larger model size, the bottom-hole pressure is higher than smaller model size.

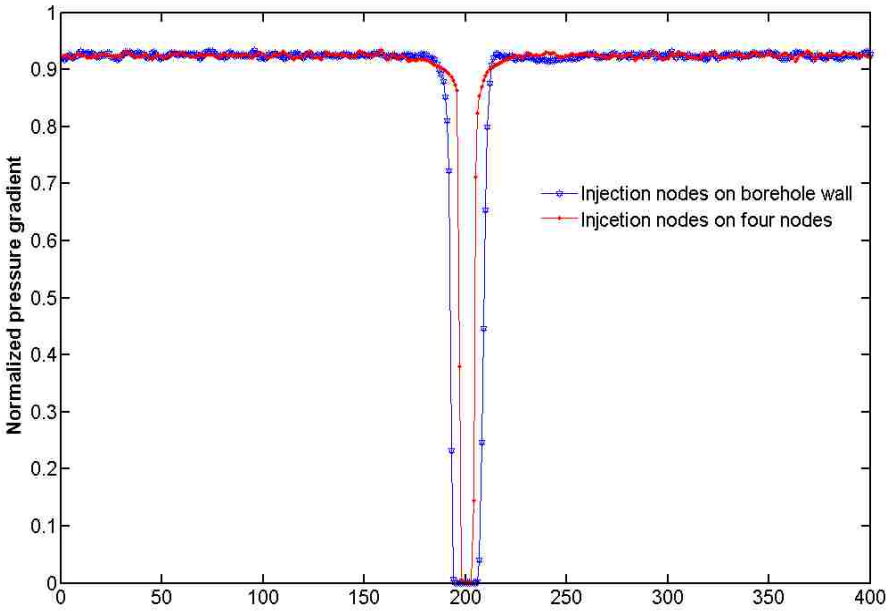

Figure 6.3. Normalized pressure gradient $(\gamma^{-1}\nabla p)^2$ for the model with injection nodes on borehole wall and injection nodes on four inner nodes.

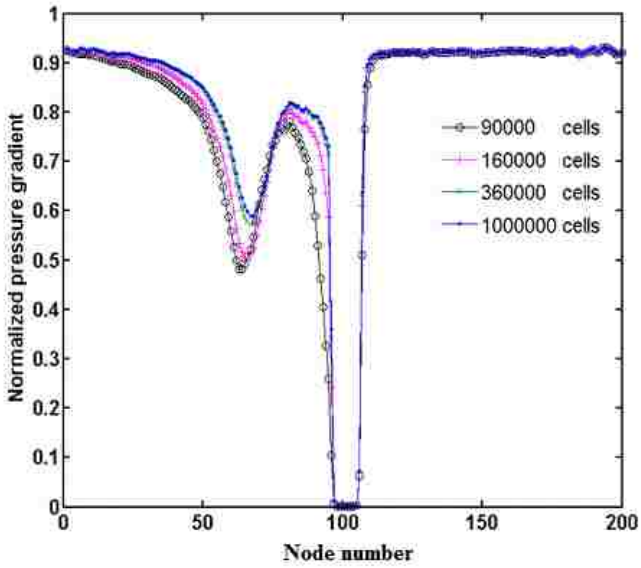

Figure 6.4. Normalized pressure gradient for five different grid sizes. By increasing the mesh size more than 160000, same solution is obtained.

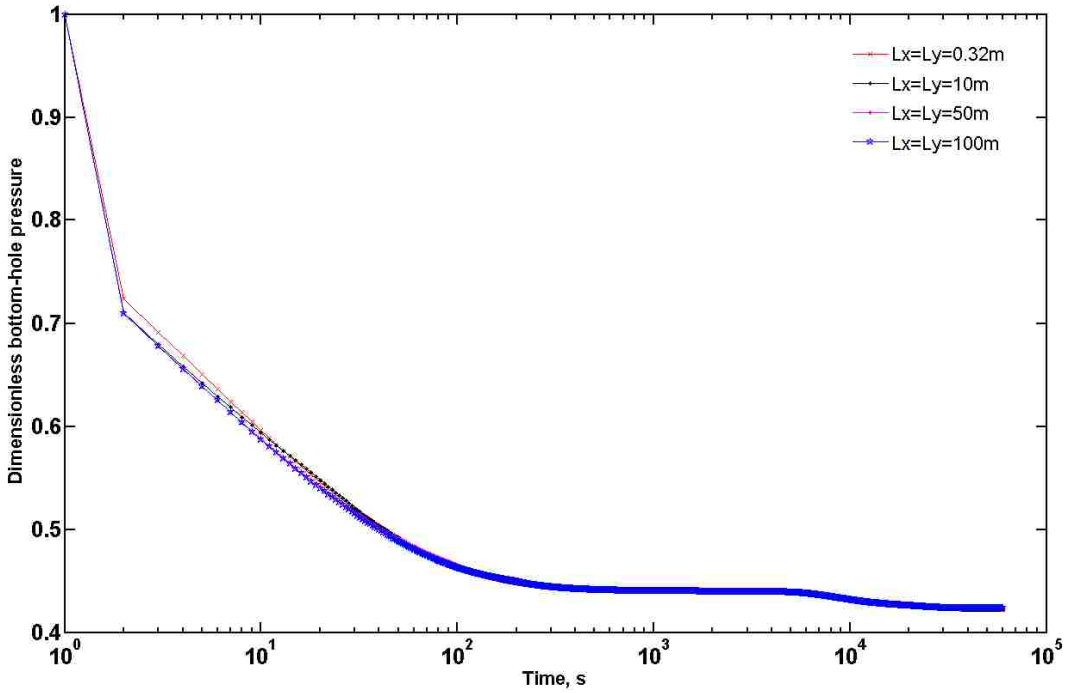

Figure 6.5. Normalized bottom-hole pressure $(\gamma^{-1}\nabla p)^2$ profile for four different model sizes. For larger model, it takes a little bit longer to pressurize the formation at the bottomhole.

The numerical solution obtained by using described initial and boundary conditions yields the results shown in Figure 6.6, which describes the snapshots of porosity distribution at different time–steps. In this simulation, the initial injection rate is selected to be $q_0 = 0.1m/s$. That injection rate is applied at 12 nodes on the wellbore perimeter as described in the previous section. We assume fluid injection will not change fluid pressure in the far distances from the wellbore, therefore we can choose fixed pressure boundary condition at the exterior boundaries. In Figure 6.6 A-E, we see different flow pattern regimes: at time t = 0.1s, the waterfront is fairly uniform i.e. Darcy flow. Then branching in sand channels starts to initiate at the wellbore side at t = 0.5s. At t = 1s, sand channels start propagating. At this point injection pressure exceeds particles confining stresses so channel continue to grow. Reaching to the steady state can be easily verified by looking at channel maps at t = 3s and t = 6s, where there is no realizable difference in channels' geometry. This process demonstrates how flow divert into regions with low solid fraction (high hydraulic conductivity), while regions with higher solid fractions and lower hydraulic conductivity are avoided by the flow due to higher pressure gradient in these regions.

In particular, erosion threshold and pressure gradient level are determining particles mobilization. In the regions where $(\gamma^{-1}\nabla \mathrm{p})^2 > \sigma$, the grains are transformed from stationary to mobile due to reduction of local average porosity, which results in lower strength, σ. Similarly at the regions where$(\gamma^{-1}\nabla \mathrm{p})^2 < \sigma$, no erosion occurs, and probably at those regions the mobile grains come to rest, or in other words, deposit.

Figure 6.7 shows the nominal pressure gradient $(\gamma^{-1}\nabla \mathrm{p})^2$ around the wellbore at different time steps. The pressure gradient is initially high near the wellbore. As the system evolves with time, the pressure gradient which is a driving force in channel propagation is diminishing.

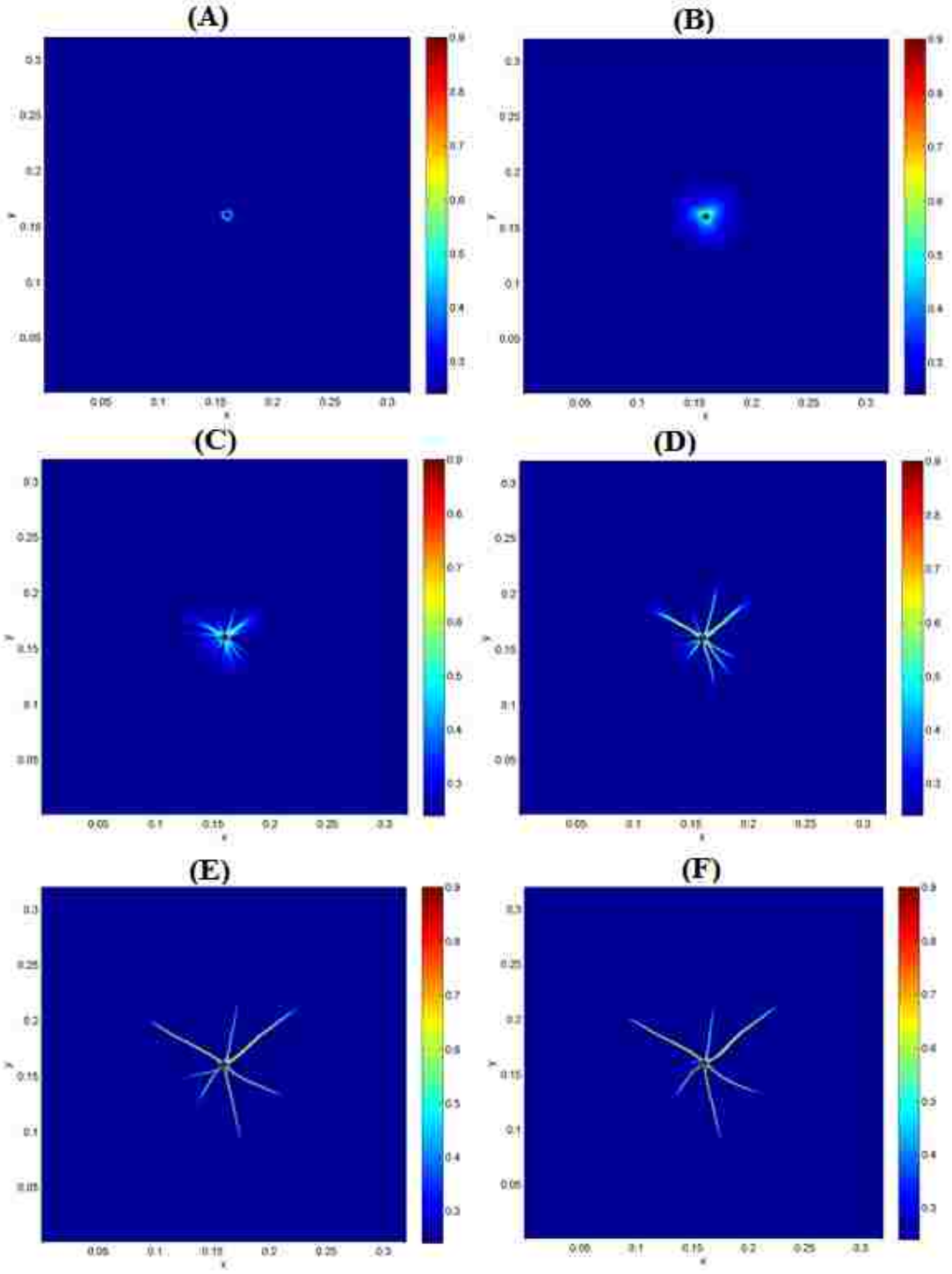

Figure 6.6. Evolution of porosity, φ is shown during injection, channel initiation and propagation of channels at (A) t = 0.01s (B) at t = 0.1s (C) at t = 0.5s (D) at t = 1s, (E) at t = 3s, and (F) at t =6s.

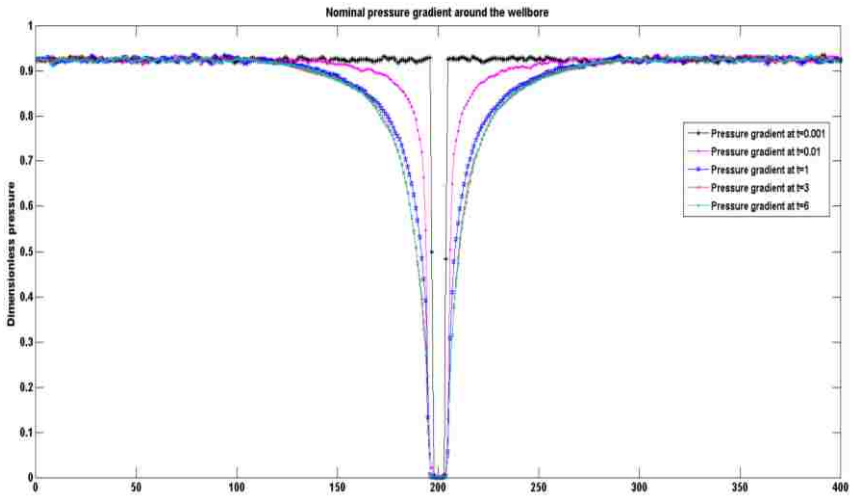

Figure 6.7.Pressure gradient around wellbore is shown to decrease with time.

In Figure 6.8, the stress distribution, σ, around the wellbore is shown, which decreases with time as injectivity increases. The initial confining stress is high since the grains are attached and sitting next to each other. The confinement provided by neighbor grains decreases due to the degradation of the rock matrix with the time. The bottom-hole pressure has been calculated in the model by averaging the pressure over all the nodes located inside the high permeable zone i.e. inner wellbore node. Figure 6.9 shows decrease in the bottom-hole flowing pressure on the center node with time.

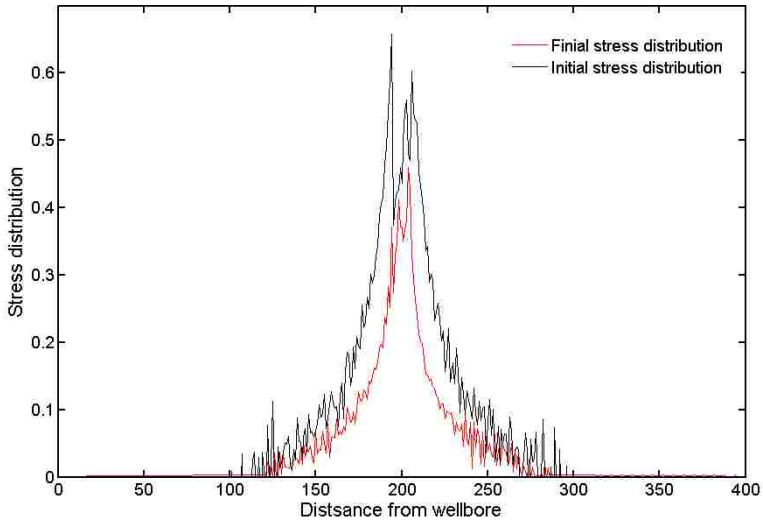

Figure 6.8. Grain resistance distribution around the wellbore is decreasing due to

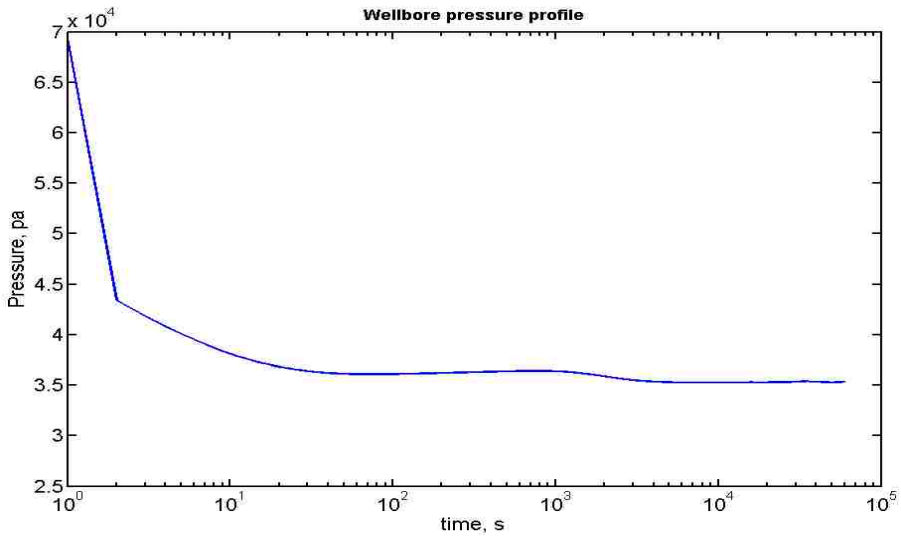

Figure 6.9. Decrease in bottom-hole pressure as a results of channelization for initial injection rate, $q = 0.1m/s$

In Figure 5.11., the porosity distribution in the channel at the end of injection, when the system reaches the steady state condition is shown. The initial porosity of the formation is 20% with 10% deviation. After injection the range of porosity in the created channels varies from 74% near the wellbore to the fracture tip with porosity almost equal to the initial formation porosity. During fluid injection and channelization, the porosity between the channel spacing decreases as the porosity in the channels increases. Meaning that channelization has led to enhanced or preferential flow paths though regions of higher conductivity at the expense of low reduced flow though other regions even as the total flow rate remains the same.

The change in porosity between the channels is shown in Figure 6.10. Figure 6.11. A, shows a side view of 3D plot of final porosity distribution and Figure 6.11. B shows the view of final porosity distribution from an angle between top and side view.

\

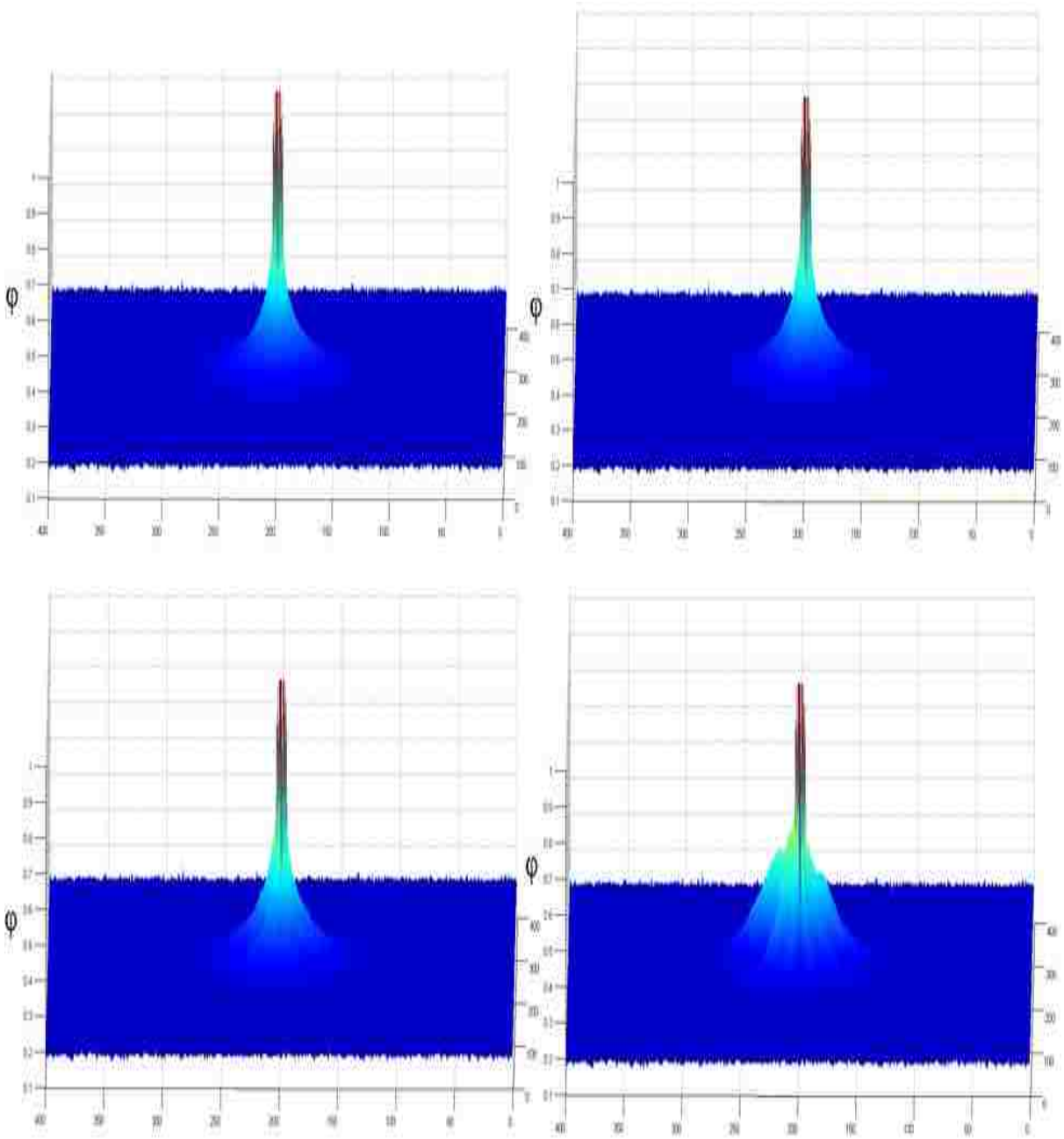

Figure 6.10. Change in porosity between channels during fluid injection. As shown in graph (A) the change in porosity around the wellbore initially is fairly uniform. With more fluid injection into the system, the uniformity in the porosity will change by increasing porosity at some regions at expense of other region. This is shown in graph (B) through (D).

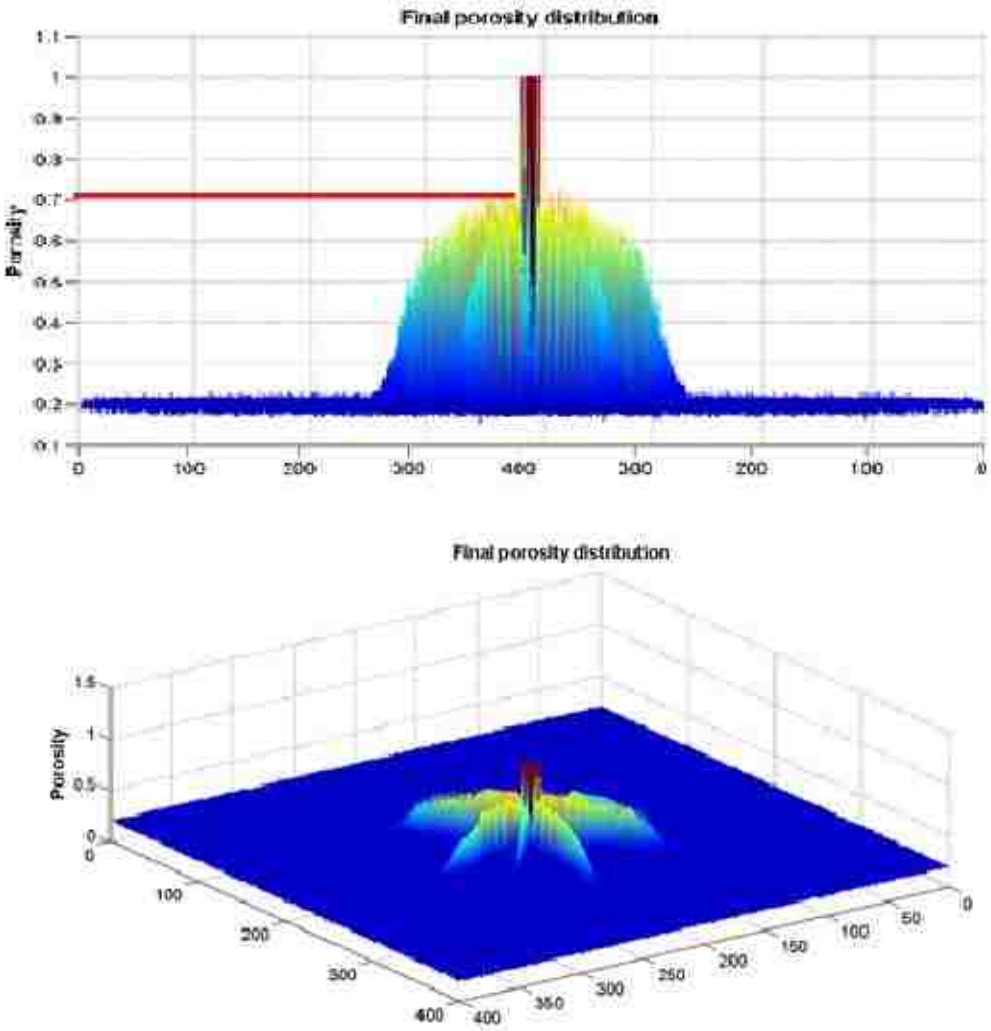

Figure 6.11. Finial porosity distribution from different angles for the base case with q = 0.1m/s.

6.2 Sensitivity Analysis for the Radial Model

To investigate the impact of various parameters on wellbore injectivity, bottom-hole pressure (BHP) and channeling, several sensitivity studies using different initial parameters such as flow rate, erosion threshold and noise distribution for initial porosity are conducted using the radial flow simulation.

6.2.1 Effect of Initial Flow Rate

A series of simulation were carried out by increasing the injection flow rate. To clearly understand how initial injection rate would affect the radial flow channelization. The injection parameters for this test

are summarized in Table 2. Different fracture patterns obtained using different injection rates are shown in Figure 6.12. Below the critical injection rate, which depends on the initial porosity distribution in the medium, fluid filtrate into the formation rock with limited damage only near the injector, but no further erosion or channeling occur. This is because the fracturing pressure has not reached with that injection rate, or to be more precise pressure gradient has not exceeded grain confining stresses and the pressure gradient everywhere is smaller than the erosion threshold. Final porosity distribution for initial injection rate of $q = 0.01\ \mathrm{m/s}$ is shown Figure 6.12. A. When the injection rate is equal to the threshold rate ($q = q_0$), the fluid induced pressure would be greater than the fracturing pressure; therefore, few channels are forming in different directions, but with short length as shown in Figure 6.12. B. for the initial injection rate of $q = 0.1\ \mathrm{m/s}$.

As q increases further, the number of channels as well as the length of channels increases. In all cases, porosity increases with time after initiation of the flow, linearly at first, and then slowly approaching a steady state condition that depends on the inlet injection rate.

Figure 6.13 shows the effects of different initial injection rates used in previous section on bottom-hole flowing pressure. The higher the initial flow rate causes the decline in BHP to occur faster and earlier during injection. After decrease in bottom-hole pressure, the trend of BHP would remain almost steady for long time small perturbations in BHP due to channels evolution and coalescence. For lower injection rate, we see that the decrease in injectivity pressure will take a longer time, however there is no further perturbation in the BHP, as slow injection rate pushes the system to the final configurations with smoother transition.

Histogram of the porosity for varying flow-rates is shown in Figure 6.14; High porosity mode is representing channels while the low porosity mode is representing part of the formation with fines deposition.

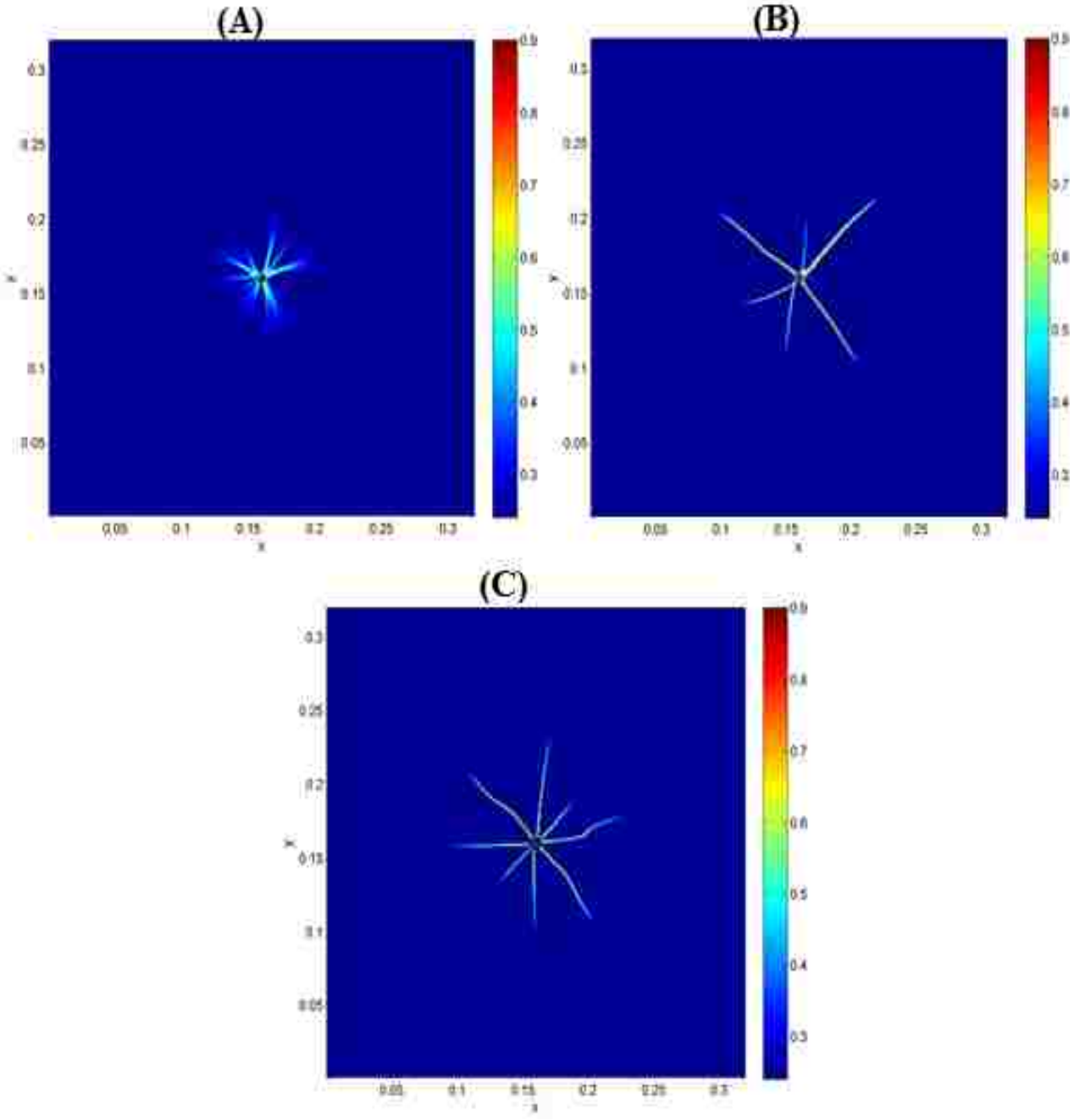

Figure 6.12. Final porosity snapshot for different injection rates at t = 6s. (A) for q = 0.01m/s channels initiated, (B) for q = 0.1m/s channels propagated, and (C) for q = 0.5m/s number of channels increased.

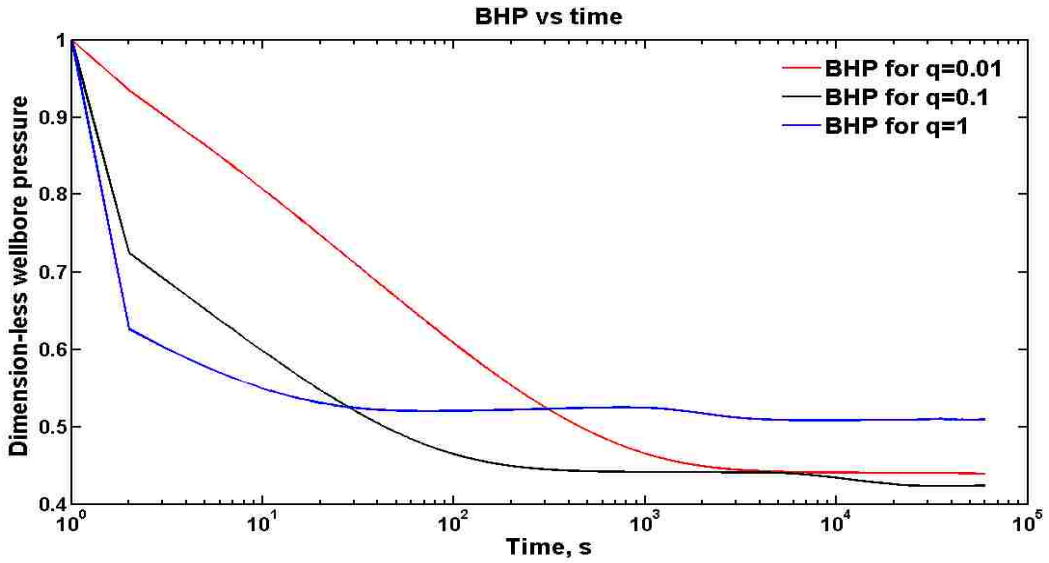

Figure 6.13. Change in BHP with time is shown for different injection rates. Higher injection rates leads immediate decline in BHP. It is notable that, after the system reaches steady-state condition, there is no change in BHP trend.

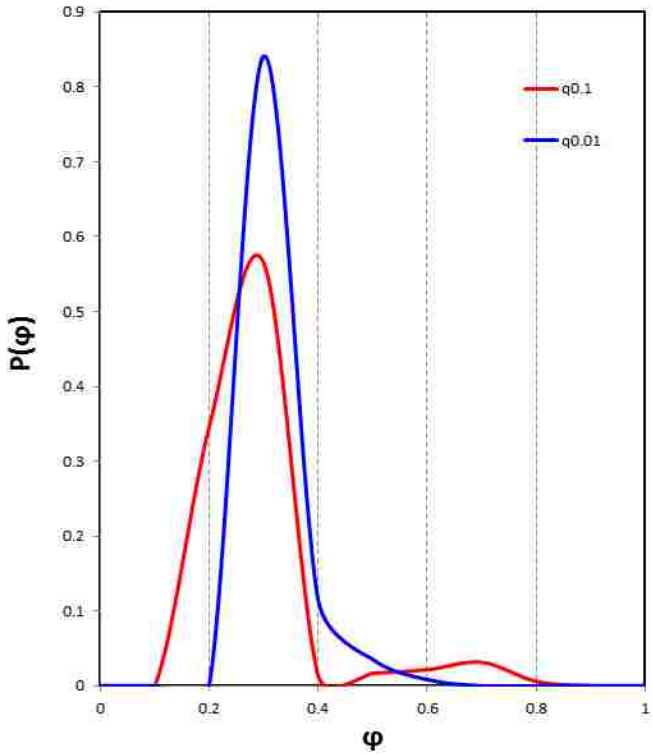

Figure 6.14. Porosity histogram for two different flow rates.

6.2.2 Sand Resistance against Erosion

As described in two-dimensional models, the effect of failure stress function on finial porosity distribution is essential in formation and growth of channels. The evolution of the porosity based on different form of erosion threshold is shown in Figure 6.15. In Figure 6.15. A, the final porosity distribution for local failure stress function $\sigma = 0.5 * (\tanh\big(2\pi(\overline{\varphi_s} - 0.6)\big) + 1$. In Figure 6.15. B, the porosity distribution for the function form $\sigma = 1 * (\tanh\big(2\pi(\overline{\varphi_s} - 0.6)\big) + 1)$ is shown. We can see that for the first form of failure stress, the number of channels is higher and less porous, but for the second form of failure model, the number of channels is less but the porosity is higher.

In Figure 6.16 we see the change in rate of bottom-hole pressure with time for the function of local failure stress $\sigma = 0.5 * (\tanh\big(2\pi(\overline{\varphi_s} - 0.6)\big) + 1$ and $\sigma = 1 * (\tanh\big(2\pi(\overline{\varphi_s} - 0.6)\big) + 1)$. We can see that the trend in BHP in both functional form of stress is close, however, for tortuosity of second form is more than the first form of stress function. In both case the system reached a steady state.

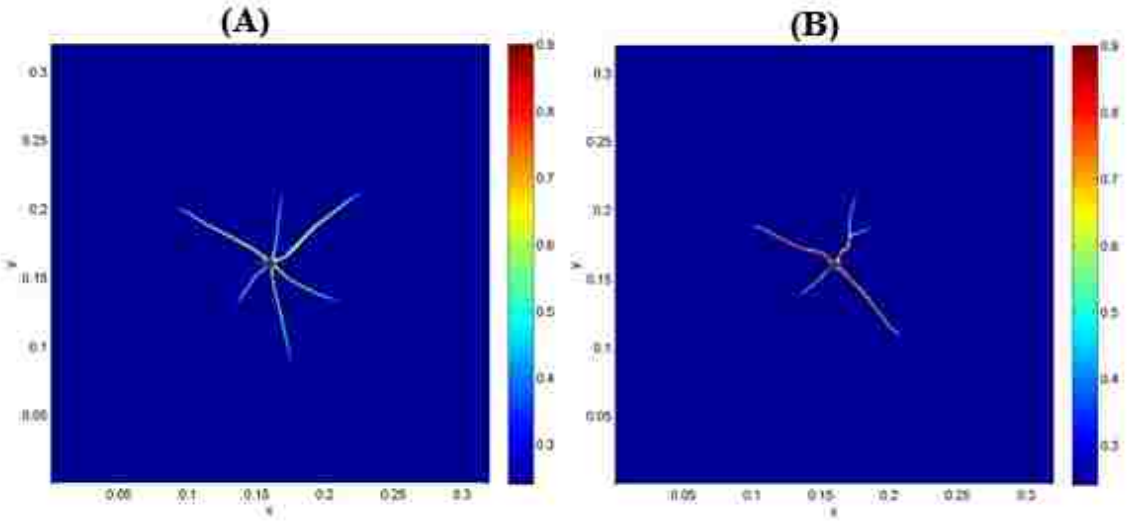

Figure 6.15. Final porosity distribution for failure stress function is shown to have impact on the growth of channels A) for less stress rock, 0.5 σ the number of channels are higher, B) for higher stress, 2 σ, the number of channel decreased.

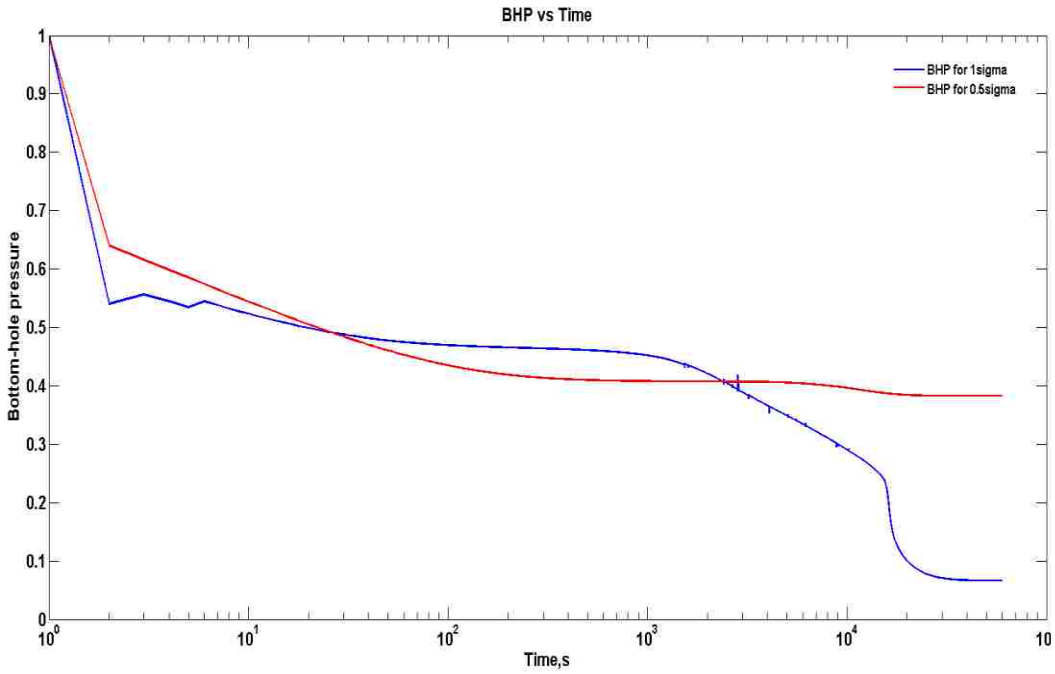

Figure 6.16. Effect of sigma on BHP. . The failure stress function, $\sigma = coeff * (\tanh(2\pi(\overline{\varphi_s} - 0.6)) + 1)$ is shown for the choices of (A) coeff = 0.5 (red), (B) coeff = 1 (blue)

6.2.3 Effect of Formation Heterogeneity

The other parameter that could change the behavior of the bottom-hole pressure is initial heterogeneity in strength, σ, which is a function of immobile solid porosity, φ_s. For used Gaussian method of disorder, if variance in the threshold for erosion (or the porosity fluctuations) is also changed, this leads to change in BHP trend and also channel patterns, which are shown in, Figure 6.17 and Figure 6.18, respectively. As shown in Figure 6.18. A, for a smaller standard distribution, $sd = 1\%$, the porosity distribution map is smoother and formed channels look fairly uniformly distributed. For higher standard deviation, $sd = 10\%$, we see more heterogeneity in the channels as shown in Figure 6.18. B. For even higher noise in the initial distribution of porosity, the induced channels will be more distinguishable as shown Figure 6.18. C.

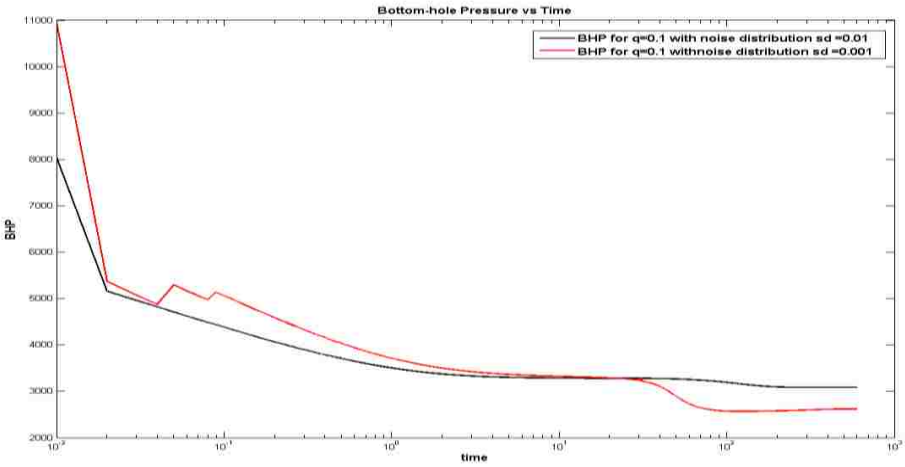

Figure 6.17. Effect of initial noise distribution on BHP. For lower sd, the tortuosity in change in BHP is higher than higher sd.

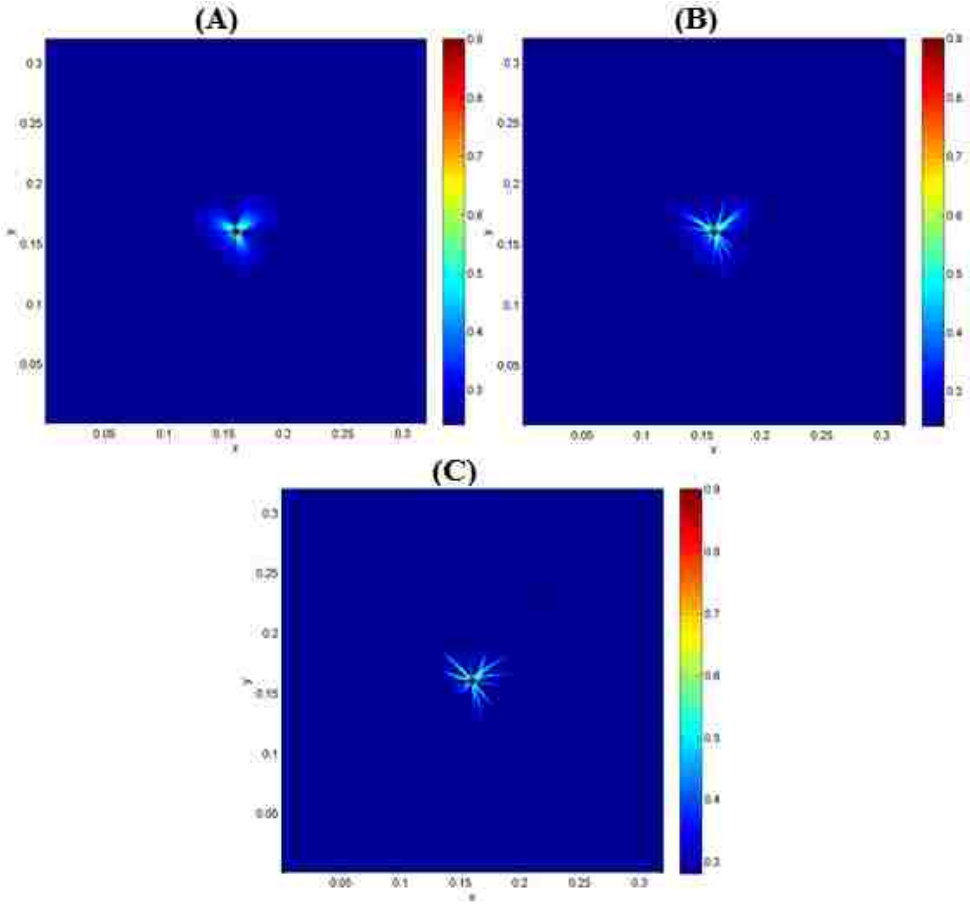

Figure 6.18. The distribution of porosity is shown to be sensitive to standard distribution for heterogeneity A) for $sd = 1\%$ the channel tip are smoother, B) for higher deviation, $sd = 10\%$ the tortuosity of channels increases, and C) for $sd = 30\%$ channels are even more disturbed

6.3 Water Flowback after Shut-in

Flowback is mainly the fluid injected into the formation that comes back toward the wellbore after immediate shut-down of the injectors. The instant shut-in of the injector will result in a pressure difference between channel tips and the wellbore. Therefore, particles might move back with the fluid from the channel tip toward the wellbore. The accumulation of particles in the wellbore may lead to injection loss. Fjaer et al., (2004) developed analytical model for continues sand production. This model is describing sand production from the rock around a cavity that has been brought beyond the onset of sand production. In this model a volume element of the rock in the vicinity of the cavity is considered. If sand is being produced from this element, the porosity increases. Mathematically, this relationship is described as

$$\frac{\partial m_{sand}}{\partial t} = \rho_s \frac{\partial \phi}{\partial t} \quad .$$

Here m_{sand} represents the (cumulative) mass of the sand being produced per unit volume of the rock, and ρ_s is the density of the sand grains.

In the radial flow model, the numerical solution for porosity evolution in the system is obtained by changing the boundary condition in the wellbore from an outflow to inflow. In Figure 6.19. A, a snapshot of final porosity distribution is show for injection at t = 6s. The decrease in porosity of channels after the injector is shut-in is shown in Figure 6.19. B, which is resulted from the movement of particles from formation toward the wellbore due to pressure imbalance. In this model, the injector is shut-in after t = 6s and well was shut-in for 2s. Figure 6.20 shows the instant decrease in bottomhole pressure after the injector is shut-in.

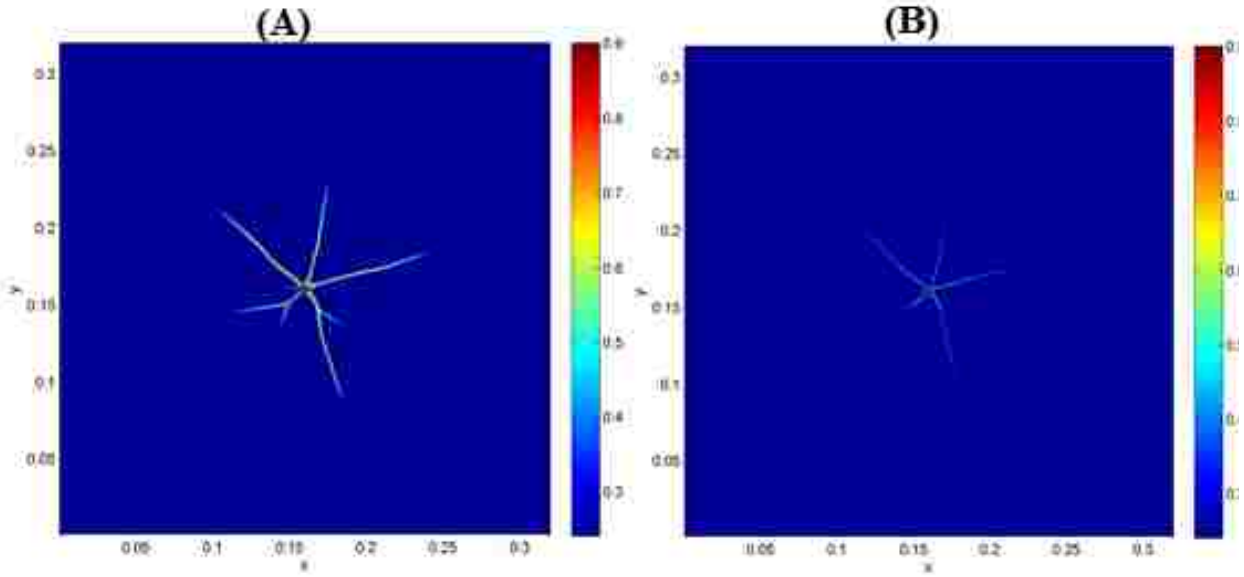

Figure 6.19. Spatial porosity distribution is shown for time before injection shut-down and after injection shut-down to see the effect of Flowback. Finial porosity distribution at A) t=6, B) after injector shut-down at t=6.2

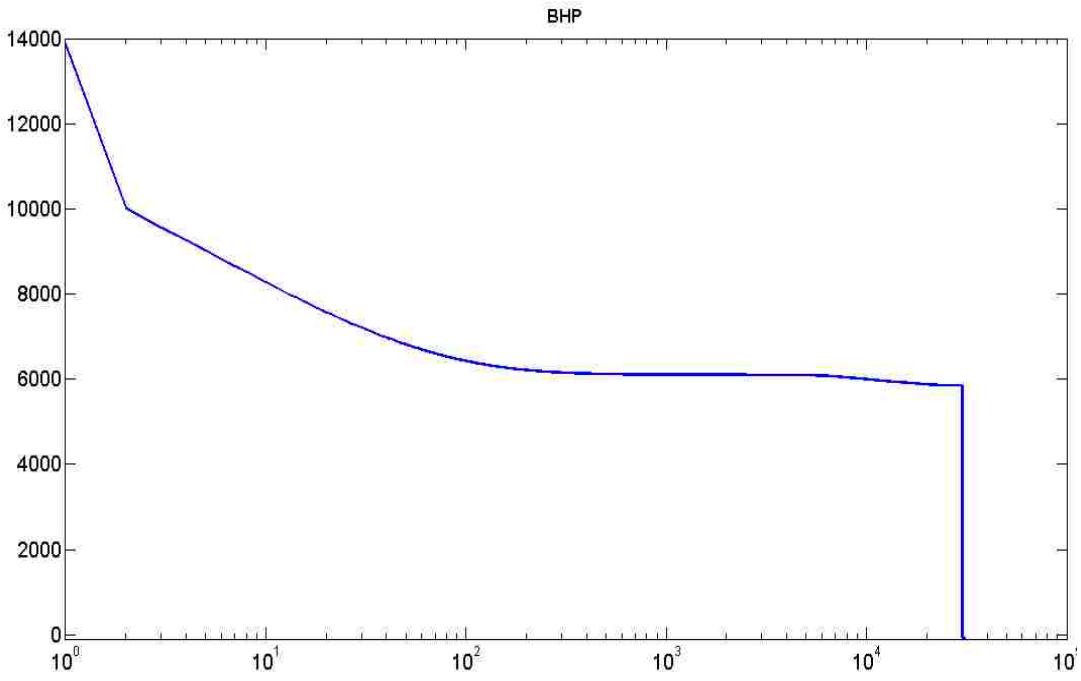

Figure 6.20. Immediate decrease in bottom-hole pressure after injector shut-down at t = 6s.

We examined the model to see the change in bottom-hole pressure with variable injection rates. In order to see the effect of injection pressure with variable rates, we ran the simulation for different flow-rates by cyclic increasing in flow-rates and cyclic shut-in of the injector for several cases.

The nine stage injection rate as flow rate and inflow parameters used for the first example are shown in Table 2. The injection starts at the initial time with the rate 0.001 m/s; the rate remains constant until time t_1, and then changes to q_2 instantaneously and remains constant until time t_2, and so on. The last injection rate is q_N until injection at time t_N, the end of injection cycle. At time t_{N+1}, the well is shut in and an influx rate of -0.0001m/s will replace the injection rate of q_N After the well remains shut-down for a short period of time, the injector resumed by an injection rate of 0.05m/s and for next time-step it will increase to 1m/s.

In Figure 6.21 different injection rates used for the simulation is shown. Figure 6.22 shows the corresponding bottom-hole pressure for different flow-rates.

Table 3. Injection rate and period of injection (case 1)

Flow-rate (m/s)	**Time (s)**
0	0
0.001	2
0.05	5
0.1	5
0.5	288
0.05	10
0.001	2
-0.0001	2
0.05	6
1	280

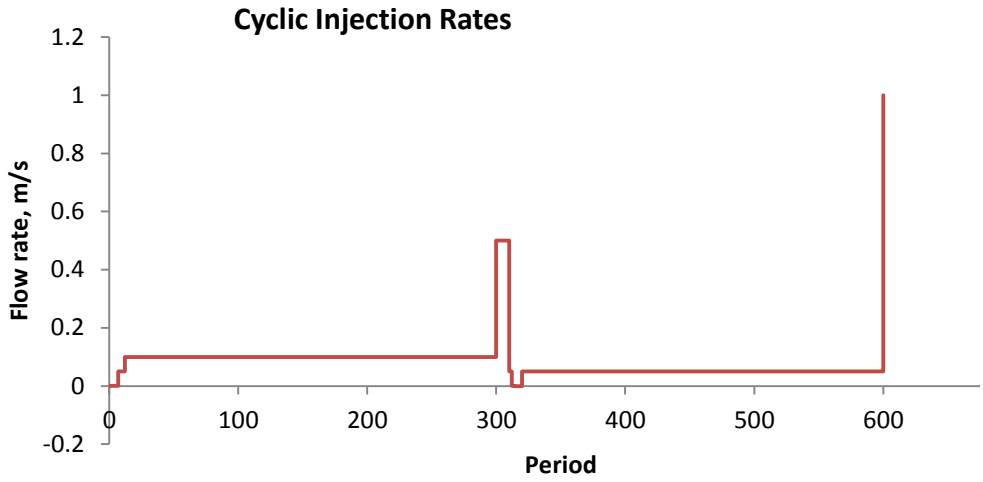

Figure 6.21. Diagram for rate of injection and period of injection (Example 1)

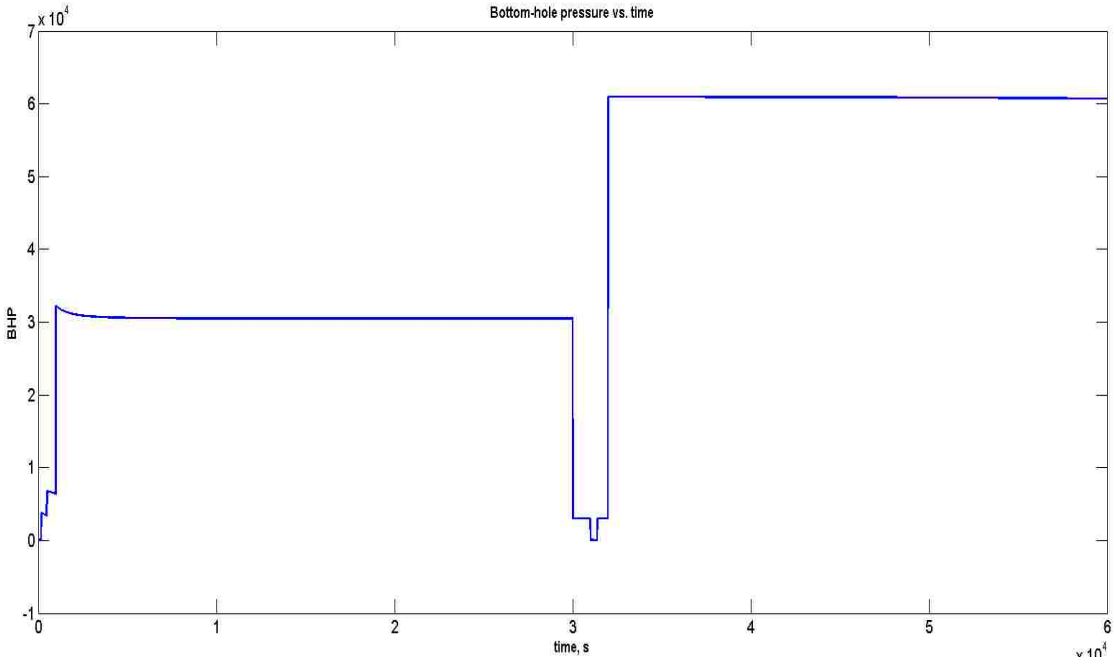

Figure 6.22. Multi-stage flow-rate increment during injection and shut-in.

In second example, we start injecting at higher rate in compare to case one. The parameters that used in this case are shown in Table 4. The injection starts at initial time with a rate 0.01 m/s; the rate remains constant until time t_1, and then changes to q_2 = 0.1m/s instantaneously and remains constant until

time t_2 = 3s and then the rate increase to q_3 = 1m/s and remains constant for t_2 = 94s. The last injection rate is q = 2m/s until injection at time t=420s, the end of injection cycle. After that, at time 420s, the injector will gradually shut down by decreasing the rate from 2m/s to 1, 0.1, and 0.00001 for total time of 5s. At this time, an influx rate of -0.0001m/s will replace the injection rate to simulate the condition which the system is shutdown. After the injector remain shut-down for a 25s, the injector will restart by an injection rate of 0.5m/s and remains constant for 2s and for next time-step it will increase to 2m/s for 48s. The injection rates that used for this case are shown in Figure 6.23 and the change in bottom-hole pressure for this test is shown in Figure 6.24.

In Figure 6.25, we observe that for even higher flow rates, there is increase in bottom-hole pressure at the beginning of injection because of higher fluid pressure than fracturing pressure; however, the BHP will decrease after breaking the fracturing pressure.

Table 4. Injection rate and period of injection (case 2)

Flow-rate (m/s)	**Time (s)**
0.01	3
0.1	3
1	94
2	420
1	2
0.1	2
0.00001	1
-0.1	25
0.5	2
2	48

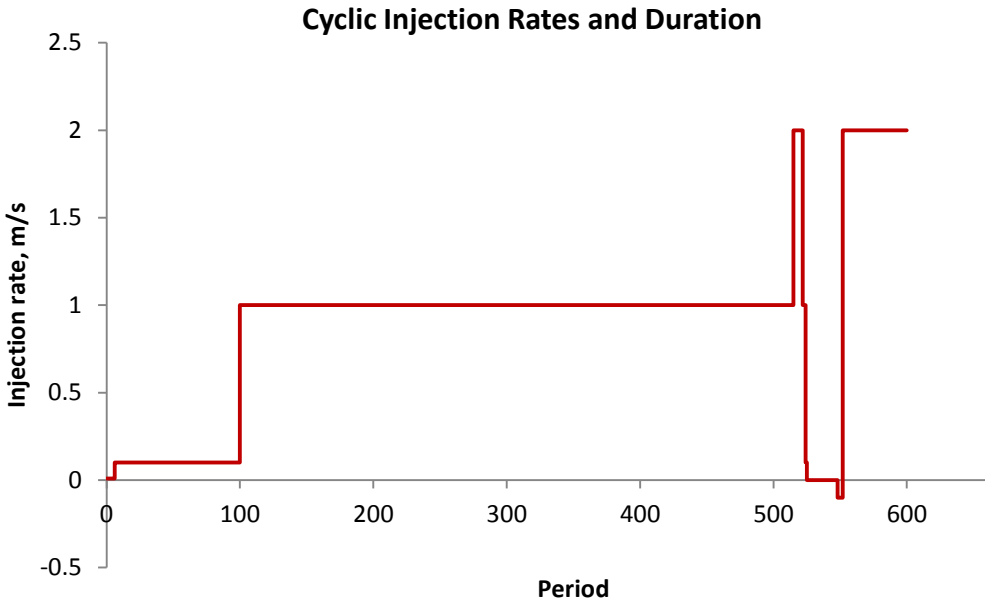

Figure 6.23. Diagram for rate of injection and period of injection (test2)

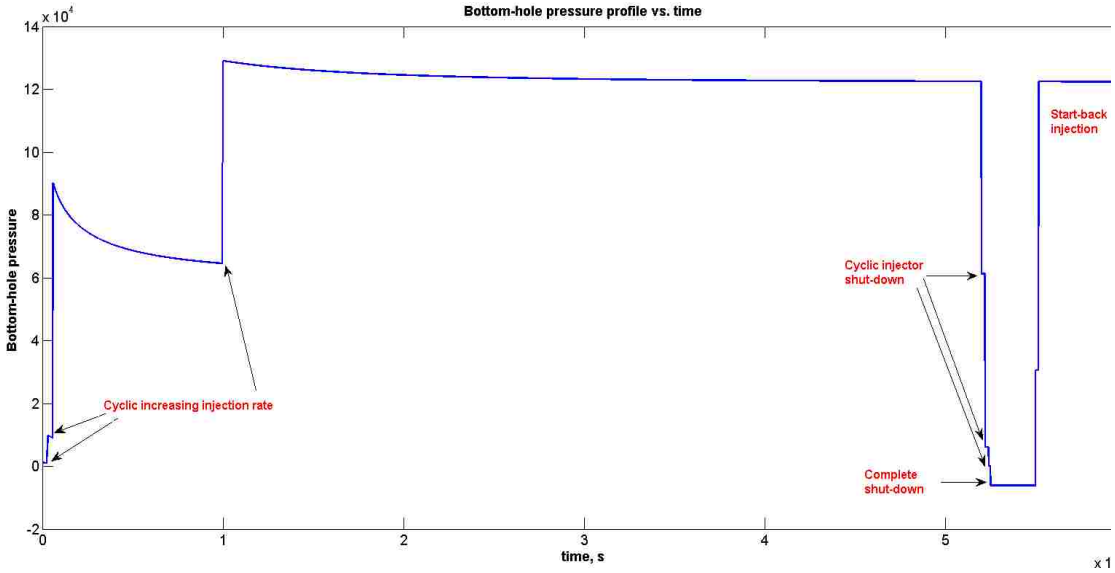

Figure 6.24. Cyclic injection and shut-down of injector

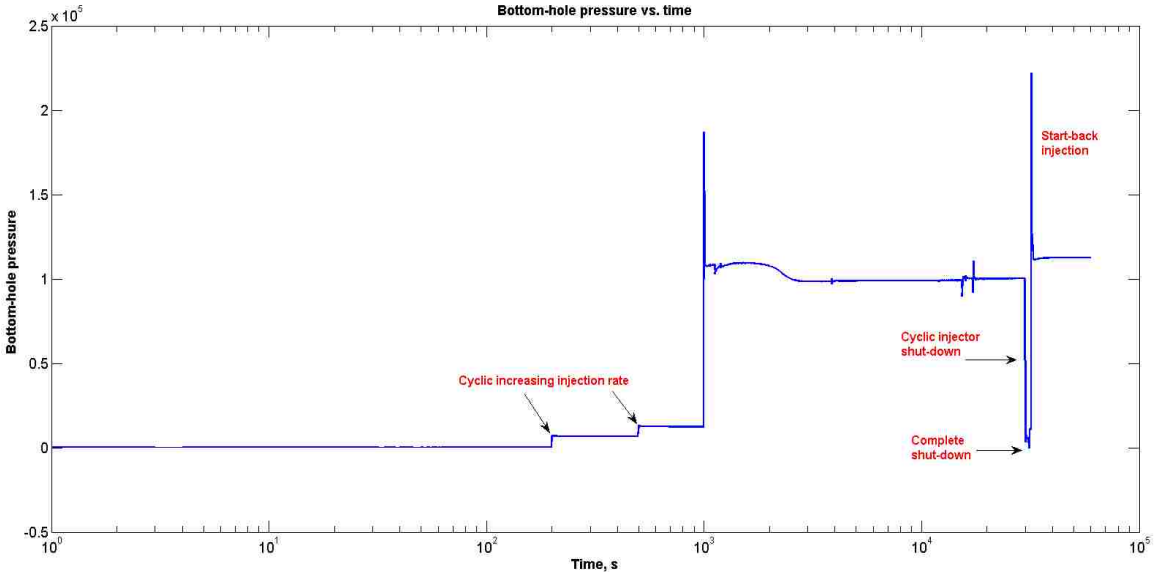

Figure 6.25. Cyclic injection and shut-down with high flow rate

6.4 Effect of Gravel Pack on Flowback Model

In this section, the effect of gravel packs on channel propagation and flow-back is examined. Gravel packs are used to create a downhole sand retention mechanism to keep the formation grains undistributed in their natural matrix. The gravel pack supports perforation tunnels or the openhole, keep formation grains in place, enables the channel of formation fines without plugging, and keep minimal pressure drop from the formation and into the injection and production stream(Chiong, 2013). The cased hole gravel pack system in this model is simulated by assuming high strength and higher porous regions around the wellbore. The parameters that are used for the gavel pack example are shown in Table 5 . In Figure 6.26, the injection nodes and gravel pack nodes are shown with red and green circles respectively.

In Figure 6.27, the effect of gravel pack on channelization is compared for a case when water is injected into openhole versus a case when gravel pack is in place. As shown in this figure, the number of channels is higher when the water injected into openhole and also a near wellbore damage is seen in the

case without gravel pack. In Figure 6.28, the effect of gravel pack on flowback after well shut-in is compared. As shown in this figure, for the case without gravel pack, we see more damage and sand accumulation near the wellbore than the case where gravel pack is used. The bottom hole pressure for both cases with and without gravel pack is compared in Figure 6.29, which as it shown, the effect of gravel pack on bottomhole pressure is not significant.

Table 5. Parameters used for Gravel Pack model.

Parameter	**Value**
Dimensions	$L_x = L_y = 50m$
Number of grids	400×400
Wellbore nodes	32
Injector nodes	12
Wellbore diameter	dx=0.125 m
Gravel pack thickness	$2 \times dx$ = 0.0357 m
Reservoir size	$400 \times dx$
Time-step	1e-2
Simulation time	6s
Initial porosity of the domain, φ_l	20%
Porosity of the gravel pack	30%
Mobile volume fraction, φ_g	0.0%
Strength of the gravel pack	3σ
Injection rate	0.01 - 2 m/s ($0.2 - 34\ bbl/min$)
Pore size	0.001m(1000μ)
Viscosity of fluid	$10^{-3}\ kg/m.s$
Characteristic hydraulic conductivity	$10^{-6}\ m^3.s/kg$
Porosity distribution noise	10%

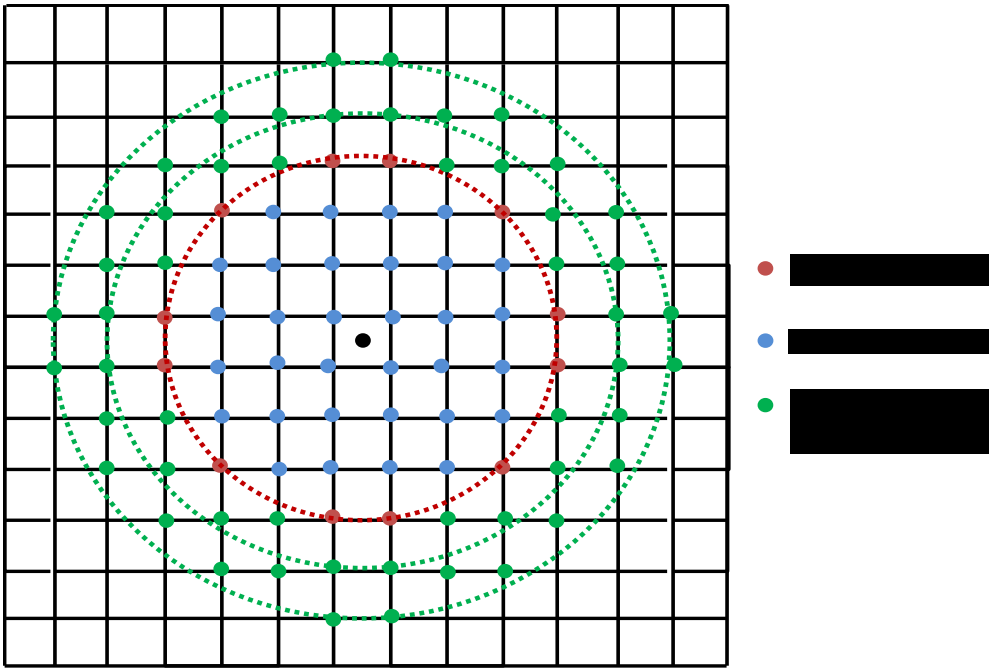

Figure 6.26. Cartesian grid for finite volume calculations. Injection well is located at the first inner red circle and gravel pack zone is shown with green circles and green nodes.

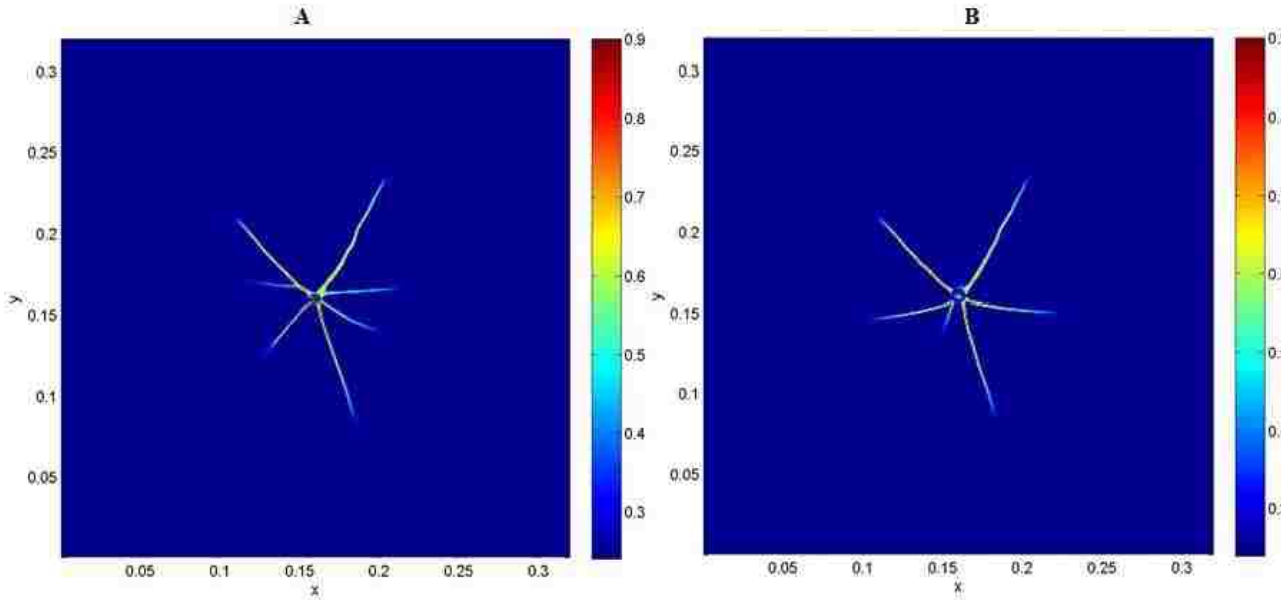

Figure 6.27. Comparison of injection into formation (A) without gravel pack shows more channels than the case (B) which with gravel used.

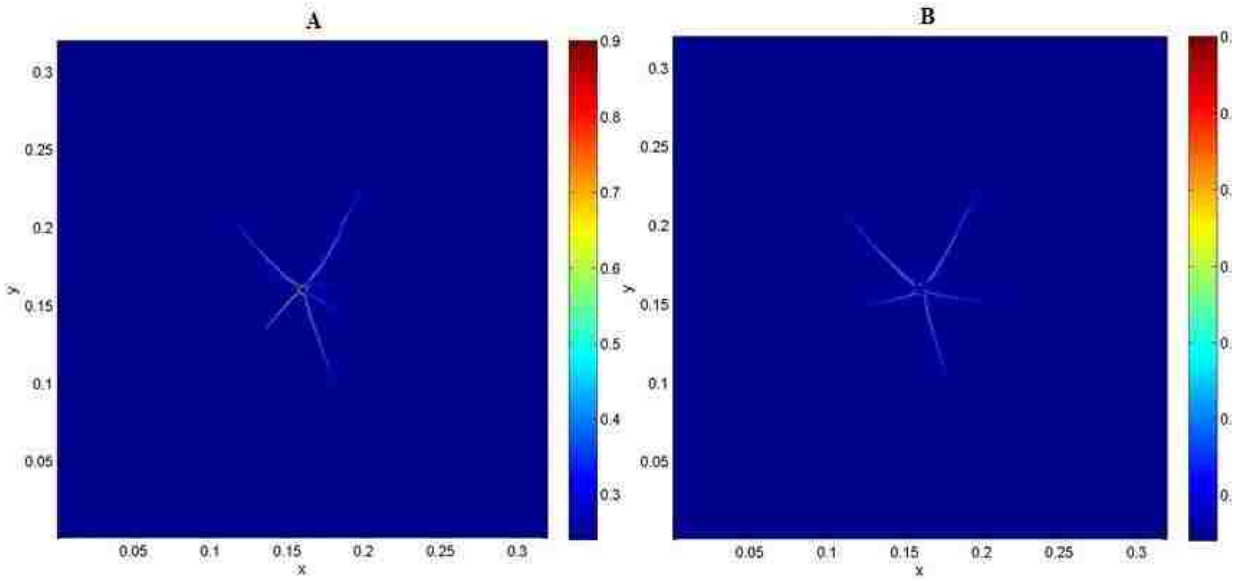

Figure 6.28. Comparison of Flowback into wellbore after well shut-in (A) without gravel pack shows more channels than the case (B) which with gravel used.

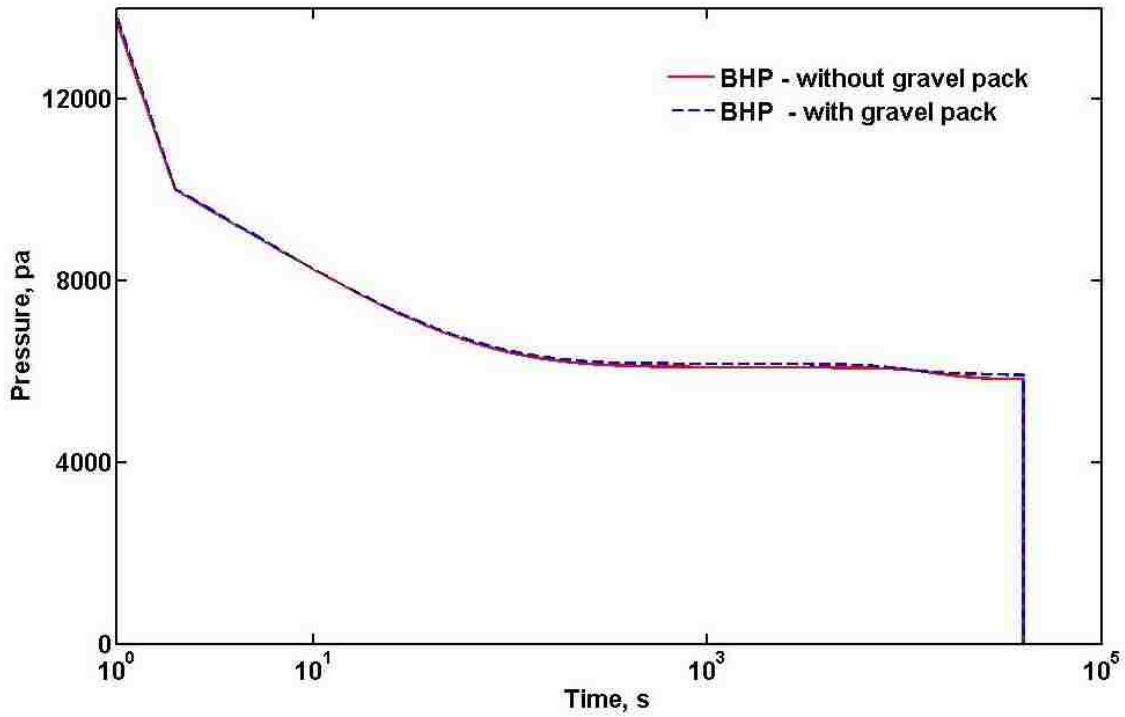

Figure 6.29. Bottom-hole pressure for injection into open hole and injection with gravel pack.

6.5 Chapter summary

In this chapter, linear flow simulation is developed for radial geometry to model channelization in injector wells. In the presented simulations a 2D Cartesian grid with finite volume method used to model radial flow channelization. The initiation and propagation of channels is described by interactions between pressure gradient of injection fluid and failure stress of the rock. Meaning that, where pressure gradient is greater than failure stress, the grains are dislodged and transformed from stationary to mobile because of reduction in immobile grains which result in lowering rock stress. In this model, change in bottomhole pressure during injection is estimated as a result of channelization. A sensitivity study is conducted to investigate the effect of different parameters on channelization patterns and bottomhole pressure. Finally a coupled model for channelization is developed to simulate fine migrations from formation toward the wellbore through the initiated channels during immediate injector shut-down (sand production).

Chapter 6: Conclusion and Future Work

The onset of erosional channelization that leads to injectivity decline and flow-back from formation due to particles in motion toward the wellbore during injectors shut-down are extremely important factors in waterflooding operations. Failure to prevent extreme flow-back, can results in safety risk, facilities challenges and a significant impairment to injection wells. A predictive model was developed to provide an assessment of the channel propagation and flow-back based on formation properties in unconsolidated formation.

This channelization model incorporates two sequential phenomena. The first one is the propagation of channels base on permeability evolution of the formation. This process is refers to as "erosion". In this step we showed that the porous medium, which is initially fairly uniform in porosity, becomes increasingly heterogeneous as the flow rate is increased, as erosion generates regions of enhanced porosity that connect to form channels with high conductivity. Eventually, the erosion patterns fuse together with time and just a few channels preferentially conduct most of the flow. The subsequent step for this model is flow-back. This instant shut-down of injector will result in pressure difference between channel tip and the wellbore, therefore particles that has been eroded along the channels, will move back with the fluid from the channel tip toward wellbore. The accumulation of particles in the wellbore may lead to injection loss.

According to different realizations generated for parameter sensitivity studies, I observe the following conclusions

- Flow rate has considerable effect on the creation of erosion or channels. That could be understood by the fact that, below critical flow rate, little or almost no erosion happens. Above this threshold, the porous medium starts to erode heterogeneously at regions where critical threshold is lowest.

- Erosion occurring at the regions with lower critical threshold has positive impact in enhancing erosion locally in other regions which leads these regions to become highly porous, meaning the channels can branch, start or stop in the medium.
- For a given flow rate, the pressure gradient and erosion rate decrease with time as channels form. Increase in average porosity of the region for higher flow rates is in consistent with channel forming.
- Also, a strong dependence between channelization patterns and heterogeneity of initial porosity distribution is seen in this model.
- Spatial porosity distribution and Bottom-hole pressure near wellbore is greatly affected by change in initial flow rate, the ratio of noise distribution for initial porosity and function form of erosion threshold σ.

To complete more realistic and generally applicable modeling of water injection in channel propagation in unconsolidated formation, the following are some recommendations for future work:

- Empirical fits to field data and experiment results can be obtained to have a better understating on how laboratory measurements of water injection into a cohesion-less formation is developed. This could lead to improving the onset of the model..

- In the provided model for flow-back, real field data could be used for duration of wellbore shut-down and restart the injection. Also, the amount of sand that flowed back could be estimated by providing analytical solution for the problem. The created model will be applied to apply on real field data to obtain model parameters for predicting near wellbore behavior.

- To achieve the defined goals of this project and validate the proposed models, it would be crucial to have access to field data such as rock properties and injection history. Rock properties include elastic and plastic properties, which can be extracted from the logs and core analysis. To access injection performance, normalize injectivity plots can be extracted

from the field data. Change in normalize injectivity slope is directly proportional to changes in injectivity and consequently frac-pack situation in downhole.

References

Abou-Sayed, A., Zaki, K., Wang, G., Meng, F., Sarfare, M. 2004. Fracture Propagation and Formation Disturbance during Injection and Frac-Pack Operations in Soft Compacting Rocks. SPE 90656-MS, SPE Annual Technical Conference and Exhibition, Houston, Texas.

A-Kindi, A., Prince-Wright, R., Walsh, J., Kuijvenhoven, C., Mergenthaler, L., Moore, W. 2008. Challenges for Waterflooding in a Deepwater Environment. SPE 118735-PA, Volume 23, Number, 3.

Barry Truax, ed. 1999. "Handbook for Acoustic Ecology" (Second ed.). Cambridge Street Publishing. Retrieved 2012-08-05.

Charlez, P., Lemonnier, P., Ruffet, C., Stilog, Bouteca, M.J., Tan, C., Altran. 1996. Thermally Induced Fracturing: Analysis of a Field Case in North Sea. SPE 36916-MS, presented at European Petroleum Conference, Milan, Italy.

Chiong, A. 2013. Solving your Sand Control Challenges. Weatherford, Science & Technology, 14.

Dusseault, M. B., Bruno, M. S., Barrera, J. 2001. Casing Shear: Causes, Cases, and Cures. SPE-72060 Drilling & Completion 16(2): 98-107

Furtado, C. J. A., Siqueira, A.G., Souza, A.L.S., Correa, A.C.F. 2005. Produced Water Reinjection in Petrobras Fields: Challenges and Perspectives. SPE - 94705-MS-P.

Gadde, P. B., Sharma, M. M. 2001. Growing Injection Well Fractures and Their Impact on Waterflood Performance. SPE 71614-MS, presented at SPE Hydraulic Fracturing Technology Conference and Exhibition, New Orleans, Louisiana.

Gang, H., Revay, J., Kalfayan, L., Perez, J., Walters, D., Bachman, R. 2011. Production and Rock Stability around a Frac-Packed Gulf of Mexico Well.

Garland, E. 2003. Discharge of Produced Water New Challenges for an Old Issue. Total Final Exploration-Production. OMC.

Guan L., Y. D., Wang, Z. 2005. Water Injectivity-What we have learned in the past 30 years. Canadian International Petroleum Conference, Calgary, Alberta

Huang, H., Zhang, F., Callahan, P., Ayoub, J. 2011. Fluid Injection Experiments in Two-dimensional Porous Media. SPE-140502-MS. SPE Hydraulic Fracturing Technology Conference, the Woodlands, Texas, USA.

Kuo, M. C. T., Hanson, H.G., DesBrisay, C.L. 1984. Prediction of Fracture Extension during Waterflood Operations. SPE-12769-MS California Regional Meeting, Long Beach, California. ISBN 978-1-55563-644-9

Leveque, R. J. 2004. Finite Volume Methods for Hyperbolic Problems. 129-130.

Mahadevan, A., Orpe, A. V., Kudolli, A., Mahadevan, L. 2012. Flow-induced channelization in a porous medium. EPL 98 (5).

Mills, P., Cerasi P., Fautrat, S. 1995. Erosion Instability in a Non-Consolidated Porous-Medium. Europhys. Lett. 29 215.

Morita, N., Davis, E., Whitebay, Lee. 1998. Guidelines for Solving Sand Problems in Water Injection Wells. SPE 39436

Muecke, T. W. 1978. Formation Fines and Factors Controlling Their Movement in Porous Media SPE-AIME, Exxon Production Research Co. 149-2136/79/0002-7007

Muñoz Mazo, E. O., Moreno, J.M.M., Schiozer, D.J. 2007. Study of Sweep Efficiency of Water Injection under Fracturing-Conditions Process. SPE 107846-MS, Latin American & Caribbean Petroleum Engineering Conference, Buenos Aires, Argentina

Pedroso, C. A., Carlos, L., Alves da Paixao, L.C., da Motta Pires, P. R., Petrobras 2009. Analysis of Fracture Growth Induced by the Injection of Water Above the Fracture Pressure in Nonconsolidated Sandstones and Soft Carbonates-Deviations from the Linear Elastic Model or Why Can't I Inject Even Above the Fracture Pressure? SPE 122180-MS, presented at 8th European Formation Damage Conference, Scheveningen, The Netherlands.

Perkins, T. K., Gonzalez, J. A. 1985. The Effect of thermoelastic stress on injection well fracturing. SPE 11332-PA, v. 25(1), pp. 78-88.

Plasson, B., Davies, D.R., Todd, A.C., Somerville, J.M. 2003. A Holistic Review of the Water Injection Process. SPE 82224-MS. ISBN 978-1-55563-963-1.

Robertson, E. 2007. Low-Salinity Waterflooding to Improve Oil Recovery – Historical Field Evidence SPE 109965 INL/CON-07-12934.

Santarelli, F. J., F. S., Embry J.M. 2011. The Sanding Mechanisms of Water Injector and their Quantification in Terms of Sand Production. SPE 146551-MS, SPE Annual Technical Conference and Exhibition, Denver, Colorado, USA.

Scheidegger, A. E. 1960. The physics of flow through porous media. Macmillan Company, New York.

Sharma M.M., S., Pang S., Wennberg, K.E., Morgenthaler, L. 1997. Injectivity decline in water injection wells, an offshore Gulf of Mexico case study. SPE 38180-MS, SPE European Formation Damage Conference, The Hague, Netherlands

Sharma, M.M. 2003. Injection Water Management Opportunities and Challenges. Presentation, University of Texas at Austin.

Silin, D. B., Patzek, T. W. 2001. Control Model of Water injection into a Layered Formations SPE 71751, SPE Journal, Volume 6, number 3, pp.253-261

Slevinsky, B. A. 2002. A Model for Analysis of Injection-Well Thermal Fractures. SPE 77568-MS, SPE Annual Technical Conference and Exhibition, San Antonio, Texas.

Suri, A., Sharma, M. 2007. A Model for Water Injection into Frac-Packed Wells. SPE 110084-MS, SPE Annual Technical Conference and Exhibition, Anaheim, California, U.S.A.

Suri, A., Sharma, M. 2010. A Model for Water Injection into Frac-Packed Wells. SPE 110084-PA, SPE Reservoir Evaluation & Engineering, Volume 13, Number 3, pp. 449-464.

Svendsen, A.P., Wright, M.S., Clifford, P., Berry, P. 1991. Thermally Induced Fracturing of Ula Water Injectors SPE, and SPE, BP Norway Ltd., and... SPE and BP Research Centre.

Tran, M. H., Abousleiman, Y.N. 2010. The Impacts of Failure Criteria and Geological Stress States on the Sensitivity of Parameters in Wellbore Stability Analysis. ARMA 10-328. 44th U.S. Rock Mechanics Symposium and 5th U.S.-Canada Rock Mechanics Symposium, Salt Lake City, Utah

Van den Hoek, P. J., Hustedt, B., Sobera, M., Mahani, H., Masfry, R.A., Snippe, J., and Zwarts, D. 2008. Dynamic Induced Fractures in Waterflooding and EOR. SPE 115204-MS. SPE Russian Oil and Gas Technical Conference and Exhibition, Moscow, Russia.

Vaziri, H., Nouri, A., Hovem, K., and Wang, X. 2008. Computation of sand production in water injectors. SPE 107695-PA. SPE Production & Operations, Volume 23, Number 4, pp. 518-524.

Wang, X., Hovem, K., Moos, D,. Quan, Y. 2008. Water Hammer Effect on Water Injection Well Performance and Longevity. SPE 112282-MS presented at SPE International Symposium and Exhibition on Formation Damage Control, Lafayette, Louisiana, USA.

Appendix

NOMENCLATURE

L_x, L_y	Dimensions
N_x, N_y	Number of grids
r_w	Wellbore radius
r_e	Reservoir radius
Δt	Time-step
t	Simulation time
L	Domain size
φ_l	Liquid porosity
φ_s	Immobile volume fraction
φ_g	Mobile volume fraction
D	Hydraulic conductivity
k	Permeability
σ	Rock strength
l_g	Pore size
μ	Viscosity of fluid
A	Dimensionless constant
γ	Characteristic hydraulic conductivity
sd	Distribution noise

Vita

Siyamak Ameen was born in 1986 in Miyandoab, Iran. He earned his high school diploma in Andishe-Sazan, Tehran, Iran on 2003. He then obtained a Bachelor of Science in Petroleum Engineering, University of Koya, Kurdistan Regional Government, on 2008. He worked in Romfor International Drilling, Kurdistan Regional Government, from May 2008 to December 2010. Thereafter, he enrolled in the Craft & Hawkins Department of Petroleum Engineering at Louisiana State University in the January 2011 to work towards a master degree in Petroleum Engineering to be awarded in December 2013.